

A Thermochronological Investigation of Orogenic Architecture, Kinematics, and Tectonic-Climatic Interactions within the St. Elias Orogen, Alaska

Aaron Louis Berger

Dissertation submitted to the faculty of the Virginia Polytechnic Institute and State University in partial fulfillment of the requirements for the degree of

**Doctor of Philosophy
in
Geosciences**

Committee

James A. Spotila, Chair
Richard D. Law
John A. Hole
Kenneth A. Eriksson
Robert J. Bodnar

March, 24th, 2008
Blacksburg, Virginia

Keywords: orogenesis, critical Coulomb wedge, glacial erosion, St. Elias orogen, thermochronometry, (U-Th)/He dating, exhumation, climate-tectonic coupling, terrane accretion, Alaska tectonics.

Copyright © 2008, Aaron Louis Berger

A Thermochronological Investigation of Orogenic Architecture, Kinematics, and Tectonic-Climatic Interactions within the St. Elias Orogen, Alaska

Aaron Louis Berger

ABSTRACT

The kinematics and architecture of orogenic systems may be heavily influenced by climate, but little research has focused on the long-term effects of glacial erosion on orogenesis. Low-temperature thermochronometry and subsidiary structural, earthquake relocation, and offshore seismic reflection data from the St. Elias orogen are the basis for a new architectural model and demonstrate an association between glacial denudation and orogenic evolution. These data show that exhumation and deformation within the St. Elias orogen are focused across a thin-skinned fold and thrust belt on the windward flank, whereas the leeward flank functions as a deformational backstop. A previously unrecognized structure beneath the Bagley ice field separates these domains with south-side-up motion. This structure is interpreted to be a backthrust, making the orogen doubly-vergent. Suggestive of accelerated fault motion in response to climate change, bedrock cooling rates within the hanging wall of the backthrust and across the entire subaerial wedge accelerated ~ten-fold coeval with the onset of intense glacial conditions. Within the orogenic wedge, the zone of highest Quaternary exhumation (5 km/myr ($\pm 25\%$)) is focused around a narrow zone where the glacial equilibrium line altitude (ELA) intersects mean topography. This zone of rapid exhumation, not present prior to the onset of intense glacial conditions, cuts across the structural trend of the orogen and is more narrowly focused than the zone of orographic precipitation. Augmented glacial

erosion around glacial ELA also coincided with a regional shift in deformation away from prominent forethrusts including the North American-Yakutat terrane suture (Chugach St. Elias fault) and the seaward deformation front (Pamplona zone). Accelerated denudation across the subaerial wedge thus appears to have forced the redistribution of strain along the backthrust and a series of forethrusts that lie beneath the zone of highest glacial flux, which in turn are systematically truncated by the backthrust. In a cause and effect response, the expansion of glaciers therefore appears to have resulted in an orogen scale structural reorganization and a narrowing of the orogenic wedge to preserve topographic slope. The focusing of long-term erosion around glacial ELA and the structural response of the orogenic wedge to Cenozoic climate change have not previously been observed in a real-world orogenic system and imply a high degree of coupling between climate and tectonics in this glacially-dominated orogen.

ACKNOWLEDGEMENTS

The culmination of my academic career would not have been possible without the support and encouragement of many people throughout my life. Of utmost importance, I would like to draw attention to my wife (Elizabeth Berger), who is the person who would be the last to ask or expect acknowledgment. Without her continuous and unwavering love and support this dissertation would not have been possible. I am unsure what I did to deserve such a wonderful friend and partner. I would also like to thank my entire family who engrained in me the value of hard work, integrity, and an education, without which my achievements in life would not have been possible. To this end, I would especially like to recognize my mother and father (Sheila and Edwin Berger), who taught me to never fail or lose sight of my goals, and also my grandfather and grandmother (Harold and Lillian Dotson), who were like second parents to me.

My passion for geology and ultimately the path to my Ph.D. can be traced back to my earliest memories with my father who always found time to take me into the hills and go on adventures in search of beautiful minerals and natural wonders. As a self-taught geologist, his questions and observations continue to amaze me. I began my academic career in geosciences at New Mexico Tech where Dr. William Chavez, Dr. Peter Mozley, and Dr. Bruce Harrison were instrumental in my decision to pursue a career in geosciences and to attend graduate school. After receiving my B.S. in geology, I subsequently started work on my masters at Montana Tech where Dr. Christopher Gammons and Dr. Richard Berg taught me the basics of independent research and scientific writing and helped me get accepted into the Virginia Tech Ph.D. program

where my most significant personal achievements as a scientist and professional took place.

Dr. James Spotila was my Ph.D. advisor and was responsible for my continued development as a scientist. His high standards and relentless scientific critique pushed me to achieve ever greater skills as a scientist and a writer and were instrumental in all that I have accomplished. Dr. Spotila is an exceptional scientist as well as a friend. My committee members, Dr. Richard Law, Dr. Kenneth Eriksson, Dr. John Hole, and Dr. Robert Bodnar provided additional guidance and taught me a great deal about their respective fields. My research group was also a key component of my success at Virginia Tech. Ryan McAleer and Jamie Buscher helped me learn the basics of thermochronometry and served a continuous source of scientific discussion. They, along with Lisa Tranel, were also helpful during my many frustrating problems with ArcGIS. I would also like to thank Connie Lowe, who is always on the side of the students, as well as the rest of the administrative and technical staff at Virginia Tech.

ATTRIBUTIONS

Several colleagues aided in the writing and research presented within this dissertation. A brief description of their contributions is included here. The content and scope of this dissertation was edited, critiqued, and shaped by my doctoral committee, which is made up of Dr. James A. Spotila (chair), Dr. Richard D. Law, Dr. Kenneth A. Eriksson, Dr. John A. Hole, and Dr. Robert J. Bodnar. Each of my committee members is a faculty member within Virginia Tech's Department of Geosciences. Dr. James A. Spotila is an Associate Professor of Geology and specializes in low-temperature thermochronometry and neotectonics; Dr. Richard D. Law is a Professor of Geology and specializes in structural geology and crustal deformation; Dr. Kenneth A. Eriksson is a Professor of Geology and specializes in siliciclastic sedimentology and Precambrian crustal evolution; Dr. John A. Hole is an Associate Professor of Geophysics and specializes in exploration seismology and the development of continental crust; and Dr. Robert J. Bodnar is a University Distinguished Professor of Geochemistry and specializes in fluid inclusions and fluids in low-to-high-temperature geologic environments.

Chapter three was submitted to *Earth and Planetary Science Letters* "Aaron L. Berger, James A. Spotila, James B. Chapman, Terry L. Pavlis, Eva Enkelmann, Natalia A. Ruppert, and Jamie T. Buscher; Architecture, Kinematics, and Exhumation of a Convergent Orogenic Wedge: A Thermochronological Investigation of Tectonic-Climatic Interactions within the Central St. Elias Orogen, Alaska." All authors contributed to the interpretations and to the editing process. A.L. Berger collected and prepared samples to be dated by the (U-Th)/He technique, developed the hypotheses presented, proposed the

existence of a backthrust beneath the Bagley ice field, conducted ArcGIS analyses, created figures and tables, interpreted data, and wrote the manuscript. J.A. Spotila analyzed samples on the (U-Th)/He line, provided scientific support and critique, and secured funding. A.L. Berger, J.B. Chapman, and T.L. Pavlis developed the architectural model of the orogen. N.A. Ruppert obtained and analyzed the earthquake data. E. Enkelmann dated samples using the ZHe and ZFT technique.

Chapter four was submitted to *Geology* “Aaron L. Berger and James A. Spotila; Denudation and Deformation in a Glaciated Orogenic Wedge: The St. Elias Orogen, Alaska.” A.L. Berger and J.A. Spotila developed hypotheses to be tested, created figures and tables, and co-wrote the manuscript. A.L. Berger collected and prepared samples to be dated by the (U-Th)/He technique and conducted ArcGIS analyses. J.A. Spotila secured funding for the project and analyzed samples on the (U-Th)/He line.

Chapter five was submitted to *Nature Geoscience* “Aaron L. Berger, Sean P. S. Gulick, James A. Spotila, John M. Jaeger, James B. Chapman, Lindsay A. Lowe, Terry L. Pavlis, Kenneth D. Ridgway, Bryce Willems, Ryan J. McAleer; Quaternary Tectonic Response to Intensified Glacial Erosion in an Orogenic Wedge.” All authors contributed to the interpretations, hypotheses presented, and to the editing process. Writing was done by A.L. Berger, with subsidiary contributions by J.A. Spotila and S.P.S. Gulick. A.L. Berger collected and prepared samples to be dated by the (U-Th)/He technique, conducted ArcGIS analyses, created figures, and interpreted the low-temperature thermochronometry data. A.L. Berger, J.B. Chapman, and T.L. Pavlis developed structural models. S.P.S. Gulick, L.A. Lowe, and J.M. Jaeger collected and processed

seismic reflection data and integrated the well data (biostratigraphy) into the manuscript.

Research funding was provided by J.A Spotila and S.P.S. Gulick.

TABLE OF CONTENTS

Abstract.....	ii
Acknowledgements.....	iv
Attributions.....	vi
Table of Contents.....	ix
List of Multimedia Objects.....	xii
Grant and Funding Information.....	xv
Chapter 1	
Introduction.....	1
References.....	5
Chapter 2	
Tectonic History of Southwest Alaska Prior to the onset of Yakutat Driven Orogenesis.....	15
Accretion of the Chugach Terrane.....	16
Accretion of the Prince William Terrane.....	18
High-Temperature / Low-Pressure Metamorphism.....	19
References.....	20
Chapter 3	
Architecture, Kinematics, and Exhumation of a Convergent Orogenic Wedge: A Thermochronological Investigation of Tectonic-Climatic Interactions within the Central St. Elias Orogen, Alaska.....	29
Abstract.....	30
Introduction.....	31
Background: The St. Elias Orogen.....	33
Methods.....	36
Results and Interpretations.....	38
New data.....	38
General pattern of cooling ages.....	39

Constraints on cooling history and maximum burial temperatures.....	42
Differences in low-temperature cooling across major faults.....	43
Discussions.....	45
Constraints on active deformation.....	45
Architecture of the St. Elias orogen.....	49
Role of glacial climate in orogenic wedge deformation.....	50
Conclusions.....	53
Acknowledgements.....	55
References.....	56
Appendix A.....	82
Analytical methods.....	82
Acceleration in bedrock cooling rates.....	85
Particle trajectories the St. Elias orogen.....	86
Additional references.....	88

Chapter 4

Denudation and Deformation in a Glaciated Orogenic Wedge: The St. Elias Orogen, Alaska.....	93
Abstract.....	94
Introduction.....	94
Methods.....	96
Results.....	97
Discussion.....	100
Conclusions.....	103
Acknowledgements.....	104
References.....	105
Appendix B.....	112
Thermochronologic methods.....	112
Glaciological parameters and precipitation data.....	117
Waxell-St. Elias Ridge.....	121
Additional references.....	124

Chapter 5

Quaternary Tectonic Response to Intensified Glacial Erosion in an Orogenic Wedge.....	133
Abstract.....	134
Introduction.....	135
Background.....	136
Analytical Methods.....	137
Bedrock Thermochronometry.....	139
Offshore Seismic.....	140
Architectural Model.....	141
Discussion and Conclusion.....	143
Acknowledgements.....	144
References.....	145

LIST OF MULTIMEDIA OBJECTS

Chapter 1

Figure 1.1 Generalized tectonic model of southern Alaska and the St. Elias orogen.....	9
Figure 1.2 Photograph of the core of the St. Elias orogen.....	10
Figure 1.3 Photograph of the Steller glacier.....	11
Figure 1.4 Photograph of the Bering glacier.....	12
Figure 1.5 Photograph of the Baldwin glacier.....	13
Figure 1.6 Photograph of typical glacial topography of the orogen.....	14

Chapter 2

Figure 2.1 Regional geologic map showing Chugach, Prince William, and Yakutat terranes	24
Figure 2.2 Photograph of the Schist of Liberty Creek.....	25
Figure 2.3 Photograph of the Prince William terrane.....	26
Figure 2.4 Photograph of a dike swarm.....	27
Figure 2.5 Photograph of a migmatite within the Chugach Terrane.....	28

Chapter 3

Figure 3.1 Map of the St. Elias orogen.....	68
Figure 3.2 Distribution of AHe ages in the central St. Elias orogen.....	69-70
Figure 3.3 <u>AHe age versus elevation</u>	71
Figure 3.4 Elevation profile versus AHe age.....	72
Figure 3.5 Map of geology and higher-temperature AFT, ZHe, and ZFT ages.....	73-74

Figure 3.6 Cooling history of the St. Elias orogen.....	75
Figure 3.7 Photographs of the CSEF and Bagley faults.....	76
Figure 3.8 Distribution of relocated earthquakes.....	77
Figure 3.9 Slope, exhumation, and tectonics of the central St. Elias orogen.....	78-79
Figure 3.10 New architectural model for the St. Elias orogen.....	80
Table 3.1 AHe, ZHe, and ZFT data for the central St. Elias orogen.....	81
Table 3.2 AHe data for the central St. Elias orogen.....	89-91
Table 3.3 ZHe and ZFT data for the central St. Elias orogen.....	92

Chapter 4

Figure 4.1 Distribution of AHe ages in the St. Elias orogen.....	109
Figure 4.2 Precipitation, topography, ELA, and AHe age distribution.....	110
Figure 4.3 Exhumation rate versus glacier-basin.....	111
Figure 4.4 AHe age versus elevation.....	127
Figure 4.5 Map of glacier drainage basins and precipitation.....	128
Figure 4.6 Topographic profile of hanging wall of the Bagley fault.....	129
Table 4.1 AHe data.....	130-131
Table 4.2 Glacier data.....	132

Chapter 5

Figure 5.1 Thermochronometry and tectonics of the St. Elias orogen.....	150
Figure 5.2 History of glaciation, bedrock cooling, and sedimentation during Yakutat driven orogenesis.....	151-152

Figure 5.3 Variation in bedrock cooling rate, topography, and climate across the St. Elias orogen153

Figure 5.4 Seismic reflection profiles from the continental shelf in the Gulf of Alaska.154

Figure 5.5 Proposed model of climate-related influences on orogen kinematics.....155

GRANT AND FUNDING INFORMATION

Funding for this research was provided by the National Science Foundation grant number EAR0409224 (STEEP project) (covered all field and laboratory expenses), the Virginia Tech Multicultural Academic Opportunities Program (MAOP) (provided four semesters of tuition and support), and the Virginia Tech Department of Geosciences 2008 British Petroleum Graduate Scholarship (provided one semester of tuition and support). Funding was also provided by the Virginia Tech Department of Geosciences in the form of three departmental teaching assistantships.

Chapter 1

Introduction

AARON L. BERGER

Department of Geosciences, Virginia Tech, Blacksburg, Virginia 24061, USA

In recent years, substantial research has focused on the mechanics, deformation, and architecture of orogenic systems, which are a fundamental component of plate tectonics (e.g. Wobus et al., 2003; Thiede et al., 2005; Huang et al., 2006). However, despite significant geological, geophysical, and computational studies (e.g. Dahlen et al., 1984; Westbrook et al., 1988; Koons, 1995; Whipple and Meade, 2004), temporal and spatial deformation within real world orogenic systems continue to be unpredictable, likely due to a complex interplay between crustal rheology, thermal-mechanical evolution, and surface mass-transfer. In particular, the importance of this latter process is poorly understood and has been the topic of intense scientific research and debate over the last few decades (e.g. Willett et al., 1993; Hardy et al., 1998; Zeitler et al., 2001; Konstantinovskaia and Malavieille, 2005; Naylor and Sinclair, 2007). To this end, an emerging paradigm in earth sciences predicts that the development and kinematics of deformational systems may reflect a marriage between atmospheric and tectonic processes (e.g. Molnar and England, 1990; Koons, 1990). To date, scientific contributions to this topic have largely been based on modeling (e.g. Naylor and Sinclair, 2007; Konstantinovskaia and Malavieille, 2005; Roe et al., 2006), as the co-evolution of climate and tectonically constructed topography in natural systems masks the real world orogenic response to focused denudation. Nonetheless, evidence continues to mount that denudation can strongly influence spatial deformation patterns, fault localization, fault initiation, and crustal extrusion (e.g. Willett et al., 1993; Hardy et al., 1998; Zeitler et al., 2001; Whipple and Meade, 2004). Despite the potential importance of climate on tectonics, the impact of the most severe transition in climate during Cenozoic time, the

Late Neogene and Pleistocene onset and advance of glaciers, has hitherto not been empirically defined via comprehensive analysis of orogen kinematics.

To obtain empirical data on the impact of climate change and glaciation on orogenesis and to quantify the processes of terrane accretion, we focus on a heavily glaciated orogenic wedge created by the ongoing collision of the Yakutat terrane and the North American plate in southwest Alaska (Figure 1.1), which has a well constrained history of orogenesis and climate change (e.g. Plafker et al., 1994; Lagoe and Zellers, 1996; Bruhn et al., 2004). Chosen for the presence of some of the highest rates of exhumation and sediment accumulation known (Jaeger et al., 1998; Spotila et al., 2004), the tractable size of the St. Elias orogen provides the resolution to examine tectonic and climatic signals in their entirety. As glacial erosion is generally believed to be more effective than fluvial erosion (Montgomery, 2002; Brocklehurst and Whipple, 2002), the onset and advance of alpine glaciers across the orogen provides an ideal venue to address the difficult and elusive problem of the importance of climatic and surficial processes during orogenesis.

The interplay between tectonic uplift and glacial denudation across the St. Elias orogen has constructed the highest coastal mountain range in the world, with peak elevations routinely over 3,000 m and locally exceeding 5,000 m (Mt. Logan at 5,959 m and Mt. St. Elias at 5,489 m) (Figure 1.2). Coupled with the extreme maritime climate and high latitude of the region, the orogen supports the largest northern hemisphere glaciers outside of Greenland and Iceland (Figures 1.3, 1.4, 1.5). These large, warm-based valley and piedmont glaciers are highly effective at erosion (e.g. Jaeger et al.,

1998; Sheaf et al., 2003) and have sculpted the rugged glacial morphology of the orogen (Figures 1.2, 1.6). The size and prevalence of glaciers across the St. Elias orogen provides an ideal natural laboratory to study the impact of late Cenozoic glaciation on mountain building and landscape development. Using low-temperature thermochronometry, along with subsidiary structural relationships, seismicity, and offshore seismic reflection data, this study presents a new holistic view of orogen kinematics, deformation, and architecture and makes discoveries regarding the spatial distribution of glacial erosion, the magnitude of the change in erosion from fluvial to glacial regimes, and the impact of Cenozoic glaciation on orogenic wedge kinematics and evolution. Many of these results have previously not been observed in a natural system and have far-reaching implications for the classic "chicken and egg" debate of Late Cenozoic climate change (Molnar and England, 1990), the glacial buzz-saw hypothesis (Brozović et al., 1997), as well as the processes governing orogenesis.

REFERENCES:

- Brocklehurst, S.H., and Whipple, K.X., 2002, Glacial erosion and relief production in the eastern Sierra Nevada, California, *Geomorphology*, 42, 1-24.
- Brozovic, N., Burbank, D.W., and Meigs, A.J., 1997, Climatic limits on landscape development in the Northwestern Himalaya, *Science*, 276, 571-574.
- Bruhn, R.L., Pavlis, T., Plafker, G., and Serpa, L., 2004, Deformation during terrane accretion in the Saint Elias orogen, Alaska: Geological Society of America *Bulletin*, v. 116, n. 7/8, p. 771-787.
- Dahlen, F.A., Suppe, J., and Davis, D., 1984, Mechanics of fold-and-thrust belts and accretionary wedges; cohesive Coulomb theory: *Journal of Geophysical Research*, ser. B, Solid Earth and Planets, v. 89, n. 12, p. 10,087-10,101.
- Hardy, S., Duncan, C., Masek, J., and Brown, D., 1998, Minimum work, fault activity and the growth of critical wedges in fold and thrust belts: *Basin Research*, v. 10, p. 365-373.
- Huang, C.Y., Yuan, P.B., and Tsao, S., 2006, Temporal and spatial records of active arc-continent collision in Taiwan: A synthesis: *GSA Bulletin*, v. 118, p. 274-288.
- Jaeger, J.M., Nittrouer, C.A., Scott, N.D., and Milliman, J.D., 1998, Sediment accumulation along a glacially impacted mountainous coastline: Northeast Gulf of Alaska: *Basin Research*, v. 10, p. 155-173.

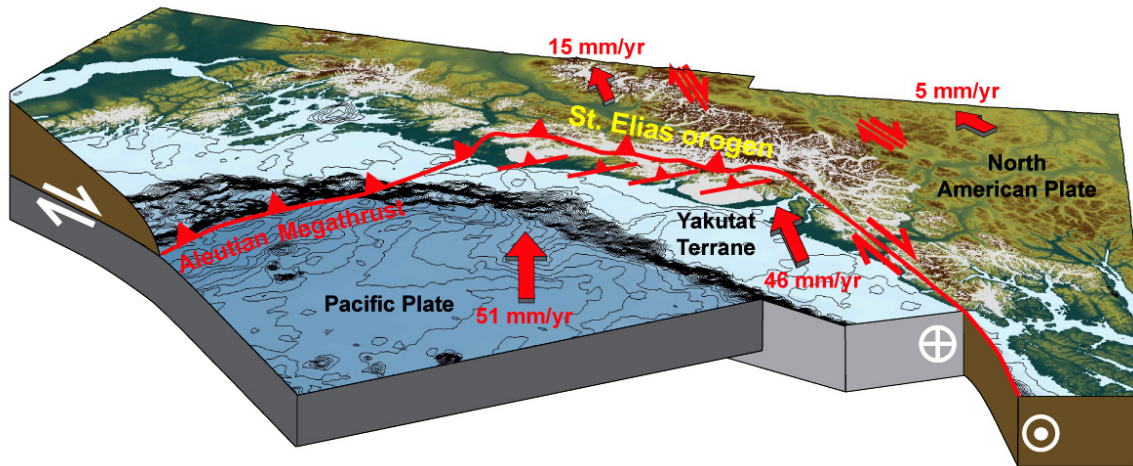
- Konstantinovskaia, E., and Malavieille, J., 2005, Erosion and exhumation in accretionary orogens: Experimental and geological approaches: *Geochemistry, Geophysics, Geosystems*, v. 6, Q02006.
- Koons, P.O., 1990, Two-sided orogen; collision and erosion from the sandbox to the Southern Alps, New Zealand: *Geology*, v. 18, p. 679-682.
- Koons, P.O., 1995, Modeling the topographic evolution of collisional belts: *Annual Review of Earth and Planetary Sciences*, v. 23, p. 375-408.
- Lagoe, M. B., and Zellers, S. D., 1996, Depositional and microfaunal response to Pliocene climate change and tectonics in the eastern Gulf of Alaska: *Marine Micropaleontology*, v. 27, p. 121-140.
- Molnar, P., and England, P., 1990, Late Cenozoic uplift of mountain ranges and global climate change: Chicken or egg?: *Nature*, v. 346, p. 29-34.
- Montgomery, D.R., 2002, Valley formation by fluvial and glacial erosion, 30, 1047-1050.
- Oskin, M., and Burbank, D.W., 2005, Alpine landscape evolution dominated by cirque retreat, *Geology*, 33, 933-936.
- Naylor, M., and Sinclair, H.D., 2007, Punctuated thrust deformation in the context of doubly vergent thrust wedges: Implications for the localization of uplift and exhumation: *Geology*, v. 35, p. 559-562.
- Plafker, G., Moore, J.C., and Winkler, G.R., 1994, Geology of the southern Alaska margin, in Plafker, G., and Berg, H.C., eds., *The Geology of Alaska: Boulder, Colorado, Geological Society of America, Geology of North America*, v. G-1, p. 389-449.

- Roe, G.H., Stolar, D.B., Willett, S.D., 2006, Response of a steady-state critical wedge orogen to changes in climate and tectonic forcing: Geological Society of America Special Paper 398, p. 227-239.
- Sheaf, M.A., Serpa, L., and Pavlis, T.L., 2003, Exhumation rates in the St. Elias Mountains, Alaska: Tectonophysics, v.367, p. 1–11.
- Spotila, J.A., Buscher, J.T., Meigs, A.J., and Reiners, P.W., 2004, Long-term glacial erosion of active mountain belts: Example of the Chugach-St. Elias Range, Alaska: Geology, v. 32, p. 501–504.
- Thiede, R.C., Arrowsmith, J.R., Bookhagen, B., McWilliams, M.O., Sobel, E.R., and Strecker, M.R., 2005, From tectonically to erosionally controlled development of the Himalayan orogen: Geology, v. 33, p. 689-692.
- Westbrook, G.K., Ladd, J.W., Buhl, P., Bangs, N., and Tiley, G.J., 1988, Cross section of an accretionary wedge: Barbados Ridge complex: Geology, v. 16, p. 631-635.
- Whipple, K.X., and Meade, B.J., 2004, Controls on the strength of coupling among climate, erosion, and deformation in two-sided, frictional orogenic wedges at steady state: Journal of Geophysical Research, vol. 109, doi: 10.1029/2003JF000019.
- Willett, S.D., Beaumont, C., and Fullsack, P., 1993, Mechanical model for the tectonics of doubly vergent compressional orogens: Geology, v.21, p. 371-374.

Wobus, C.W., Hodges, K.V., and Whipple, K.X., 2003, Has focused denudation sustained active thrusting at the Himalayan topographic front?: *Geology*, v. 31, p. 861-864.

Zeitler, P.K., Koons, P.O., Bishop, M.P., Chamberlain, C.P., Craw, D., Edwards, M.A., Hamidullah, S., Jan M.Q., Khan, M.A., Khattak, M.U.K., Kidd, W.S.F., Mackie, R.L., Meltzer, A.S., Park, S.K., Pecher, A., Poage, M.A., Sarker, G., Schneider, D.A., Seeber, L., and Shroder, J.F., 2001, Crustal reworking at Nanga Parbat, Pakistan; metamorphic consequences of thermal-mechanical coupling facilitated by erosion: *Tectonics*, v. 20, p. 712-728.

Figure 1.1: Generalized tectonic model of southern Alaska and the St. Elias orogen.



Tectonic model of southern Alaska and the St. Elias orogen showing the distribution of modern glaciers, seafloor bathymetry (100 meter contour interval), and plate vectors with respect to a stable North America. The core of the St. Elias orogen accommodates ~ 3 mm/yr of shortening across a thin-skinned fold and thrust belt along the leading edge of the Yakutat terrane. Vectors of plate motion within the orogen are poorly constrained and are as referenced on Figure 3.1.

Figure 1.2: Photograph of the core of the St. Elias orogen.



Photograph taken near the Bering glacier looking east along the St. Elias Mountains. The large ice field on the left (partially shrouded in clouds) is the Bagley ice field which is ~10 kilometers wide and ~200 kilometers long (picture looking down the length of the ice field). The large mountain in the background is Mt. St. Elias which is the third highest peak in North America at 5,489 meters. The suture between the accreting Yakutat terrane and the North American plate is located along the southern base of the ridge beneath the clouds.

Figure 1.3: Photograph of the Steller glacier.



Photograph taken from the Carbon Mountains looking to the north-northeast up the Steller glacier which is a large outlet glacier draining the Bagley ice field. The large mountain in the background is Mt. Steller at 3,236 meters and the hills on the right are Khitrov Hills. The Steller glacier is about 4 kilometers wide and 50 kilometers long and erodes into its base at ~ 4 km/Myr ($\pm 25\%$).

Figure 1.4: Photograph of the Bering glacier.



Photograph taken from the Khitrov Hills looking to the northeast up the 10 km wide and 70 km long Bering glacier which drains the Bagley ice field. The Bering glacier is eroding into its base at ~ 5 km/Myr ($\pm 25\%$). The Khitrov hills are the location of the youngest AHe (apatite helium) cooling ages in the orogen with ages as young as 440,000 years (cooling rate of 200° C/Myr). These results are discussed in chapter four.

Figure 1.5: Photograph of the Baldwin glacier.



Photograph looking north down the Baldwin glacier located on the leeward flank of the orogen near the U.S.-Canadian border. The hills throughout the drainage basin are actively mass wasting, contributing to the large lateral moraines shown in the photograph. Long-term erosion via mass wasting on the flanks of glaciers throughout the orogen is believed to approximately equal erosion at the bedrock / ice interface (steady-state erosion). Therefore, in cases where bedrock cooling ages record glacial conditions, cooling ages are believed to roughly correlate to long-term erosion at the bedrock-ice interface.

Figure 1.6: Photograph of typical glacial topography of the orogen.



Photograph of a valley glacier within the Granite Range on the leeward flank of the orogen. The picture was taken looking south to the range crest of the St. Elias orogen and illustrates the typical ruggedness of the landscape and the erosive power of glaciers that cover the orogen. The glacial equilibrium line altitude (ELA) is clearly visible in the center of the photograph where the glacier transitions from concave to convex at the snowline (grey to white transition on the glacier). At the glacial ELA, ice-flux for an individual glacier is at its maximum.

Chapter 2

Tectonic History of Southwest Alaska Prior to the onset of Yakutat

Driven Orogenesis

AARON L. BERGER

Department of Geosciences, Virginia Tech, Blacksburg, Virginia 24061, USA

Since the late Paleozoic, the southwestern margin of Alaska has been the site of prolonged crustal convergence and terrane accretion resulting from the long-lived subduction of the Kula and Pacific plates beneath the North American plate. As a result, a multitude of allochthonous island arcs, continental fragments, and oceanic plateaus (terranes) have been successively accreted onto the North American plate such that almost all of present-day Alaska is composed of a continent scale *mélange* (Moore and Twiss, 1995). The last 200 Myr of subduction-related tectonic events prior to the onset of Yakutat driven orogenesis is recorded in southwest Alaska (Figure 2.1). Inboard of the accreting Yakutat terrane, the North American plate is composed of two Mesozoic and early Cenozoic accreted assemblages known as the Chugach and Prince William terranes. This tectonic assemblage was subjected to high-temperature low-pressure metamorphism and related plutonism in the Eocene due to the subduction of the Kula / Pacific plate spreading ridge. These geologic events are important to the early cooling history of the region and the boundary conditions of the active St. Elias orogen and each is discussed briefly below.

ACCRETION OF THE CHUGACH TERRANE

The Chugach terrane is a ~124,000 km² amalgamation of three sub-terranes underplated and accreted beneath the North American plate via the Border Ranges fault system from ~200-62 Ma (e.g. Plafker et al., 1977; Wallace and Winkler, 1989; Plafker et al., 1994). These sub-terranes accreted in three distinct phases beginning with the Schist of Liberty Creek (~200-160 Ma), followed by the McHugh Complex (~160-120 Ma), and

finally the Valdez Group (~120-62 Ma). During accretion of each sub-terrane, the prominent tectonic transport direction was roughly perpendicular to the trend of subduction (Plafker et al., 1994).

The Schist of Liberty Creek (Figure 2.2) is composed of a sequence of trench to near-trench sediments of Triassic to Jurassic turbidites as well as offscraped material that was deposited off of the coast of Alaska and possibly as far south as British Columbia (Little and Naeser, 1989; Plafker et al., 1994). During accretion, the Schist of Liberty Creek were underthrust beneath the North American plate to a depth of 12-25 km and subjected to greenschist to local blueschist facies metamorphic conditions (Roeske, 1986). The compressional forces produced by this tectonic event resulted in widespread faulting, folding, and the development of a pronounced foliation within the Schist of Liberty Creek and locally within the North American plate (Sample and Fisher, 1986).

The next sub-terrane to accrete was the McHugh Complex. This sequence of rocks is made up of metamorphosed trench sediments with up to kilometer blocks of late Triassic to early Cretaceous greywacke, volcanics, and argillite deposited off the coast of Alaska and British Columbia (Plafker et al., 1994). During accretion, the McHugh Complex was underthrust beneath the North American plate to ~10-22 km and subjected to greenschist facies metamorphic conditions (Plafker et al., 1994). The accretion of the McHugh Complex resulted in a second phase of deformation that produced widespread faulting, folding, and the development of a slaty foliation within the McHugh Complex, the Schist of Liberty Creek, and locally in the North American plate (Sample and Fisher, 1986). Within the McHugh Complex, the age of metamorphism appears to decrease to

the south, suggesting that accretion took place over a prolonged period of time as successive material was incorporated into the system (Plafker et al., 1994).

The last sub-terrane within the Chugach terrane to accrete was the Valdez Group. This sequence of rocks contains late Cretaceous mudstone, turbidites, sandstone, and minor amounts of mafic volcanics deposited on the margins of a primitive island arc and along the coast of North America (Little and Naeser, 1989; Plafker et al., 1994). Like the previous two sub-terrane, as the primitive island arc collided with the North American plate, it was underthrust to a depth of ~10 km and subjected to zeolite to localized amphibolite facies metamorphism (Plafker et al., 1976; Plafker et al. 1994). During accretion, the rocks of the Valdez group, McHugh Complex, and Schist of Liberty Creek underwent a third phase of deformation resulting in widespread faulting, folding, and the development of a slaty foliation (Sample and Fisher, 1986).

ACCRETION OF THE PRINCE WILLIAM TERRANE

The Prince William terrane (Figure 2.3) is a ~140,000 km² section of Paleocene through middle Eocene crust composed of turbidites and trench-fill sediments consisting of ~15-20% mafic volcanics (Little and Naeser, 1989). Based on sparse paleomagnetic data, these sediments were deposited at about 16° south latitude from their present location (Plafker et al., 1994). The Prince William terrane was accreted to the North American plate via the Contact fault from ~61-35 Ma. An absolute age of this event is given by 42±5.5 and 48±7 Ma K-Ar cooling ages for two syn-accretion plutons (Little and Naeser, 1989). Based on seismic reflection, magnetic, and exploratory well data, the

majority of the Prince William terrane was underplated beneath the North American plate during accretion (Plafker et al., 1994). At this time, the Prince William terrane underwent low-greenschist to greenschist facies metamorphism resulting in the development of local slaty cleavage. The accretion of the Prince William terrane also produced local folding and faulting within the Chugach terrane, regional uplift, and right-lateral strike-slip movement along the Border Ranges fault system (Little and Naeser, 1989).

HIGH-TEMPERATURE / LOW-PRESSURE METAMORPHISM

As the Kula / Pacific plate spreading ridge subducted under southwest Alaska during Eocene time (~60-48 Ma), the overriding crust was heated as the slab window passed beneath the region (Wallace and Winkler, 1989). This thermal event resulted in high-temperature and low-pressure metamorphism (up to amphibolite grade) within the Prince William and Chugach terrains and a surge of near trench volcanism which produced swarms of mafic to intermediate dikes which have a mid-ocean-ridge-basalt (MORB) signature (Figures 2.4 and 2.5) (Little and Naeser, 1989). The passage of the Kula / Pacific slab window and the subsequent crustal heating resulted in regional east-west tectonic extension and a regionally variable fracture penetrating foliation (Wallace and Winkler, 1989).

REFERENCES:

- Bradley, D., Kusky, T., Haeussler, P., Goldfarb, R., Miller, M., Dumoulin, J., Nelson, S. W., and Kari, S., 2003, Geologic signature of early Tertiary ridge subduction in Alaska: Geological Society of America, Special Paper 371, 19-49.
- Bruhn, R. L., Plavis, T. L., Plafker, G., and Serpa, L., 2004, Deformation during terrane accretion in the Saint Elias origin, Alaska, GSA Bulletin, vol. 116, no. 7/8, 771-787, July/August.
- Carey, S. W., 1955. The orocline hypothesis in geotectonics, Proc. R. Soc. Tasmania, 89, 255-288.
- Davies, D. L., and Moore, J. C., 1984, do m.y. intrusive rocks from the Kodiak Islands link the Peninsular, Chugach, and Prince William terranes: Geological Society of America Abstracts with Programs, v. 16 p. 277.
- DeBari, A. M., and Coleman, R. G., 1989, Examination of the deep levels of an island arc: Evidence from the Tonsina Ultramafic-Mafic Assemblage, Tonsina, Alaska, Journal of Geophysical Research, vol. 94, NO. B4, 4373-4391, April 10.
- Engelbrechtsen, D. C., Cox, A., and Gordon, R. G., 1985, Relative motions between oceanic and continental plates in the Pacific basin: Geological Society of America Special Paper 206, p. 59.
- Haeussler, P. J., Bradley, D. C., and Goldfarb, R. J., 2003, Brittle deformation along the Gulf of Alaska margin in response to Paleocene-Eocene triple junction migration: Geological Society of America, Special Paper 371, 119-140.

- Hillhouse, J. W., and Coe, R. S., 1994, Paleomagnetic data from Alaska: The Geology of North America, vol. G-1, The Geology of Alaska, The Geological Society of America, 797-812.
- Little, T. A., and Naeser, C. W., 1989, Tertiary Tectonics of the Border Ranges Fault System, Chugach Mountains, Alaska: Deformation and Uplift in a Forearc Setting, *Journal of Geophysical Research*, vol. 94, NO. B4, 4333-4359.
- Magoon, L. B., 1986, Present-day geothermal gradient, Geologic studies of the lower Cook Inlet Cost No. 1 Well, Alaska outer continental shelf, U.S. Geol. Surv. Bull., 1596, 41-46.
- Mazzotti, S., and Hyndman, R. D., 2002, Yakutat collision and strain transfer across the northern Canadian Cordillera, *Geology*, vol. 30, no. 6, 495-498.
- Nokleberg, W. J., Jones, D. L., and Silberling, N. J., 1985, Origin and tectonic evolution of the Maclaren and Wrangellia terrains, eastern Alaska Range, Alaska: *Geological Society of America Bulletin*, vol. 96, 1251-1270.
- Page, R. A., Plafker, G., Fuis, G. S., Nokleberg, W. J., Ambos, E. L., Mooney, W. D., and Campbell, D. L., 1986, Accretion and subduction tectonics in the Chugach Mountains and Copper River Basin, Alaska: Initial results of the Trans-Alaska Crustal Transect, *Geology*, vol. 14, 501-505.
- Plafker, G., D. L. Jones, and E. A. Pessagno, 1977, A Cretaceous accretionary flysch and Mélange terrane along the Gulf of Alaska margin, The U.S. Geological Survey in Alaska: Accomplishments during 1976, U.S. Geol. Surv. Circ., 751-B, B41-B43.

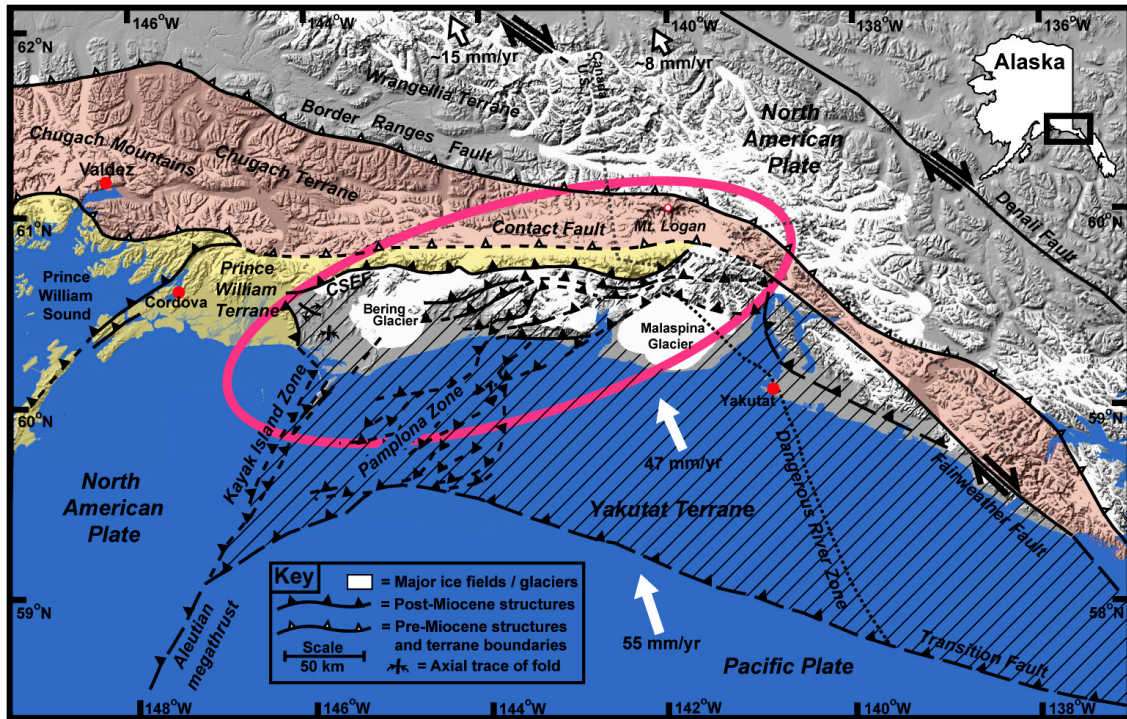
- Plafker, G., Moore, C. J., and Winkler, G. R., 1994, Geology of the southern Alaska margin: The Geology of North America, vol. G-1, The Geology of Alaska, 389-447, The Geological Society of America.
- Plafker, G., Jones, D. L., and Pessagno, E. A., Jr., A Cretaceous accretionary flysch and mélangé terrane along the Gulf of Alaska margin, in Blean, K. M., ed., The United States Geological Survey in Alaska: Accomplishments during 1976: U.S. Geological Survey Circular 751-B, P. B41-B43.
- Plavis, T. L., 1982, Cretaceous deformation along the Border Ranges fault, southern Alaska: Brittle deformation during formation of a convergent margin, *Tectonics*, 1, 343-368.
- Redfield T. F., and Fitzgerald, P. G., 1993, Denali fault system of southern Alaska: An interior strike-slip structure responding to dextral and sinistral shear coupling: *Tectonics*, vol. 12, no. 5, 1195-1208.
- Roeske, S. M., Snee, L. W., and Plavis, T. L., 2003, Dextral-slip reactivation of an arc-forearc boundary during Late Cretaceous-Early Eocene oblique convergence in the northern Cordillera: Geological Society of America, Special Paper 371, 141-169.
- Roeske, S. M., 1986, Field relations and metamorphism of the Raspberry Schist, Kodiak Islands, Alaska, in Evans, B. W., and Brown, E. H., eds., *Blueschists and eclogites*: Geological Society of America Memoir 164, p. 169-184.
- Sample, J. C., and D. M. Fisher, 1986, Duplex accretion and underplating in an ancient accretionary complex, Kodiak Islands, Alaska, *Geology*, 14, 160-163.

Tailler, I. L., 1973, Probable rift origin of the Canada Basin, Arctic Ocean, in *Arctic Geology*, edited by M. G. Pitcher, 526-533, Mem. Am. Assoc. Pet. Geol., 19.

Wallace, W. W., and Winkler, G. R., 1989, Structural Analysis of the Southern Peninsular, Southern Wangellia, and Northern Chugach Terranes along the Trans-Alaska Crustal Transect, Northern Chugach Mountains, Alaska, *Journal of Geophysical Research*, vol. 94, no. B4, 4297-4320.

Weinberger, J., and Sisson, V. B., 2003, Pressure and temperature conditions of brittle-ductile vein emplacement in the greenschist facies, Chugach metamorphic complex, Alaska: Evidence from fluid inclusions: Geological Society of America, Special Paper 371, 217-235.

Figure 2.1: Regional geologic map showing Chugach, Prince William, and Yakutat terranes.



Major structures and terranes of southeast Alaska, plotted on a shaded relief map. Fault and geologic data after Plafker et al. (1994) and Bruhn et al. (2004). Post-Miocene structures are shown with solid teeth and pre-Miocene terrane boundaries are shown with open teeth. The Chugach St. Elias fault (CSEF) represents the suture between the accreting Yakutat terrane and the Prince William terrane (North American plate). The Prince William terrane is shown in yellow, the Chugach terrane is shown in red, and the red oval outlines the core of the St. Elias orogen. The plate vectors are as referenced on Figure 3.1 and are drawn with respect to a stable North America.

Figure 2.2: Photograph of the Schist of Liberty Creek.



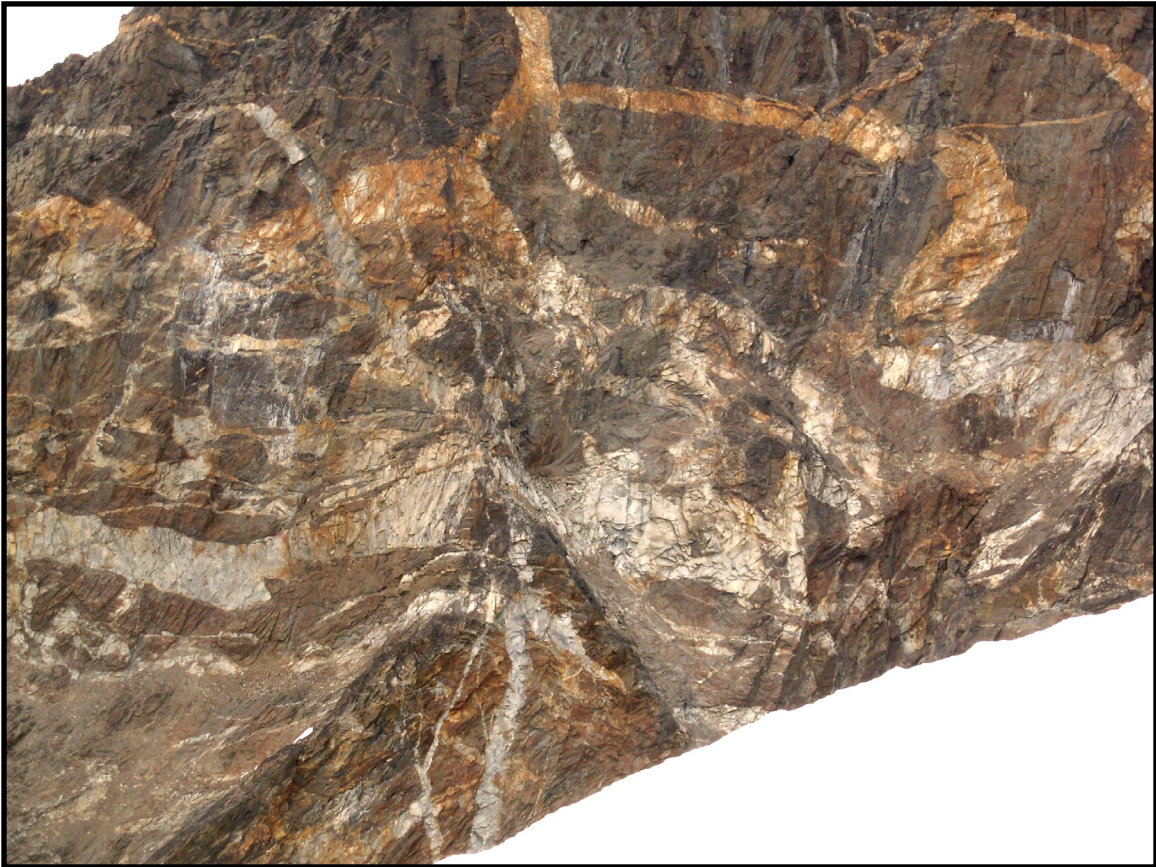
Photograph of the Schist of Liberty Creek taken above the Chitna River. The outcrop is approximately 3 meters high and shows a well developed foliation. Some of the rocks locally are mapped as blueschist facies. The green coloration seen in this exposure, however, reflects chlorite and not glaucophane.

Figure 2.3: Photograph of the Prince William terrane.



Photograph looking west along Barkley ridge of the Prince William terrane east of the Bering glacier. The quartz veins in the foreground and the deformed stratigraphy in the background are observed regionally throughout the Prince William terrane. The rocks are regionally mountain forming and are prehnite-pumpellyite to lower greenschists grade. To the east, the metamorphic grade increases to amphibolite facies within 30-40 kilometres near Mt. St. Elias.

Figure 2.4: Photograph of a dike swarm.



Photograph of a dike swarm on the leeward flank of the orogen near the Chugach / Wrangellia terrane contact and the U.S. / Canadian border. These dikes are believed to be related to the passage of the Kula / Pacific plate slab window beneath the region. The large dikes are 1-2 meters in width.

Figure 2.5: Photograph of a migmatite within the Chugach Terrane.



Photograph taken on a ridge overlooking the Tana glacier within the Chugach terrane. The migmatite in the center of the photograph is believed to be related to the passage of the Kula / Pacific plate slab window beneath the region. Based on thermochronometry presented in this dissertation, these rocks have been cooler than $\sim 240^{\circ}\text{C}$ for the last ~ 40 Ma

Chapter 3

Architecture, Kinematics, and Exhumation of a Convergent Orogenic Wedge: A Thermochronological Investigation of Tectonic-Climatic Interactions within the Central St. Elias Orogen, Alaska

AARON L. BERGER¹, JAMES A. SPOTILA¹, JAMES B. CHAPMAN², TERRY L. PAVLIS², EVA ENKELMANN³, NATALIA A. RUPPERT⁴, and JAMIE T. BUSCHER¹

¹Department of Geosciences, Virginia Tech, Blacksburg, VA, 24061, USA

²Department of Geological Sciences, University of Texas El Paso, El Paso, TX 79968, USA

³Earth and Environmental Sciences Department, Lehigh University, Bethlehem, PA, 18015, USA

⁴Alaska Earthquake Information Center, Geophysical Institute, University of Alaska Fairbanks, Fairbanks, AK, 99775, USA

Submitted to *Earth and Planetary Science Letters*, 2007

ABSTRACT

The kinematics and architecture of orogenic systems along the leading edges of accreting terranes may be heavily influenced by climate, but little research has been devoted to the long-term effects of glacial erosion on orogenesis. Here we use low-temperature apatite and zircon (U-Th)/He and fission-track thermochronometry, along with subsidiary structural relationships and seismicity, to develop a new architectural model of the St. Elias orogen in southern Alaska, which is one of the best examples of a glaciated orogenic wedge worldwide. These data illustrate that the orogen consists of a deformational backstop on the leeward flank and a rapidly deforming and eroding, thin-skinned fold and thrust belt on the windward flank. A structure beneath the Bagley ice field separates these distinct deformational domains, which we propose is a backthrust that makes the orogen doubly-vergent. Thermochronometry within the orogenic wedge suggests that denudation and deformation are strongly influenced by glacial erosion. Long-term exhumation, at rates of up to 4 mm/yr, is concentrated within a narrow zone along the windward flank, where glacier equilibrium lines intersect the orogenic wedge. The onset of enhanced glaciation also coincided with a marked acceleration in exhumation across the orogenic wedge, accelerated backthrust motion, and a major shift in deformation away from the North American-Yakutat terrane suture (Chugach St. Elias fault). We propose that accelerated glacial erosion forced the redistribution of strain along the backthrust and an en echelon array of forethrusts that lie beneath the zone of heaviest glaciation, which in turn are systematically truncated by the backthrust. This focusing of deformation matches predictions from analytical models of orogenic wedges

and implies a high degree of coupling between climate and tectonics in this glacially-dominated orogen.

INTRODUCTION

Accretion of terranes, such as allochthonous island arcs, continental fragments, and oceanic plateaus, is more common than continent-continent collisions and represents a significant process controlling the growth and development of continental crust (Coney et al., 1980). Orogenic systems make up the leading edges of colliding terranes, where the interplay of deformation, subduction, and erosion influences the mode and mass balance of accretion. In recent years, substantial research has focused on the architecture, mechanics, and deformation related to accretion-driven orogenesis (e.g. Dahlen et al., 1984; Westbrook et al., 1988; Koons, 1995; Whipple and Meade, 2004; Huang et al., 2006). Despite significant advancements, the mechanisms controlling strain partitioning, the 3-D structural development of orogenic wedges, and the influence of climate on orogenic evolution are still unresolved (e.g. Burbank et al., 2003; Konstantinovskaia and Malavieille, 2005; Roe et al., 2006; Hoth et al., 2006). Although evidence has mounted that climate and tectonics exist as a coupled system (e.g. Molnar and England, 1990; Koons, 1990; Hardy et al., 1998; Wobus et al., 2003; Thiede et al., 2005; Whipple and Meade, 2004; Naylor and Sinclair, 2007), uncertainties remain regarding how orogenic wedges evolve temporally and spatially in response to climatic gradients, the difference between fluvially and glacially-dominated erosion, and the field validity of numerical models of orogenesis (Willett et al., 1993; Zeitler et al., 2001; Hoth et al., 2006; Roe et

al., 2006). The Saint Elias orogen provides an excellent natural model to investigate these issues.

Located in southeastern Alaska and adjacent Canada along the Pacific-North American plate boundary, the St. Elias orogen is one of the western hemisphere's few examples of active terrane accretion (Plafker, 1987; Bruhn et al., 2004; Pavlis et al., 2004) (Figure 3.1). Produced from the ongoing oblique collision and partial accretion of the Yakutat terrane, the orogen is defined by a seismically active zone of interplate deformation with high rates of shortening, high coastal relief, and some of the most rapid Holocene erosion rates known (Lahr and Plafker, 1980; Hallet et al. 1996; Sauber et al., 1997; Jaeger et al., 1998; Sheaf et al., 2003). These attributes make the St. Elias orogen an ideal setting to examine the active processes of terrane accretion and Cordilleran-type tectonics. The high latitude and extreme maritime climate of the orogen also make it ideal for addressing the influence of differential glacial erosion on orogenesis and continental margin mountain building (Meigs and Sauber, 2000; Montgomery et al., 2001; Tomkin 2007; Gulick et al., 2004).

To constrain the kinematics and architecture of the St. Elias orogen, long-term deformation patterns and the location, timing, and geometry of major faults need to be determined. Previous work provides some constraints (e.g. Plafker et al., 1994; Meigs and Sauber, 2000; Doser and Lomas, 2000; Bruhn et al., 2004; Pavlis et al., 2004; Spotila et al., 2004), but extensive ice cover, a lack of preserved tectonic geomorphic features, and inaccessibility limit our knowledge of temporal and spatial deformation patterns. To gain a better understanding of this system, we have employed radiogenic helium ((U-Th)/He)

and fission-track thermochronometry with high spatial resolution sampling across the central portion of the orogenic wedge. The resulting exhumation pattern, coupled with structural relationships and seismicity, demonstrates the importance of climate on orogenic evolution and provides a new kinematic and architectural model for the St. Elias orogen as a windward-facing, doubly-vergent, thin-skinned orogenic wedge.

BACKGROUND: THE ST. ELIAS OROGEN

The Yakutat terrane is a composite oceanic-continental microplate overlain by up to 10 km of sedimentary cover, which was translated northwards along the dextral Fairweather-Queen Charlotte fault system until it encountered the Aleutian megathrust in the Middle Miocene (Plafker et al., 1994; O'Sullivan and Currie, 1996; Ferris et al., 2003) (Figure 3.1). The ensuing collision resulted in a foreland fold and thrust belt of offscraped sedimentary cover derived from the subducting Yakutat terrane basement (Plafker et al., 1994; Bruhn et al., 2004). Deformed sedimentary rocks consist of ~3 km of Eocene Kulthieth Formation (nonmarine deltaic to shallow marine sandstone with interbedded coal), overlain by ~2 km of Late Eocene to Early Miocene Poul Creek Formation (interbedded marine glauconitic siltstone and sandstone with minor volcanics), and capped by 0-5 km of synorogenic (~5.5 Ma through present) Yakataga Formation (interbedded glacial marine sandstone, siltstone, and diamictites) (Bruns and Schwab, 1983; Plafker, 1987; Zellers, 1993; Kressek et al., 1995). North of the Yakutat terrane, the North American plate is composed of three Mesozoic to Early Eocene accreted assemblages known as the Prince William, Chugach, and Wrangellia terranes (Figures

3.1 and 3.2). This forearc assemblage was subjected to high-temperature, low-pressure metamorphism, and associated plutonism in the Eocene (e.g. Plafker et al., 1994; Pavlis and Sisson, 2003). Roughly synchronous with the onset of the Yakutat collision, high topography is believed to have developed regionally at $\sim 10 \pm 4$ Ma (Lagoe et al., 1993; Rea and Snoeckx, 1995; White et al., 1997).

The active core of the St. Elias orogen can be divided into three structural domains. The central domain (the focus of this paper), located between the Bering and Malaspina glaciers, is an east-west trending, thin-skinned (<15-km-thick), roughly south-vergent fold and thrust belt (Figures 3.1 and 3.2) (Plafker et al., 1994; Bruhn et al., 2004). Within this thrust system, penetrative deformation, although present, is considered to be of subsidiary importance to fault-accommodated block motion (Plafker et al., 1994; Bruhn et al., 2004). Within the eastern and western domains, deformation becomes more complex (Figure 3.1). In the west, structures wrap around to form an immature indenter corner via the Kayak Island Zone, which connects to the Aleutian megathrust (Plafker et al., 1994; Gulick et al. 2007). In the east, thrust faults converge and connect with the Fairweather transform fault (Bruhn et al., 2004).

Major thrust faults of the orogen include the Chugach-St. Elias fault, representing the suture between the Yakutat and Prince William terranes, and more seaward forethrusts including the Kosakuts, Hope Creek, Miller Creek, Sullivan, and Malaspina faults (Figures 3.1 and 3.2). Offshore, the thrust belt consists of the Pamplona zone. North of the thrust belt, the Border Ranges fault is the Mesozoic subduction-thrust suture between the Chugach and Wrangellia terranes, and the Contact fault is the Paleogene

subduction-thrust suture between the Prince William and Chugach terranes (Pavlis, 1982; Plafker et al., 1994). The Contact fault has been interpreted to accommodate active westward extrusion of the orogen via dextral slip, but the modern slip rate and Quaternary history are not known for any of the faults in the St. Elias orogen. Currently, approximately 3 cm/yr of the 4.7 cm/yr Yakutat-North America convergence is accommodated by the fold and thrust belt, based on the poorly constrained, GPS-derived, active deformation field (Sauber et al., 1997; Fletcher and Freymuller, 2003; Elliott et al., 2006). The remaining ~1-2 cm/yr of Yakutat-North America convergence is transferred hundreds of kilometers into the interior of Alaska (Figure 3.1) (Mazzotti and Hyndman, 2002; Pavlis et al., 2004; Haeussler et al., 2004). These convergence vectors are believed to have remained roughly steady since the earliest Pliocene (Cox and Engebretson, 1985; DeMets et al., 1994).

Situated perpendicular to the powerful Gulf of Alaska storm track, the sharp relief of the St. Elias orogen receives orographic precipitation that is >3 m/yr at the coast, but decreases to <0.6 m/yr on the leeward flank (Péwé, 1975). Such heavy precipitation and high latitude have led to extensive glaciation. The large, warm-based valley and piedmont glaciers that cover the orogen move at rates upwards of 100s of meters per year and are highly effective at erosion (Fleisher et al., 2003) (Figure 3.1). Short-term glacial erosion rates are ~0.5 cm/yr (10^4 yr, orogen-wide) to 1 cm/yr (10^2 yr, basin-wide), based on sediment yield along the continental shelf and within fjords (e.g. Jaeger et al., 1998; Sheaf et al., 2003). The concentration of ice rafted sediment in the Gulf of Alaska indicates that the first scattered tidewater glaciers appeared at ~5 Ma (Lagoe et al., 1993;

Rea and Snoeckx, 1995; Kressek et al., 1995; Lagoe and Zellers, 1996). However, it was not until after the ~4.2-3.0 Ma Mid-Pliocene Warm Interval that the orogen became heavily glaciated. Since ~2.5 Ma, the orogen has been dominated by glacial erosion, and by the Pleistocene glaciers have routinely advanced to the edge of the continental shelf during glacial maxima. This prolonged history of extensive, syn-orogenic glaciation makes the St. Elias orogen unique amongst active orogenic belts worldwide.

The low-temperature cooling and exhumation history of the St. Elias orogen is locally constrained by existing (U-Th)/He and fission-track thermochronometry (O'Sullivan and Currie, 1996; Spotila et al., 2004; Johnston, 2005). The onset of Yakutat driven orogenesis has been interpreted to coincide with a pronounced acceleration in cooling at ~18 Ma, based on an apatite fission-track age-elevation transect from Mt. Logan (O'Sullivan and Currie, 1996) (Figure 3.1). Across the orogen, low-temperature bedrock cooling ages become younger towards the coast, implying greater exhumation where glaciers and orographic precipitation are focused (Spotila et al., 2004). Apatite (U-Th)/He ages as young as 1 Ma have previously been obtained from the leading edge of the deforming Yakutat terrane. Existing data, however, only document first-order exhumation patterns and fail to resolve differential rock uplift on individual faults or details of the exhumation pattern that bear on the architecture and history of deformation.

METHODS

New (U-Th)/He ages of apatite (AHe) and zircon (ZHe) and a zircon fission-track age (ZFT) were obtained from bedrock samples collected by helicopter along a north-

south transect across the orogen. We combined new data with previously measured AHe, ZHe, apatite fission-track (AFT), and ZFT ages from the central St. Elias orogen (K. Long and S. Roeske, pers. comm., 1992; Spotila et al., 2004; Johnston, 2005). These thermochronometers have typical closure temperatures of ~70 °C (AHe), ~110 °C (AFT), ~180 °C (ZHe), and ~240 °C (ZFT), largely varying with cooling rate, radiation damage, and grain size (Gleadow and Duddy, 1981; Hurford, 1986; Wolf et al., 1996; Farley, 2000; Ehlers and Farley, 2003; Reiners et al., 2004; Herman et al., 2007; Flowers et al., 2007). New AHe data includes re-analysis of several dated samples by Spotila et al (2004), which were weakly constrained by limited data (Appendix A).

AHe ages were measured at Virginia Tech on ~0.02 mg, multi- and single grain aliquots. We performed ~5 replicate analyses of each sample, to test reproducibility and the potential effects of inclusions or other defects common to detrital samples (Table 3.1). Samples were carefully screened for defects at 100x magnification and analyzed for ⁴He by ³He spike and quadrupole mass spectrometry. Parent nuclides were measured using isotope dilution (²³⁵U and ²³⁰Th) and ICP mass spectrometry at Yale University and Caltech. Cumulative analytical uncertainties are approximately ±10% (1σ). Age accuracy was cross-checked by periodic measurement of known standards, including Durango fluorapatite (30.9±1.53 Ma 1σ, n=40). ZHe ages were measured at Lehigh University using similar procedures. Errors reported for each average AHe and ZHe age are the standard deviation of replicate analyses (Table 3.1). One ZFT age was analyzed at Union College following standard procedures. The central age is reported for this sample, because it did not pass the χ^2 -test and may only be partially reset (where a reset age <

depositional age) reset. Additional description of methods and associated data are provided in Appendix A and Tables 3.2 and 3.3.

To constrain a sample's depth and rate of exhumation, we translated AHe ages to time-averaged exhumation rates using a closure-temperature approach, appropriate for a rapidly-cooled area (Spotila et al., 2004). Closure temperatures (51-94° C, Appendix A) were calculated for linear cooling histories using the approach of Dodson (1973) and apatite parameters from Farley (2000). Closure depths were estimated using a range of geothermal gradients (25-35 °C/km) (Magoon, 1986; Johnsson et al., 1992; Johnsson and Howell, 1996) and an ambient surface temperature of 0 °C (Péwé, 1975). The higher geothermal gradient was applied in areas of rapid cooling, because of the effect of isotherm advection during rapid denudation (Reiners and Brandon, 2006). To counter the effect of the rugged glacial topography on closure isotherm depth, samples were positioned relative to local mean elevation, as defined over 12 km wavelength. Numerical thermo-kinematic models were not utilized to estimate exhumation, given the uncertainties in background geothermal gradient, topographic history, and the potential presence of fluid convection in the permeable lithologies of the orogen.

RESULTS AND INTERPRETATIONS

New data

AHe, ZHe, and ZFT ages are well reproduced and provide robust new constraints on the pattern of low-temperature cooling across the central St. Elias orogen (Table 3.1). Average AHe ages were calculated from replicate analyses on each sample after

removing nine anomalously-old outliers from 110 total age determinations, which likely reflect ^4He contamination from micro-inclusions or U and Th zonation (Figure 3.2). After outlier removal, the average standard deviation of 24 of the 28 new AHe ages is $\pm 10.3\%$ (1σ), which is only slightly higher than analytical uncertainties. Even samples with very young average AHe ages reproduced well, such as 06STP74 (1.04 Ma $\pm 2.9\%$ 1σ , $n=4$) and 01CH32 (0.58 Ma $\pm 6.9\%$ 1σ , $n=5$) (Table 3.1). The good reproducibility of these ages indicates that purity and chemistry variations inherent within detrital apatite from multiple provenances are not a problem within most formations. However, four remaining samples reproduced more poorly ($1\sigma > 25\%$). Three of these consist of sandstones from the Yakataga Formation, indicating that intergrain age variability is high in this unit. Yakataga Formation samples also account for about half of the anomalously-old age determinations that were culled from the data. This unit may locally be only partially reset, such that the most retentive apatite grains retain a fraction of ^4He produced prior to deposition which contaminate the multigrain age determination. In general, the new AHe data are consistent with results from Spotila et al (2004), including re-analyses on several samples. However, re-analysis of three samples (01CH34, 01CH41, and 01CH29) using improved analytical techniques and a higher number of replicate analyses resulted in age constraints that replace earlier data (Appendix A).

General pattern of cooling ages

As observed by Spotila et al. (2004), AHe ages increase with distance from the coast (Figure 3.2). With the tighter spatial coverage of the new data, however, this

northward increase in cooling exhibits a sharper transition between young and old ages. Two general AHe age populations can be defined; a group of ages south of the Bagley ice field (windward flank of the orogen) that are younger than the onset of the Yakutat collision, and a group of ages north of the Bagley ice field (leeward flank of the orogen) that pre-date Yakutat-driven orogenesis. Young ages south of the ice field are from the Prince William and Yakutat terranes and range from 0.6 to 3.0 Ma. The oldest of this group occur proximal to the coast within the Yakataga and Poul Creek Formations and range from 2-3 Ma. Some of these samples may be partially reset, given poor age reproducibility (Table 3.1). To the north, AHe cooling ages decrease within the Poul Creek and Kulthieth Formations, culminating in a swath of the youngest AHe ages (0.6-0.8 Ma) just south of the Chugach St. Elias fault. These ages are younger than previously observed in the St. Elias orogen (Spotila et al., 2004; McAleer, 2006) and are comparable to the youngest cooling ages observed in any orogenic belt worldwide (e.g. Batt et al., 2000; Burbank et al., 2003; Willett et al. 2003). Ages within the Prince William terrane are slightly older (0.8-2 Ma), but the upper age bracket is poorly constrained.

The older population of AHe cooling ages north of the Bagley ice field range from 7 to 28 Ma (Figure 3.2). These ages indicate that samples from the leeward flank of the orogen, with the exception of 05STP23, 05STP36, and 99CH2, have not been reset by exhumation from closure depths of ~2 km since the Middle Miocene onset of Yakutat-driven orogenesis. Within this population, the youngest ages occur adjacent to the Bagley ice field and increase irregularly to the north. Assuming that extreme lateral changes in geothermal gradient are not present, the northward increase in age and the local age

perturbations are likely due to isochron tilting and variability in sample elevation (Table 3.1). A clear age-elevation gradient of 7 Ma/km is observed in three samples spanning ~1.5 km of elevation (Figure 3.3). This gradient may represent slow, steady exhumation during the Miocene of ~0.14 mm/yr, or it may represent an exhumed AHe partial retention zone (e.g. Ehlers and Farley, 2003). In either case, this age pattern suggests that younger ages are the result of deeper incision and sample location relative to fixed isochrons. The north-south age gradient is best fit by a 4° northward dip of isochrons, which implies minor south-side-up tilting (Figure 3.4). A decrease in tilting is inferred at the Wrangellia-Chugach terrane boundary, where isochrons appear to level-out.

Higher temperature thermochronometry is generally consistent with the spatial AHe age pattern, although differences exist that bear on the older and deeper exhumation history of the orogen. AFT ages along the same transect are consistently older, but show a similar spatial pattern of younger ages on the windward flank (4-6 Ma) versus the leeward flank of the orogen (13-40 Ma) (K. Long and S. Roeske, pers. comm., 1992; Johnston, 2005) (Figure 3.5). The sharp decrease in AHe ages proximal to the Chugach St. Elias fault, however, is not observed in the AFT data. ZHe ages, including those measured by Spotila et al. (2004) and three new ages presented here (Table 3.3, Appendix A) (Figure 3.5), are older than AHe and AFT ages. Most of the ZHe ages are older than deposition (non-reset) or predate the onset of Yakutat-driven orogenesis. However, the new ZHe ages from near the Chugach St. Elias fault are positionally reset (i.e. ZHe age < depositional age), including a young age of 5.1 Ma (Figure 3.5) (Table 3.1). These reset samples occur near the swath of youngest AHe ages and represent the

first syn-tectonic zircon cooling ages measured in the St. Elias orogen. In contrast, fully reset detrital ZFT ages have not been obtained from the Yakutat terrane and only one ZFT age from the Kulthieth Formation has been interpreted to be partially reset (Johnston, 2005) (Figure 3.5). The new ZFT age from the Prince William terrane (43 Ma) is younger than deposition but reproduced poorly and may therefore also be only partially reset.

Constraints on cooling history and maximum burial temperatures

Multiple thermochronometers constrain the synorogenic cooling history within the leading edge of the Yakutat terrane and the North American plate associated with exhumation from ~2-8 km depth. Assuming time-averaged cooling, in which samples cool linearly between closure temperatures, changes in cooling rate between different thermochronometers can be inferred (Figure 3.6). We assume AFT, ZHe, and ZFT closure temperatures of 110 °C, 180 °C, and 240 °C respectively, and use closure temperatures calculated individually for each AHe age (Appendix A). Using paired reset cooling ages from the Yakutat and Prince William terranes, cooling rates abruptly accelerated from ~10 °C/Ma to upwards of 100 °C/Ma at ~1-2 Ma (Figure 3.6). In contrast, paired thermochronometers from the Chugach terrane on the leeward flank of the orogen record post-40-Ma, linear cooling of 4-7 °C/Ma (Figure 3.6). This suggests limited syn-orogenic acceleration in cooling and implies differential exhumation histories between the leeward and windward flanks. The slow and steady cooling history of the

Chugach terrane also contrasts with the ~18 Ma acceleration in cooling observed at Mt. Logan (O'Sullivan and Currie, 1996), which may reflect a local structural event.

The distribution of depositionally non-reset ages across the leading edge of the Yakutat terrane constrains the upper burial temperatures experienced by different parts of the orogenic wedge (Figure 3.5). Using the threshold of reset cooling ages as a proxy for maximum sustained temperature, zones of thermal resetting at ~70 °C (AHe), ~110 °C (AFT), and ~180 °C (ZHe) are situated at ~0, 15, and 30 km inland from the coast, respectively. Reset detrital ZHe ages and the partially-reset ZFT age within the Kulthieth Formation also bracket the maximum temperature sustained by any part of the Yakutat terrane now exposed to between ~180-240 °C. This estimate is consistent with vitrinite reflectance data within the Yakutat terrane (Johnsson et al., 1992; Johnsson and Howell, 1996) and corresponds to prehnite grade metamorphic conditions.

Differences in low-temperature cooling across major faults

The closely-spaced new data constrains the timing of relative rock uplift across major faults. Two pairs of AHe ages were measured across the hanging wall and footwall of the Chugach St. Elias fault (Figure 3.2). Near the Bering glacier, this structure strikes approximately east-west, dips northward at ~40°, has pure-reverse slip, and juxtaposes intensely-folded lithologies of the Prince William and Yakutat terranes across a <10-m-wide, talus-covered zone (Bruhn et al., 2004) (Figure 3.7). Measured AHe ages in the hanging wall and footwall of the fault are analytically indistinguishable; 0.72 and 0.76 Ma on the west (05STP13, 05STP6) and 0.85 and 0.81 Ma on the east (05STP18,

05STP19) (Table 3.1, Figure 3.2). These sample pairs were taken from relatively undeformed blocks ~0.4-1.2 km from the fault plane. The identical cooling histories should therefore represent uniform denudation and a lack of relative rock uplift across the fault, rather than heating from fault motion or fault-related fluids. An additional AHe age pair from farther east (02CH34, 02CH33) that straddles the fault over a wider distance (~2.5 km) similarly shows a lack of differential cooling. In contrast, ZHe cooling ages for the western sample pair are different on either side of the fault (Figure 3.5). The younger ZHe age of the hanging wall sample (05STP6, 5.1 Ma) implies more recent cooling, indicative of relative rock uplift over the footwall sample (05STP13, 9.6 Ma). These results suggest that the Chugach St. Elias fault has been inactive over the past ~1 Ma, but may have been active at ~5 Ma during the closure of the younger ZHe age.

Differential rock cooling and denudation does appear to have occurred in the last few million years across the Bagley ice field (Figure 3.7). AHe ages just north of the ice field in the Chugach terrane range from 7-13 Ma, whereas those to the south in the Prince William terrane are 0.8 to ~2.0 Ma (Figure 3.2). These age groups are separated by a ~15-km-wide, ice field expanse. Although it is possible that the ice field covers an inflection in ages associated with a tilted partial retention zone, this would require a remarkable coincidence between the axis of tilting, inflection in ages, and the curved trend of the ice field. The ice field also delineates a jump in AFT and ZHe ages and separates the distinct windward and leeward flank cooling histories (Figure 3.6). We therefore prefer a simpler hypothesis in which the transition in ages is due to structural dislocation. Given the subsidiary importance of penetrative deformation versus fault

accommodated motion across the study area, we interpret this abrupt transition to represent differential, south-side-up rock uplift across a major fault residing beneath the ice field. Based on footwall and hanging wall cooling histories, substantial south-side-up fault motion likely began or significantly accelerated at ~1-2 Ma (Figure 3.6).

Relative rock uplift along faults within the Yakutat terrane is not as clearly defined. The steady northward decrease in cooling ages may reflect an increase in long-term exhumation rate, resulting from cumulative displacement on thrusts faults progressing up the fold and thrust belt (Figure 3.2). This is most apparent across the Miller Creek and Hope Creek faults in samples 01CH54, 06STP81, and 01CH29, which decrease in AHe age to the north from 2.9, to 1.3, to 0.7 Ma over 20 km. This pattern is ambiguous, however, as the trend is not continuous along the northeast strike of the faults. For example, sample pair 01CH29 and 06STP21 lie on opposite sides of the Hope Creek fault, but have the same age (~0.7 Ma) (Figure 3.2). Within each thrust sheet, AHe ages also increase along strike to the southwest, possibly reflecting a decrease in fault slip-rate towards the coast (e.g. 01CH41-06STP72 and 06STP21-06STP81).

DISCUSSIONS

Constraints on active deformation

The low temperature cooling history across the St. Elias orogen provides new constraints on deformation over the past few million years. Given that traditional neotectonic methods are hindered in the St. Elias orogen by pervasive glacier coverage

and erosion, our findings are a key element in advancing our understanding of the architecture and kinematics of the orogen.

One of the principal results of this study is the inactivity of the Chugach St. Elias fault for at least the last 1 Myr, which is arguably one of the most important structures in the St. Elias orogen. The cessation of activity along the Chugach St. Elias fault represents an orogen-wide shift in deformation away from the orogenic suture. The activity of this structure was previously uncertain, although the fault was believed to represent the structural backstop of the orogen (Bruhn et al., 2004).

A second key result is the identification of major south-side-up rock uplift across the Bagley ice field, which we interpret to be indicative of an active fault residing beneath the glacier. The geometry of this structure is unknown, but could be explained by: 1) a northward-dipping structure with top-to-the-north motion, 2) a vertical structure with south-side-up motion, or 3) a southward-dipping structure with reverse motion. The first of these possibilities would likely reflect the reactivation of the Contact fault. This is deemed unlikely, however, considering the tectonic setting and the thin-skinned nature of the orogen. The third interpretation is supported by relocated earthquakes beneath the Bagley ice field, which form a rough south-dipping alignment projecting to ~13 km depth, have faulting parameters indicative of underthrusting, and have compressive axes oriented in a north to north-north-west direction (Ruppert, in press) (Figure 3.8). We thus interpret the south-side-up motion across the Bagley trough to be the result of a previously unrecognized backthrust. Because a backthrust would have a different orientation than the Contact fault (Plafker et al., 1994), we refer to it as the “Bagley

fault". Although this structure is not exposed, the differential exhumation rates across it (see below) imply a 10^6 yr fault slip-rate of ~3-4 mm/yr, assuming steady state topography and a fault dip of 45°. The Bagley fault may also accommodate dextral motion, considering the oblique angle of Yakutat-North American convergence and the lack of observed strike-slip motion within the foreland thrust system (Bruhn et al., 2004).

Our interpretation of an active structure beneath the Bagley ice field is consistent with the occurrence of other major, active faults beneath linear ice-field valleys in Alaska (Plafker et al., 1994; Haeussler et al., 2004). It is also supported by the topographic differences north and south of the ice field. Deglaciaded ridges and nunataks of the Prince William terrane have greater maximum elevation, mean elevation, and mean slope relative to similar landforms in the Chugach terrane (Figure 3.9). This geomorphic contrast may not reflect mechanical differences in the respective terranes, given that the Chugach terrane contains bedrock of comparable erosional resistance (massive gneiss and granitic intrusions surrounded by schist) to the Prince William terrane (metasandstone, slates, phyllites, and schist). Furthermore, these terranes have comparable topographic expressions to the west of the orogen in the Chugach Mountains (Buscher et al., in press). The greater ruggedness of the Prince William terrane is thus consistent with south-side-up relative rock uplift via the proposed backthrust.

Active deformation within the Yakutat terrane is also constrained by thermochronometry. The pattern of AHe ages suggests exhumation rates increase northwards, due to cumulative net uplift, and decrease to the southwest, due to an along-strike reduction in fault motion (Figure 3.2). In this configuration, Yakutat-North

American convergence is partitioned between successive forethrusts in an en-echelon manner, consistent with interpretations by Bruhn et al. (2004) and Chapman and Vorkink (2006). This complicated partitioning of strain is supported by the southwest decay in elevation of prominent hanging-wall ridges (e.g. Dahlgren and Brower Ridges) (Figure 3.9) which might indicate a westward decrease in fault motion. It is also consistent with the decrease in exposed stratigraphic depth in the hanging wall of the Kosakuts, Hope Creek, and Miller Creek faults to the west (Figure 3.5) and explains why active deformation cross-cuts the structural and topographic fabric of the orogen.

These constraints on active deformation can be integrated with the cooling pattern of the entire orogen. Long-term (10^5 - 10^6 yr), time-averaged, exhumation rates were calculated from AHe ages assuming a closure temperature approach ($\pm 25\%$) and contoured with discontinuities across key faults to reflect differential block motion (Figure 3.9). Exhumation rates increase from approximately 1 mm/yr at the coast to 4 mm/yr just south of the Chugach St. Elias fault. On the leeward flank of the orogen, exhumation rates decrease from 0.3 mm/yr adjacent to the Bagley ice field to 0.1 mm/yr by the Chitina River, typical of background exhumation above the Aleutian subduction zone (Buscher et al., in press). Although isochrons suggest that the Chugach and Wrangellia terranes have been tilted northwards, the slow and steady syn-orogenic exhumation north of the Bagley ice field (or the lack of exhumation associated with a partial retention zone), and the distinct windward and leeward flank cooling histories imply that the leeward flank behaves as a deformational backstop that has been decoupled from the orogen since the onset of Yakutat driven orogenesis. Total syn-

orogenic rock uplift of the southernmost extent of the tilted block is likely limited to ~3-4 km, based on AHe ages, the current elevation, and assuming initial low relief.

Architecture of the St. Elias orogen

Based on these results, we propose a new architectural model of the central St. Elias orogen as a windward-facing, doubly-vergent, thin-skinned wedge, illustrated in cross sectional view in Figure 3.10. The line-of-cross-section is parallel to regional convergence vectors and extends from the offshore limit of deformation, the Pamplona Zone, into the deformational backstop. The cross section was created using offshore stratigraphy and structure from Bruns and Schwab (1983) and Risley et al. (1992) and onshore geologic mapping (Miller, 1971; Plafker et al., 1994; Bruhn et al., 2004; Plafker, 2005). Where available, industry data from wells (Risley et al., 1992) and earthquake locations (Figure 3.8) were used to constrain fold and thrust belt stratigraphy and architecture. The resulting cross section is a new interpretation of the St. Elias orogen, which has traditionally been depicted as a mono-vergent system (Plafker et al., 1994; Bruhn et al, 2004).

The interaction of structures at depth depicted in this bi-vergent model should modify deformation patterns at the surface through time. The apparent termination of the Chugach St. Elias fault in the last few million years may have been facilitated as a result of truncation by the south-dipping Bagley fault. As the Kosakuts, Hope Creek, and Miller Creek forethrusts converge on the Bagley fault, they may also be truncated. This could explain the lack of differential exhumation across these thrusts near their northern extent

(Figures 3.9 and 3.10). However, we do not consider these poorly constrained structural interactions at depth to be the impetus of the observed changes in deformation pattern. Given the acceleration in rock cooling in the last few Myr and our interpretation that this reflects accelerated motion across a backthrust, we propose that a fundamental shift in deformation occurred at this time due to a change in external boundary conditions.

Using calculated exhumation rates and assuming steady state topography, we can estimate the amount of convergence accommodated in the orogenic wedge by erosional efflux. Over the last 1 Myr, the total area eroded from the cross section has been $\sim 193 \text{ km}^2$ (Figure 3.10), which accounts for $\sim 2/3$ of the Yakutat-North America shortening, assuming 3 cm/yr convergence and a 10-km-thick tectonic influx. The unaccounted-for tectonic influx ($\sim 107 \text{ km}^2$) may be accommodated by subduction or lateral extrusion. The pattern of erosion also illustrates variations in depth of exhumation and requires variable particle trajectory paths within the orogenic wedge (e.g. Willett et al., 2003). To replace eroded material, the deepest, steepest particle paths should be focused beneath the swath of rapid exhumation just south of the Chugach St. Elias fault, consistent with the location of reset ZHe ages (Figure 3.5).

Role of glacial climate in orogenic wedge deformation

The new architectural model for the St. Elias orogen has implications for the orogen's kinematics and climate-tectonic coupling (Figure 3.10). The doubly-vergent wedge, with a windward-facing, rapidly-exhuming core and a leeward-facing backstop, closely matches predictions of numerical models of critical wedges undergoing

differential orographic precipitation and erosion (e.g., Koons, 1990; Beaumont et al., 1992; Willett et al., 1993). A backthrust separating the orogenic wedge from the backstop is a critical element in these models, because it enables the wedge to maintain a critical Coulomb form during spatially variable erosion (Koons, 1990; Konstantinovskaia and Malavieille, 2005; Naylor and Sinclair, 2007). The change in boundary conditions that may have been responsible for the fundamental shift in the kinematics of deformation in the St. Elias orogen is late Cenozoic climate change. The eleven-fold increase in cooling rate across the windward flank of the orogen at ~1-2 Ma (Figure 3.6) may reflect accelerated exhumation following the onset of intense glacial conditions after ~2.5 Ma (Lagoe et al., 1993; Rea and Snoeckx, 1995; Kressek et al., 1995; Lagoe and Zellers, 1996). Although it is possible that certain geometries of particle paths and lateral variations in isotherm depth could yield apparent increases in cooling rate towards the present, the magnitude of the acceleration is too large and the paths required to explain the increase in cooling do not fit model predictions (Konstantinovskaia and Malavieille, 2005; Naylor and Sinclair, 2007) (Appendix A). The acceleration in cooling also occurred in the North American plate, is observed regionally (e.g. McAleer, 2006), and coincided with a ~ten-fold increase in terrigenous sediment flux into the Gulf of Alaska (Lagoe et al., 1993; Shackleton et al., 1995). We therefore favor the interpretation that the increase in cooling rate reflects an increase in exhumation rate forced by climate change. Assuming a geothermal gradient of 30 °C/km, the acceleration in cooling would have corresponded to an average increase in denudation from ~0.3 to ~4 mm/yr, which is comparable to the estimated 5 mm/yr orogen-wide erosion rate for the Holocene (Sheaf et

al., 2003). This acceleration in exhumation may have forced heightened activity of the Bagley fault, to maintain critical Coulomb form as the upper reaches of the wedge were denuded.

This interpretation of the St. Elias orogen is consistent with model predictions that deformation and wedge geometry can be altered by shifts in climate (e.g. Whipple and Meade, 2004; Naylor and Sinclair, 2007). In these models, frontal accretion (i.e. tectonic influx) drives the horizontal transport of rock into the deforming wedge (i.e. rock advection) and exhumation accommodates this where erosion is rapid. The two bounding, conjugate reverse faults remain active only if erosional outflux is greater than, or equal to, tectonic influx (Willett et al., 1993; Whittington, 2004). If tectonic influx exceeds erosional outflux, the wedge will increase in height, progressively inhibiting motion on the conjugate reverse faults and initiating an outward propagation of deformation. However, if erosion exceeds influx, the wedge will diminish in volume and movement on the conjugate reverse faults will increase. Thus, as long as the wedge maintains its critical Coulomb form, a change in the balance of tectonic influx or erosional outflux will force a shift in deformation (e.g. Koons, 1990; Willett et al., 1993; Konstantinovskaia and Malavieille, 2005; Naylor and Sinclair, 2007).

The influence of climate on development of the St. Elias orogen is also evident in the focusing of denudation along the windward flank (Figures 3.9 and 3.10). The peak in exhumation just south of the Chugach St. Elias fault coincides spatially with mean Quaternary glacier equilibrium line altitudes (Berger and Spotila, 2006), which range from ~0.5-1.5 km in elevation on the windward flank of the orogen (Péwé, 1975). This

suggests that exhumation is focused by maximum ice flux and concentrated glacier erosion, which should occur around the equilibrium line altitude (Andrews, 1972; Meigs and Sauber, 2000; Tomkin, 2007). This focused denudation may have forced the proposed increase in fault motion to the northeast along several forethrusts (Figures 3.9).

The apparent climatic-tectonic coupling in the glacially-dominated St. Elias orogen has implications for the role of glacial erosion in orogenic wedge dynamics. Previous studies have shown that glacial erosion can be more effective than fluvial erosion and that glacial equilibrium altitude can limit the topography of mountain ranges (Brozovic et al., 1997; Meigs and Sauber, 2000; Montgomery et al., 2001; Tomkin, 2007). The focused denudation near glacier equilibrium line altitude, coupled with the apparent correlation between enhanced glaciation, accelerated denudation, and shifts in deformation, suggest that glacial erosion is also highly effective at dictating the partitioning of strain in orogenic belts. The impact of glacial erosion on the St. Elias orogen is also an example of the profound impact climate change can have on tectonic systems. Where present, glaciation may thus play a primary role in the evolution of orogenic wedges, supporting the paradigm that the development and kinematics of both active and inactive structures worldwide reflects a marriage between climatic and tectonic forces (e.g. Zeitler et al., 2001; Konstantinovskaia and Malavieille, 2005; Naylor and Sinclair, 2007).

CONCLUSIONS

The architecture and kinematics of deformation in the glaciated St. Elias orogen are more clearly elucidated by new thermochronometry. Cooling ages across the leeward flank of the orogen imply limited Yakutat-driven exhumation and only minor south-side-up tilting. In addition, paired thermochronometers from the Chugach terrane record slow and steady cooling rates throughout much of the Cenozoic. These data suggest that the leeward flank of the orogen functions as deformational backstop to the deforming wedge to the south. In contrast, cooling ages from the windward flank of the orogen, in both the deforming Prince William and Yakutat terranes, are much younger and signify more rapid exhumation. The boundary between these distinct deformational domains is the Bagley ice field, which we propose hides a major backthrust that we term the Bagley fault. This structure makes the St. Elias orogen a doubly-vergent, windward-facing orogenic wedge, which is a significant development in our understanding of this orogen's architecture.

The St. Elias orogen is also a type example of how climate and tectonics couple in orogenic systems. Within the orogenic wedge, thermochronometry illustrates two ways that climate plays a deterministic role in the deformation of the orogen. First, the most rapid exhumation is concentrated in a narrow region that corresponds to where glacier equilibrium line altitudes intersect the windward flank of the orogen. This implies that glacial erosion focuses denudation and deformation in the wedge. Second, the ten-fold increase in cooling rates across the orogenic wedge at ~1-2 Ma likely resulted from increased erosion following the onset of intense glacial conditions. Because the acceleration in motion on the Bagley fault and termination of the Chugach St. Elias fault

occurred at the same time, we postulate that accelerated glacial erosion across the upper reaches of the orogen redistributed Yakutat-North American shortening and resulted in truncation of forethrusts at depth. Climate change thus appears to have driven an orogen scale shift in the kinematics of deformation, which matches model predications and provides a unique view of how processes of terrane accretion function in a glacially-dominated climate.

ACKNOWLEDGEMENTS

We thank collaborators in studying the St. Elias orogen for many helpful discussions and ideas, including Ryan McAleer, Elizabeth Berger, Andrew Meigs, Ron Bruhn, Mike Vorkink, John Garver, Sean Gulick, Peter Koons, Julie Elliott, Jeff Freymueller, Peter Zeitler, and all other STEEP participants. Reviews by Rick Carlson, Sean Willett, and Frederic Herman greatly benefited this manuscript. Support was provided by National Science Foundation grant “The St. Elias Erosion/Tectonics Project”, EAR0409224.

REFERENCES

- Andrews, J.T., 1972, Glacier power, mass balances, velocities, and erosion potential, *Z. Geomorphol. N.F. Suppl. Bd.*, 13, p. 1-17.
- Batt, G.E., Braun, J., Kohn, B.P., and McDougall, I., 2000, Thermochronological analysis of the dynamics of the Southern Alps, New Zealand: *Geological Society of America Bulletin*, v. 112, p. 250-266.
- Beaumont, C., Fullsack, P., and Hamilton, J., 1992, Erosional control of active compressional orogens, in McClay, K.R. ed., *Thrust tectonics*: New York, Chapman and Hall, p. 1-18.
- Berger, A.L., and Spotila, J.A., 2006, The Western Chugach-St. Elias Orogen, Alaska: Strain Partitioning and the Effect of Glacial Erosion: AGU, 87(52), Fall Meet, Suppl., Abstract T11A-0416.
- Brozovic, N., Burbank, D.W., and Meigs, A.J., 1997, Climatic limits on landscape development in the Northwestern Himalaya, *Science*, 276, 571-574.
- Bruhn, R.L., Pavlis, T., Plafker, G., and Serpa, L., 2004, Deformation during terrane accretion in the Saint Elias orogen, Alaska: *Geological Society of America Bulletin*, v. 116, n. 7/8, p. 771-787.
- Bruns, T.R., and Schwab, W.C., 1983, Structure maps and seismic stratigraphy of the Yakataga segment of the continental margin, northern Gulf of Alaska: U.S. Geological Survey Miscellaneous Field Studies Map, MF-1424, 25p.

- Burbank, D.W., Blythe, A.E., Putkonen, J., Pratt-Sitaula, B., Gabet, E., Oskin, M., Barros, A., and Ojah, T.P., 2003, Decoupling of erosion and precipitation in the Himalayas: *Nature*, vol. 426, n. 6967, p. 652-655.
- Buscher, J.T., Berger, A.L., and Spotila, J.A., in press, Exhumation in the Chugach-Kenai Mountain belt above the Aleutian subduction zone, southern Alaska: A.G.U. Chapman Monograph.
- Chapman, J.B. and Vorkink, M., 2006, Tectonic geomorphology in an orogen dominated by glacial erosion, Saint Elias Mountains, Alaska: AGU Chapman Conference: Abstract, Active Tectonics and Seismic Potential of Alaska, May 11-14.
- Coney, P.J., Jones, D.L., and Monger, J.W.H., 1980, Cordilleran suspect terranes: *Nature*, v. 288, p. 329-333.
- Cox, A. and Engebretson, D.C., 1985, Change in motion of Pacific plate at 5 Myr BP: *Nature*, 313, 472-474.
- Dahlen, F.A., Suppe, J., and Davis, D., 1984, Mechanics of fold-and-thrust belts and accretionary wedges; cohesive Coulomb theory: *Journal of Geophysical Research*, ser. B, Solid Earth and Planets, v. 89, n. 12, p. 10,087-10,101.
- DeMets, C., Gordon, R.G., Argus, D.F., and Stein, S., 1994, Effect of recent revisions of geomagnetic reversal time-scale on estimate of current plate motions: *Geophysical Research Letters*, v. 21, p. 2191-2194.
- Dodson, M.H., 1973, Closure temperatures in cooling geological and petrological systems: *Contributions in Mineralogy and Petrology*, v. 40, p. 259-274.

- Doser, D.I., and Lomas, R., 2000, The transition from strikeslip to oblique subduction in southeastern Alaska from seismological studies: *Tectonophysics*, v. 316, p. 45–65.
- Ehlers, T.A., and Farley, K.A., 2003, Apatite (U-Th)/He thermochronometry: Methods and applications to problems in tectonic and surface processes: *Earth and Planetary Science Letters*, v. 206, p. 1–14.
- Elliott, J., Freymueller, J.T., and Larsen, C.F., 2006, Using GPS to untangle the tectonics of the Saint Elias orogen, Alaska, *Eos Trans., AGU*, 87(52), Fall Meet. Suppl., Abstract G42A-03.
- Farley, K.A., 2000, Helium diffusion from apatite: General behavior as illustrated by Durango fluorapatite: *Journal of Geophysical Research*, v. 105, p. 2903–2914.
- Ferris, A., Abers, G.A., Christensen, D. H., and Veenstra, E., 2003, High resolution image of the subducted Pacific plate beneath central Alaska, 50 – 150 km depth, *Earth Planetary Science Letters*, v.214, p. 575 – 588.
- Fleisher, J.P., Bailey, P.K., and Cadwell, D.H., 2003, A decade of sedimentation in ice-contact, proglacial lakes, Bering Glacier, AK: *Sedimentary Geology*, v. 160, p. 309-324.
- Fletcher, H.J., and Freymueller, J.T., 2003, New constraints on the motion of the Fairweather fault, Alaska, from GPS observations: *Geophysical Research Letters*, v. 30, p. 1139–1142.

- Flowers, R.M., Shuster, D.L., Wernicke, B.P., and Farley, K.A., 2007, Radiation damage control on apatite (U-Th)/He dates from the Grand Canyon region, Colorado Plateau: *Geology*, v. 35, p.447-450.
- Gleadow, A.J.W. and Duddy, I.R., 1981, A natural long-term annealing experiment for apatite. *Nuclear Tracks* 5, 169-174.
- Gulick, S., Jaeger, J., Freymueller, J., Koons, P., Pavlis, T., and Powell, R., 2004, Examining tectonic-climatic interactions in Alaska and the northeastern Pacific: *Eos*, v. 85, n. 43.
- Gulick, S., Lowe, L., Pavlis, T., and Mayer, L., 2007, Gardner, J., Geophysical insights into the Transition fault debate: Propagating strike-slip in response to stalling Yakutat block subduction in the Gulf of Alaska: *Geology*, v. 35, p. 763-766.
- Haeussler, P.J., Schwartz, D.P., Dawson, T.E., Stenner, H.D., Lienkaemper, J.J., Sherrod, B., Cinti, F.R., Montone, P., Craw, P.A., Crone, A.J., and Personius, S.F., 2004, Surface Rupture and Slip Distribution of the Denali and Totschunda Faults in the 3 November 2002 M 7.9 Earthquake, Alaska: *Bulletin of the Seismological Society of America*, v. 94, p. S23–S52.
- Hallet, B., Hunter, L., and Bogen, J., 1996, Rates of erosion and sediment evacuation by glaciers: A review of field data and their implications: *Global and Planetary Change*, v. 12, p. 213–235.
- Hardy, S., Duncan, C., Masek, J., and Brown, D., 1998, Minimum work, fault activity and the growth of critical wedges in fold and thrust belts: *Basin Research*, v. 10, p. 365-373.

- Herman, F., Braun, J., Senden, T.J., and Dunlap, W.J., 2007, (U-Th)/He thermochronometry; mapping 3D geometry using micro-X-ray tomography and solving the associated production-diffusion equation: *Chemical Geology*, v. 242, pp.126-136.
- Hoth, S., Adam, J., Kukowski, N., and Oncken, O., 2006, Influence of erosion on the kinematics of bivergent orogens: Results from scaled sandbox simulations: Geological Society of America, Special Paper 398, p. 201-225.
- Huang, C.Y., Yuan, P.B., and Tsao, S., 2006, Temporal and spatial records of active arc-continent collision in Taiwan: A synthesis: *GSA Bulletin*, v. 118, p. 274-288.
- Hurford, A. J. 1986. Cooling and uplift pattern in the Lepontine Alps South Central Switzerland and age of vertical movement on the Insubric fault line. *Contributions to Mineralogy and Petrology*, v. 92, p. 413-427.
- Jaeger, J.M., Nittrouer, C.A., Scott, N.D., and Milliman, J.D., 1998, Sediment accumulation along a glacially impacted mountainous coastline: Northeast Gulf of Alaska: *Basin Research*, v. 10, p. 155-173.
- Johnsson, M.J. and Howell, D.G., 1996, Thermal maturity of sedimentary basins in Alaska: An overview, U.S. United State Geological Survey, Report B 2142, p. 1-9.
- Johnsson, M.J., Pawlewicz, M.J., Harris, A.G., and Valin, Z.C., 1992, Vitrinite reflectance and conodont color alteration index data from Alaska: data to accompany the thermal maturity map of Alaska, United State Geological Survey Open-File Report 92-409.

- Johnston S.A., 2005, Geologic structure and exhumation accompanying Yakutat terrane collision, southern Alaska: Oregon State University, M.S. thesis, 49 p.
- Konstantinovskaia, E., and Malavieille, J., 2005, Erosion and exhumation in accretionary orogens: Experimental and geological approaches: *Geochemistry, Geophysics, Geosystems*, v. 6, Q02006.
- Koons, P.O., 1990, Two-sided orogen; collision and erosion from the sandbox to the Southern Alps, New Zealand: *Geology*, v. 18, p. 679-682.
- Koons, P.O., 1995, Modeling the topographic evolution of collisional belts: *Annual Review of Earth and Planetary Sciences*, v. 23, p. 375-408.
- Krissek, L. A., et al., 1995, Late Cenozoic ice-rafting records from Leg 145 sites in the North Pacific; late Miocene onset, late Pliocene intensification, and Pliocene-Pleistocene events: *Proceedings of the Ocean Drilling Program, Scientific Results*, v. 145, p. 179-194.
- Lagoe, M. B., Eyles, C. H., Eyles, N., and Hale, C., 1993, Timing of late Cenozoic tidewater glaciation in the far North Pacific: *Geological Society of America Bulletin*, v. 105, p. 1542-1560.
- Lagoe, M. B., and Zellers, S.D., 1996, Depositional and microfaunal response to Pliocene climate change and tectonics in the eastern Gulf of Alaska: *Marine Micropaleontology*, v. 27, p. 121-140.
- Lahr, J.C., and Plafker, G., 1980, Holocene Pacific–North American plate interaction in southern Alaska: Implications for the Yakataga seismic gap: *Geology*, v. 8, p. 483–486.

- Magoon, L.B., 1986, Present-day geothermal gradient, Geologic studies of the lower Cook Inlet Cost No. 1 Well, Alaska outer continental shelf, United State Geological Survey Bulletin, 1596, p. 41-46.
- Mazzotti, S., and Hyndman, R.D., 2002, Yakutat collision and strain transfer across the across the northern Canadian Cordillera: *Geology*, v. 30, p. 495-498.
- McAleer, R.J., 2006, Late Cenozoic Exhumation in a Transpressional Setting: Fairweather Range, Alaska: Virginia Tech, M.S. thesis, 70 p.
- Meigs, A., and Sauber, J., 2000, Southern Alaska as an example of the longterm consequences of mountain building under the influence of glaciers: *Quaternary Science Reviews*, v. 19, p. 1543–1562.
- Menke, W., and Schaff, D., 2004, Absolute earthquake locations with differential data: *Bulletin of the Seismological Society of America*, v. 94, p. 2254-2264.
- Miller, D.J., 1971, Geologic map of the Yakataga district, Gulf of Alaska Tertiary Province, Alaska: U.S. Geological Survey Miscellaneous Geologic Investigations Map I-610, scale 1:125,000.
- Molnar, P., and England, P., 1990, Late Cenozoic uplift of mountain ranges and global climate change: Chicken or egg?: *Nature*, v. 346, p. 29-34.
- Montgomery, D.R., Balco, G., Willett, S.D., 2001, Climate, tectonics, and the morphology of the Andes: *Geology*, v. 29, p. 579-582.
- Naylor, M., and Sinclair, H.D., 2007, Punctuated thrust deformation in the context of doubly vergent thrust wedges: Implications for the localization of uplift and exhumation: *Geology*, v. 35, p. 559-562.

- O'Sullivan, P.B., and Currie, L.D., 1996, Thermotectonic history of Mt. Logan, Yukon Territory, Canada: Implications of multiple episodes of middle to late Cenozoic denudation: *Earth and Planetary Science Letters*, v. 144, p. 251–261.
- Pavlis, T. L., 1982, Cretaceous deformation along the Border Ranges fault, southern Alaska: Brittle deformation during formation of a convergent margin, *Tectonics*, v. 1, p. 343-368.
- Pavlis, G.L., Picornell, C., Serpa, L., Bruhn., R.L., and Plafker, G., 2004, Tectonic processes during oblique collision: Insights from the St. Elias orogen, northern North American Cordillera: *Tectonics*, v. 23, p. 1-14.
- Pavlis, T.L. and Sisson, V.B., 2003, Development of a subhorizontal decoupling horizon in a transpressional system, Chugach metamorphic complex, Alaska: Evidence for rheological stratification of the crust: *Geological Society of America Special Paper 371*, p. 191-216.
- Péwé, T.L., 1975, Quaternary geology of Alaska: U.S. Geological Survey Professional Paper 835, 145 p.
- Plafker, G., 1987, Regional geology and petroleum potential of the northern Gulf of Alaska continental margin, *in* Scholl, D.W., et al., eds., *Geology and resource potential of the continental margin of western North America and adjacent ocean basins*: Houston, Texas, Circum-Pacific Council for Energy and Mineral Resources, Earth Science Series, v. 6, p. 229–268.

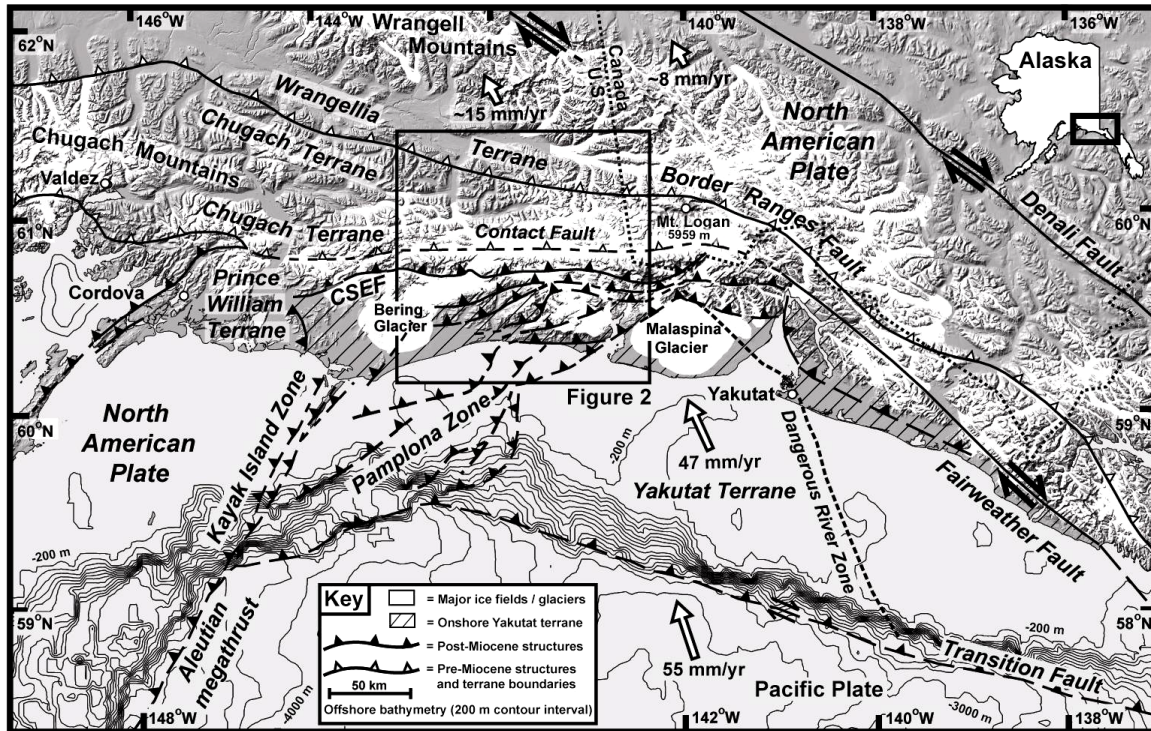
- Plafker, G., 2005, Geology of Bering Glacier and Icy Bay quadrangles, U.S. Geological Survey Open-File Report 2005-1342, scale 1:250,000. (pubs.usgs.gov/of/2005/1342)
- Plafker, G., Moore, J.C., and Winkler, G.R., 1994, Geology of the southern Alaska margin, in Plafker, G., and Berg, H.C., eds., *The Geology of Alaska*: Boulder, Colorado, Geological Society of America, *Geology of North America*, v. G-1, p. 389-449.
- Rea, D. K., and Snoeckx, H., 1995, Sediment fluxes in the Gulf of Alaska; paleoceanographic record from Site 887 on the Patton-Murray Seamount Platform, in Rea, D. K., Basov, I. A., Scholl, D. W., and Allan, J. F., eds., *Proceedings of the Ocean Drilling Program, Scientific Results*: College Station, TX., Ocean Drilling Program, p. 247-256.
- Reiners, P.W., and Brandon, M.T., 2006, Using thermochronology to understand orogenic erosion: *Annual Review of Earth Planetary Science*, v. 34, p. 419-466.
- Reiners, P.W., Spell, T.L., Nicolescu, S., and Zanetti, K.A., 2004, Zircon (U-Th)/He thermochronometry: He diffusion and comparisons with $^{40}\text{Ar}/^{39}\text{Ar}$ dating: *Geochimica et Cosmochimica Acta*, v. 68, p. 1857-1887.
- Risley, D. E., Martin, G.C., Lynch, M.B., Flett, T.O., Larson, J.A. and Horowitz, W.L., 1992, *Geologic Report for the Gulf of Alaska planning area: Mineral Management Service, Anchorage AK., OCS Report MMS 92-0065*, 302 p.

- Roe, G.H., Stolar, D.B., Willett, S.D., 2006, Response of a steady-state critical wedge orogen to changes in climate and tectonic forcing: Geological Society of America Special Paper 398, p. 227-239.
- Ruppert, N.A., in press, Stress map for Alaska from earthquake focal mechanisms: A.G.U. Chapman Monograph.
- Sauber, J., McClusky, S., and King, R., 1997, Relation of ongoing deformation rates to the subduction zone process in southern Alaska: Geophysical Research Letters, v. 24, p. 2853–2856.
- Shackleton, N. J., Hall, M. A., and Pate, D., 1995, Pliocene stable isotope stratigraphy of Site 846, in Pisias, N. G., Janacek, L. A., Palmer-Julson, A., and Van Andel, T. H., eds., Proceedings of the Ocean Drilling Program, Scientific Results, Leg 138, p. 337-355.
- Sheaf, M.A., Serpa, L., and Pavlis, T.L., 2003, Exhumation rates in the St. Elias Mountains, Alaska: Tectonophysics, v.367, p. 1–11.
- Spotila, J.A., Buscher, J.T., Meigs, A.J., and Reiners, P.W., 2004, Long-term glacial erosion of active mountain belts: Example of the Chugach-St. Elias Range, Alaska: Geology, v. 32, p. 501–504.
- Thiede, R.C., Arrowsmith, J.R., Bookhagen, B., McWilliams, M.O., Sobel, E.R., and Strecker, M.R., 2005, From tectonically to erosionally controlled development of the Himalayan orogen: Geology, v. 33, p. 689-692.

- Tomkin, J.H., 2007, Coupling glacial erosion and tectonics at active orogens: A numerical modeling study: *Journal of Geophysical Research-Earth Surface*, v. 112, F02015.
- Waldhauser, F. and W.L. Ellsworth, 2000, A double-difference location algorithm: Method and application to the northern Hayward fault, California: *Bulletin of the Seismological Society of America*, v. 90, p. 1353-1368.
- Westbrook, G.K., Ladd, J.W., Buhl, P., Bangs, N., and Tiley, G.J., 1988, Cross section of an accretionary wedge: Barbados Ridge complex: *Geology*, v. 16, p. 631-635.
- Whipple, K.X., and Meade, B.J., 2004, Controls on the strength of coupling among climate, erosion, and deformation in two-sided, frictional orogenic wedges at steady state: *Journal of Geophysical Research*, vol. 109, doi: 10.1029/2003JF000019.
- White, J. M., Ager, T. A., Adam, D. P., Leopold, E. B., Liu, G., Jette, H., and Schweger, C. E., 1997, An 18 million year record of vegetation and climate change in northwestern Canada and Alaska: Tectonic and global climatic correlates: *Palaeogeography Palaeoclimatology Palaeoecology*, v. 130, p. 293-306.
- Whittington, A.G., 2004, The exhumation of gneiss domes in bivergent wedges: Geometrical concepts and examples from the Himalayan syntaxes: *Geological Society of America Special Paper 308*, p. 35-46.
- Willett, S.D., Beaumont, C., and Fullsack, P., 1993, Mechanical model for the tectonics of doubly vergent compressional orogens: *Geology*, v.21, p. 371-374.

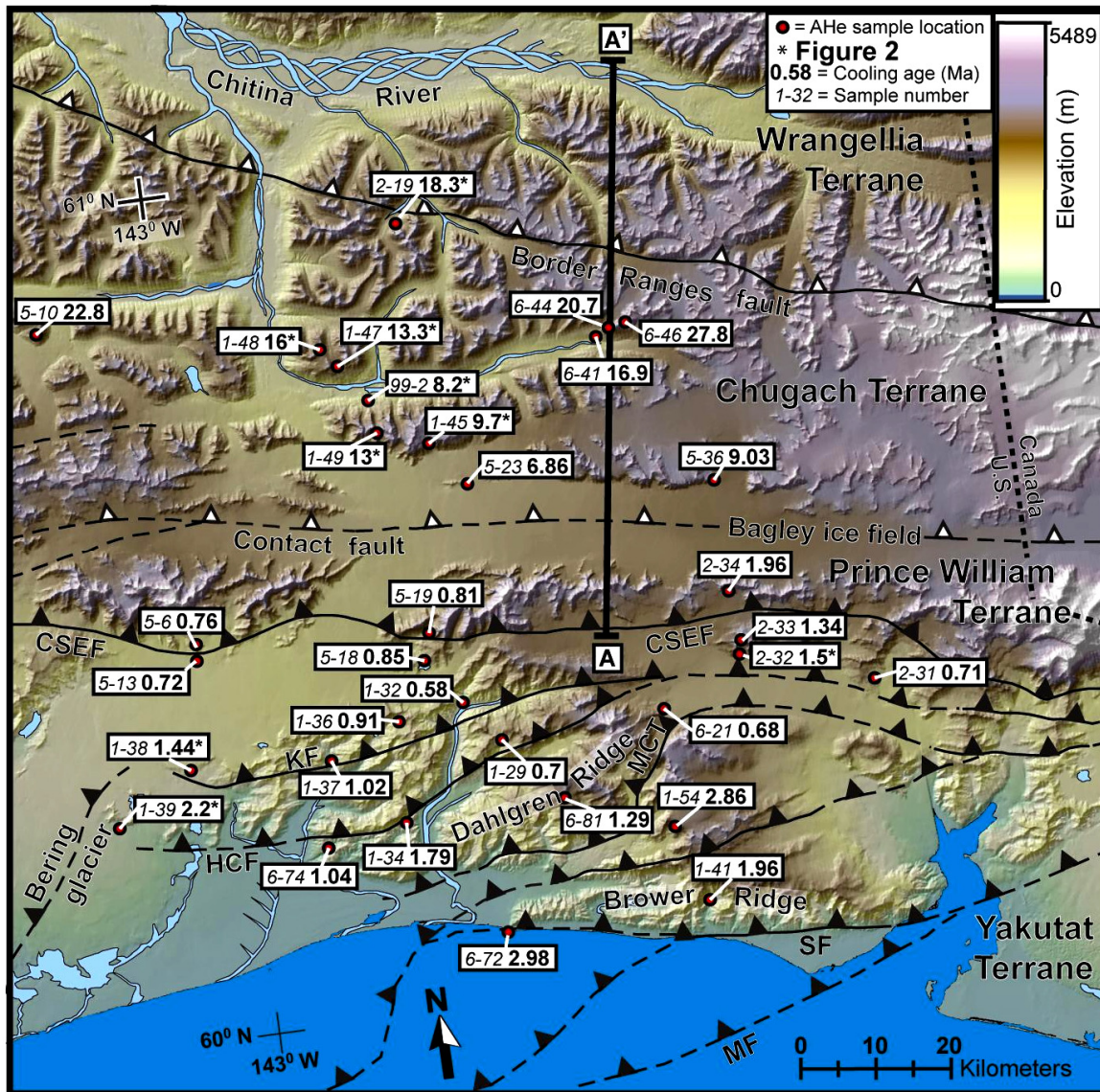
- Willett, S.D., Fisher, D., Fuller, C., En-Chao, Y., and Chia-Yu, L., 2003, Erosion rates and orogenic-wedge kinematics in Taiwan inferred from fission-track thermochronology: *Geology*, v. 31, p. 945-948.
- Wobus, C.W., Hodges, K.V., and Whipple, K.X., 2003, Has focused denudation sustained active thrusting at the Himalayan topographic front?: *Geology*, v. 31, p. 861-864.
- Wolf, R.A., Farley, K.A., and Silver, L.T., 1996, Helium diffusion and low-temperature thermochronometry of apatite, *Geochimica et Cosmochimica Acta*, v. 60, p. 4231-4240.
- Zeitler, P.K., Koons, P.O., Bishop, M.P., Chamberlain, C.P., Craw, D., Edwards, M.A., Hamidullah, S., Jan M.Q., Khan, M.A., Khattak, M.U.K., Kidd, W.S.F., Mackie, R.L., Meltzer, A.S., Park, S.K., Pecher, A., Poage, M.A., Sarker, G., Schneider, D.A., Seeber, L., and Shroder, J.F., 2001, Crustal reworking at Nanga Parbat, Pakistan; metamorphic consequences of thermal-mechanical coupling facilitated by erosion: *Tectonics*, v. 20, p. 712-728.
- Zellers, S.D., 1993, Controls on glacial-marine accumulation rates in the Yakataga Formation, Gulf of Alaska, in *Gulf Coast Section SEPM Foundation 14th Annual Research Conference*, p. 229-306.

Figure 3.1: Map of the St. Elias orogen



Major structures of St. Elias orogen in southeast Alaska, plotted on a shaded relief map which includes bathymetry of the Gulf of Alaska (100 m contour interval). Fault and geologic data after Plafker et al. (1994), Bruhn et al. (2004), and Plafker (2005). Post-Miocene structures are shown with solid teeth and pre-Miocene terrane boundaries are shown with white teeth. Plate motion vectors and rates are based on Lahr and Plafker (1980), DeMets et al. (1994), Plafker et al. (1994), and Haeussler et al. (2004). Boxed area (study area) is shown in Figures 3.2, 3.5, and 3.9. The Chugach St. Elias fault (CSEF) represents the suture between the accreting Yakutat terrane and the Prince William terrane (North American plate).

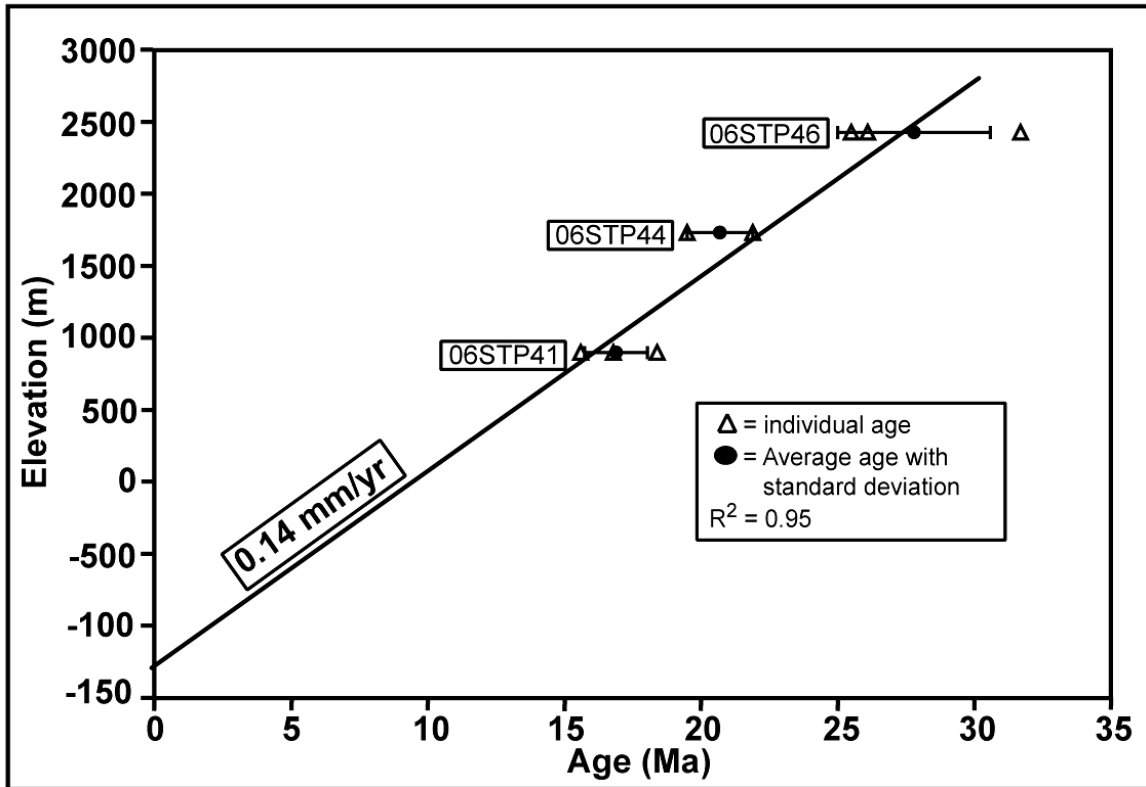
Figure 3.2: Distribution of AHe ages in the central St. Elias orogen



AHe ages plotted on a USGS 60-m resolution digital elevation model (DEM). New data are shown along with ages from Spotila et al. (2004). Terranes and major faults are shown. AHe ages increase with distance from the coast, with the youngest ages occurring in an east-west trending belt just south of the Chugach St. Elias fault (CSEF). Analytically indistinguishable cooling ages across the CSEF suggest that the fault has been inactive for >1 Ma. Cooling ages rapidly increase across the Bagley ice field, indicative of south-side-up motion across the glacier. Post-Miocene structures are shown with solid teeth and pre-Miocene terrane

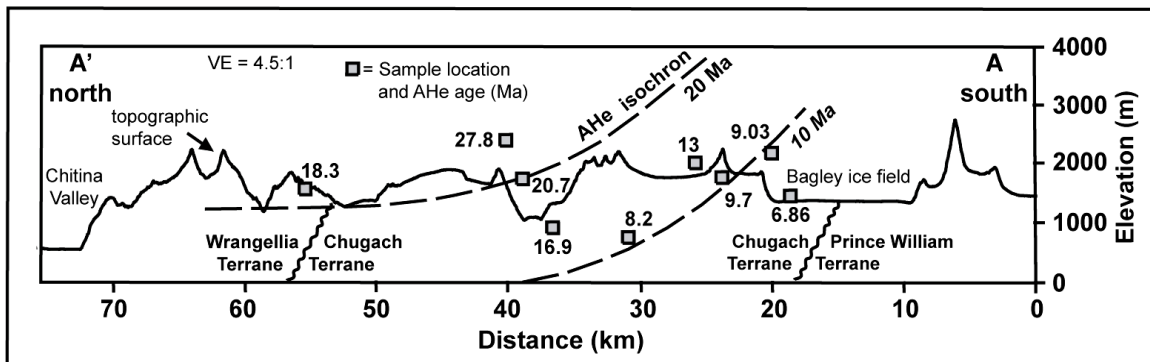
boundaries are shown with white teeth. Abbreviations: KF--Kosakuts fault, HCF--Hope Creek fault, MCT--Miller Creek thrust, SF--Sullivan fault, and MF--Malaspina fault.

Figure 3.3: AHe age versus elevation



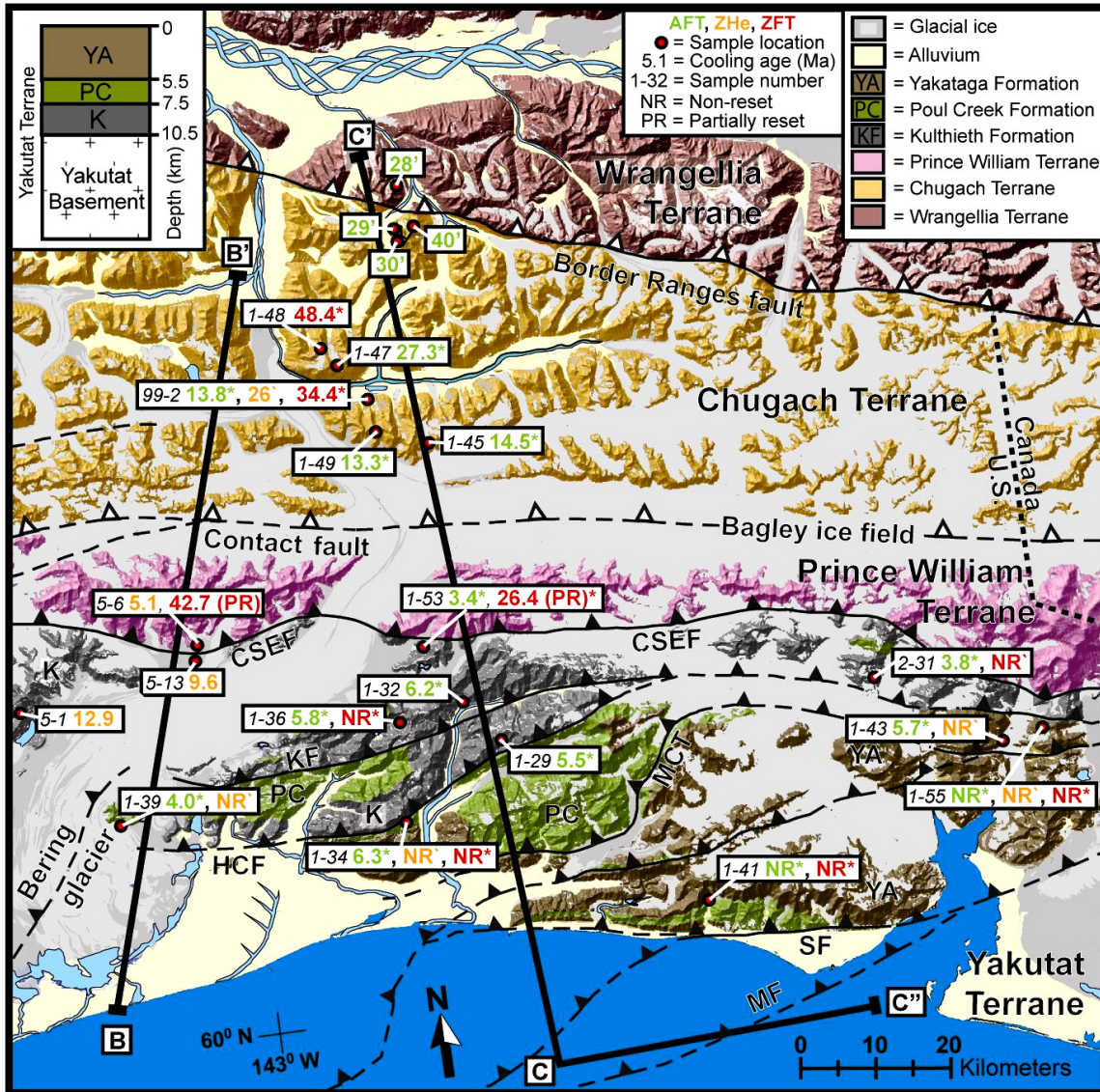
AHe age plotted against elevation for three samples from a vertical transect in the Chugach Terrane (Figure 3.2). The linear age-elevation trend suggests a 0.14 mm/yr Miocene exhumation rate. The time-zero intercept corresponds to a geothermal gradient of $\sim 21^{\circ}\text{C/km}$, consistent with regional estimates.

Figure 3.4: Elevation profile versus AHe age



North-south elevation profile with AHe ages and isochrons along line A-A' (Figure 3.2). Profile runs perpendicular to structures and terrane boundaries and was derived from a 60-m resolution DEM. Best-fit form lines denoting the 10 and 20 Ma AHe isochrons tilt upwards, suggesting greater exhumation on the south near the Bagley ice field. Sample positions are projected onto the profile using the regional structural trend. The three closely-spaced samples in the center of the profile correspond to the vertical transect shown in Figure 3.3. Vertical exaggeration is 4.5:1.

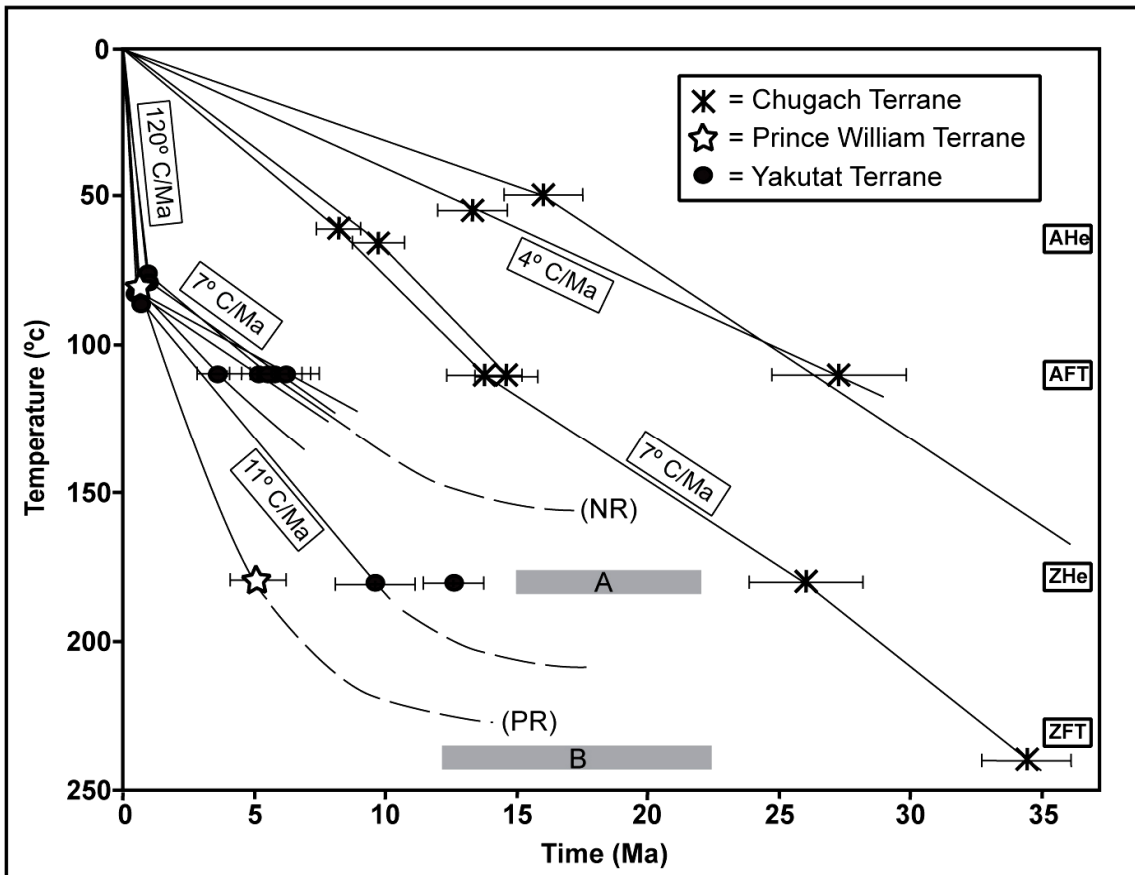
Figure 3.5: Map of geology and higher-temperature AFT, ZHe, and ZFT ages



Distribution of apatite fission-track (AFT), zircon (U-Th)/He (ZHe), and zircon fission-track (ZFT) cooling ages in the central St. Elias orogen. AFT ages are from Johnston (2005) (denoted by asterisk) and Roeske and Long (pers. comm.) (denoted by apostrophe) and are consistent with the general pattern of AHe ages (Figure 3.2). ZHe ages include five ages from Spotila et al. (2004) (denoted by reverse apostrophe) and three new ages from this study (Table 3.1). ZFT ages are from this study and Johnston (2005) and are either depositionally non-reset or predate Yakutat driven orogenesis, providing a valuable constraint on the maximum burial depth of samples. Ages are shown on the same shaded relief map as shown in Figure 3.2, but with colors representing the

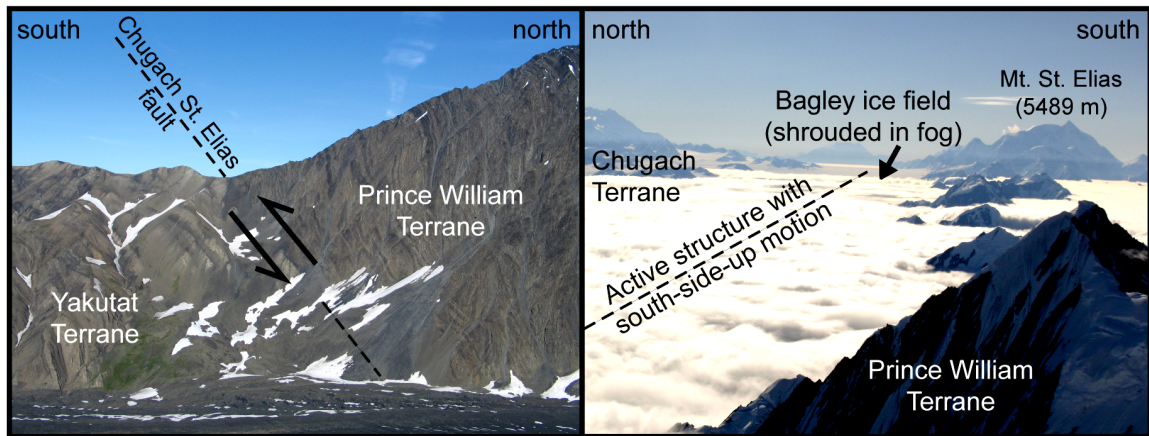
surficial and bedrock geology after regional geologic mapping (Plafker et al., 1994; Plafker, 2005). The distribution of glaciers is based on a combination of mapped ice from 1:250,000 scale USGS topographic maps and slope distributions based on ArcGIS analysis. Areas above the glacier elevation threshold with a slope of 0-10° are mapped as glacial ice, whereas areas of 0-10° slope below the glacier limit are shown as alluvium. The stratigraphic column for the Yakutat terrane in the upper left is based on Bruns and Schwab (1983), Plafker (1987), Zellers (1993), and Krissek et al. (1995). Fault abbreviations are as in Figure 3.2.

Figure 3.6: Cooling history of the St. Elias orogen



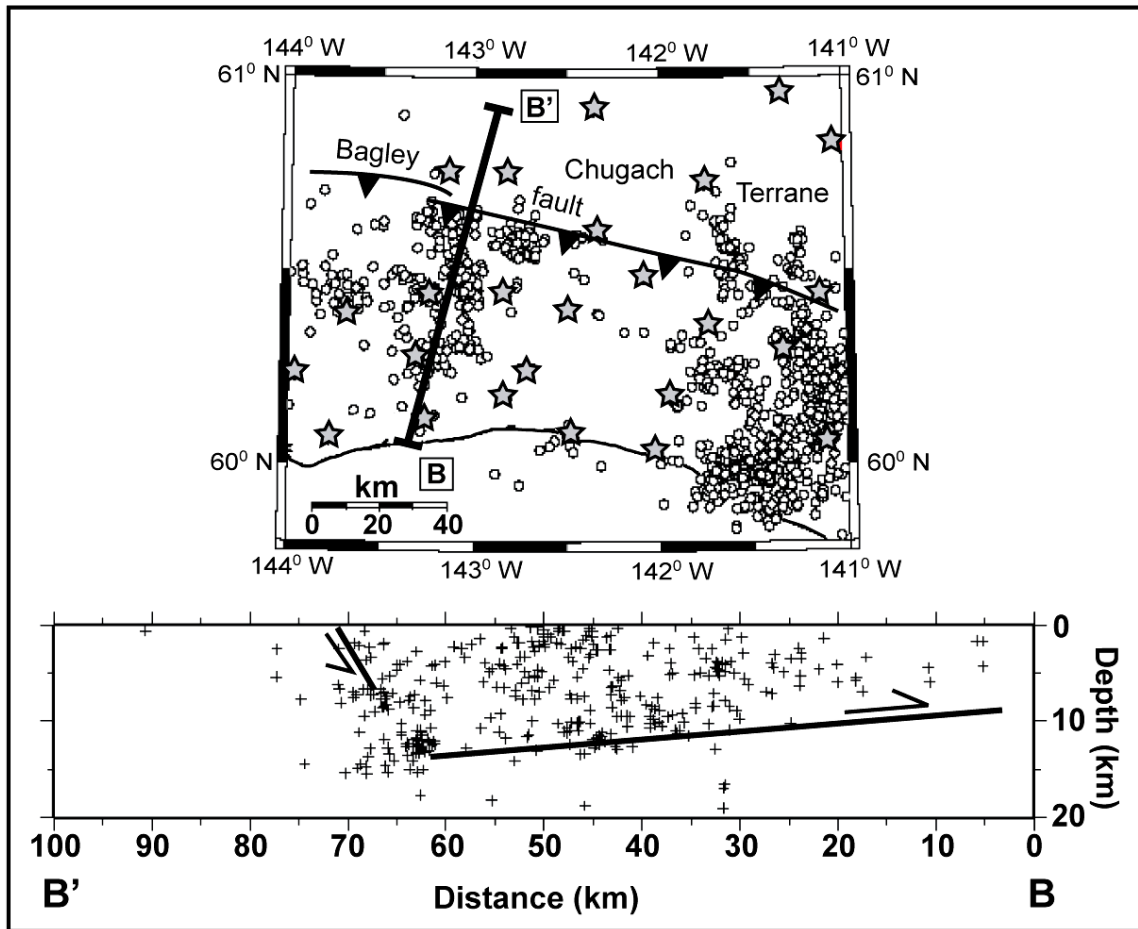
Cooling history for individual samples with paired thermochronometers from both the windward (Yakutat and Prince William terranes) and leeward (Chugach terrane) flanks of the orogen, using both new and previously published data, as shown and cited in Figures 3.2 and 3.5. Closure temperatures for reset AFT, ZHe, and ZFT ages are assumed to be 110 °C, 180 °C, and 240 °C respectively, and were calculated individually for AHe ages. Since no depositionally reset (NR) ZFT ages have been measured within the Yakutat terrane (Johnston, 2005) and the ZFT age from the Prince William terrane is believed to be partially reset (PR), the cooling paths of the windward samples must flatten back in time so as to remain cooler than 240 °C, as represented by bar “B”. Similarly, the cooling trajectory of samples from the Yakutat terrane with non-reset ZHe must flatten, as shown by bar “A”. Cooling history for the Chugach terrane is slow and steady from 40 Ma to the present. Cooling history on the windward flank accelerates by a factor of ~11 between ~1 and 2 Ma, coinciding with the intensification of glaciation following the Mid-Pliocene Warm Interval. The difference in cooling history between the Prince William and Chugach terrane implies that differential rock uplift across the Bagley ice field accelerated in the last few Myr.

Figure 3.7: Photographs of the CSEF and Bagley faults



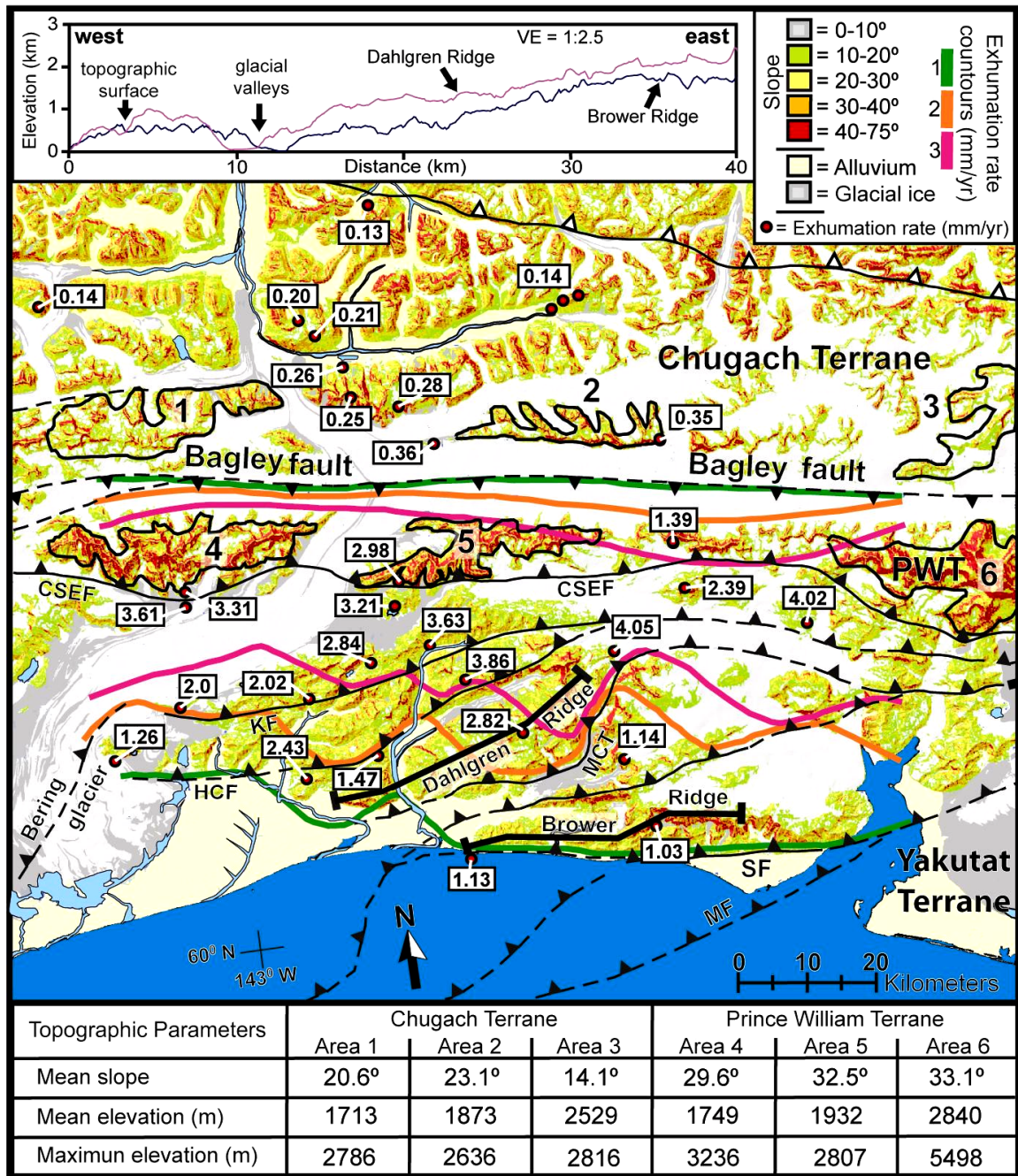
A) Photograph looking west at the inactive Chugach St. Elias fault (CSEF), taken 12 km east of the Bering glacier at Barkley Ridge. The fault juxtaposes intensely folded Yakutat and Prince William terranes across a narrow zone. For scale, the height of the saddle above the glacier is ~370 m. B) Photograph looking east at the Bagley ice field, taken from just west of the Bering glacier. An active fault with south-side up motion is inferred to be concealed by the ~15-km-wide and 200-km-long glacier-filled trough. This structure is deemed the Bagley fault.

Figure 3.8: Distribution of relocated earthquakes.



Map of ~1500 relocated earthquakes (white circles) greater than magnitude 1.5 from 1990 through 2007 and regional seismic stations (stars). Earthquake locations were determined using double difference method (Waldhauser and Ellsworth, 2000), which yields better relative locations than the original catalog locations (Menke and Schaff, 2004). Original earthquake parameters were taken from the Alaska Earthquake Information Center (AEIC). Relocated events exclude icequakes and events that predate digital data recording or were recorded by only a few stations. Locations are based on catalog P- and S-wave arrivals with the standard plane layer velocity model utilized by AEIC. Location errors are less than 5 km. Line B-B' (Figure 3.5) illustrates the depth distribution of seismicity within 20 km on either side of the section. The majority of the events are concentrated in the upper 13 km of the crust above a decollement (from Figure 3.10) and are localized within a 50-km-long part of the section that corresponds to the windward flank of the orogen. The distribution of seismicity beneath the Bagley ice field (delineated by the proposed Bagley fault, from Figure 3.9 and 3.10) is consistent with events occurring within the hanging wall and fault plane of a south-dipping backthrust.

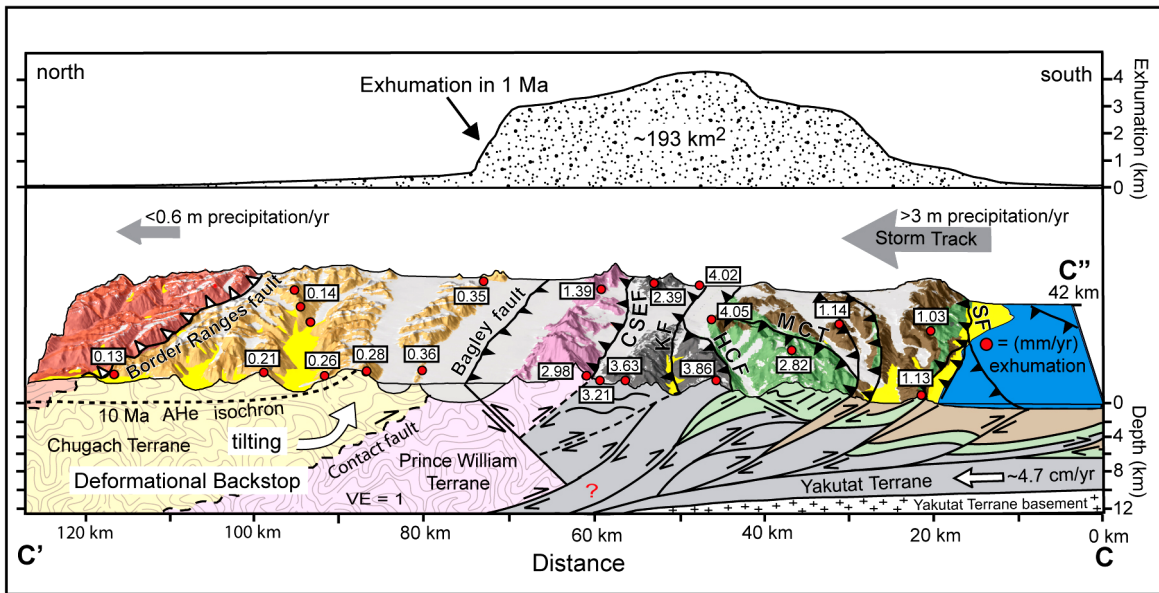
Figure 3.9: Slope, exhumation, and tectonics of the central St. Elias orogen



Exhumation rates and slope distribution in the central St. Elias orogen. Exhumation rates are calculated for AHe ages only, using a closure temperature approach. Best-fit contours of exhumation rate schematically illustrate interpreted steps in exhumation rate associated with rock uplift across the proposed Bagley fault and across active thrust faults south of

the CSEF. Slope was calculated from the elevation difference between one cell and eight surrounding cells using ArcGIS and a 60-m resolution DEM. The mean slope and mean and maximum elevation of six mainly glacier-free polygons are tabulated at the bottom, showing that the topography of the Prince William terrane (PWT) is more rugged than in the Chugach terrane, consistent with south-side up uplift across the inferred Bagley fault. Active faults within the Yakutat terrane generally do not correspond to higher slopes, given the occurrence of weaker, less-indurated Cenozoic stratigraphy of the fold and thrust belt. Elevation profiles along two ridges in the Yakutat terrane are shown in the upper left, illustrating a steady westward topographic decay that may represent an along-strike decrease in fault motion. Abbreviations, the distribution of alluvium and glaciers, and fault representations are as in Figures 3.2 and 3.5.

Figure 3.10: New architectural model for the St. Elias orogen.



Cross section along C-C'-C'' through the central St. Elias orogen (Figure 3.5), constructed parallel to regional convergence direction. This cross section summarizes the key findings of this study as a new architectural model, in which the orogen behaves as a, doubly-vergent, thin-skinned, windward-facing orogenic wedge that is heavily influenced by glacial erosion. Geologic structure is shown at 1:1 scale, but elevation and relief are exaggerated by 1.5x to be more visible. Major terranes, bedrock geology, faults, and distribution of glaciers at the surface are as shown in Figure 3.5. Inactive terrane boundaries are shown as irregular dashed lines. Active and inactive thrust faults are shown as heavy solid and dashed lines respectively. The proposed Bagley fault is shown as a southward-dipping thrust. The inactive CSEF is shown as offset by the Bagley fault at depth. Southward-vergent thrust faults of the Yakutat terrane are interpreted to flatten and merge at depth, except where truncated by the backthrust. However, the deep structure of the thrust system is poorly constrained. The thickness of the deforming cover sequence of the Yakutat terrane is based on the dip of the underlying megathrust and subducting oceanic slab (Plafker, 1987). Numbers by AHe sample locations are exhumation rates (mm/yr), from Figure 3.9. The plot above the cross section shows the volume per length area eroded from the section in 1 Myr, based on these exhumation rates. Plate motion vector from Figure 3.1. Abbreviations are as in Figure 3.2.

Table 3.1: AHe, ZHe, and ZFT data for the central St. Elias orogen.

System	Sample	Elevation (m)	Bedrock Source	Individual age determinations (Ma)	Average age (Ma)	Standard deviation (Ma / %)
AHe	01CH29	1,082	Kulthieth FM	0.56, 0.61, 0.64, 0.71, 0.83, 0.84	0.7	±0.11 / 15.7%
AHe	01CH32	442	Kulthieth FM	0.55, 0.55, 0.57, 0.59, 0.66	0.58	±0.04 / 6.9%
AHe	01CH34	579	Poul Creek FM	1.37, 1.44, 1.19, 2.27, 2.70	1.79	±0.59 / 33%
AHe	01CH36	884	Kulthieth FM	0.82, 0.90, 0.93, 0.93, 0.95, 0.95	0.91	±0.04 / 4.4%
AHe	01CH37	221	Kulthieth FM	0.84, 0.98, 1.26, 2.37+	1.02	±0.17 / 16.7%
AHe	01CH38	640	Kulthieth FM	1.07, 1.27, 2.06	1.47	±0.43 / 29.3%
AHe	01CH41	274	Yakataga FM	1.28, 2.59, 2.00, 4.44+, 8.21+, 27.2+	1.96	±0.54 / 27.6%
AHe	01CH54	1,707	Yakataga FM	2.27, 2.69, 2.79, 3.70, 8.96+	2.86	±0.52 / 18.2%
AHe	02CH31	1,387	Kulthieth FM	0.67, 0.70, 0.71, 0.74	0.71	±0.03 / 3.5%
AHe	02CH33	2,432	Kulthieth FM	1.19, 1.19, 1.27, 1.40, 1.66	1.34	±0.18 / 13.4%
AHe	02CH34	1,798	Prince William Ter.	1.96	1.96	NA
AHe	05STP06	1,052	Prince William Ter.	0.70, 0.73, 0.86, 1.82+	0.76	±0.07 / 9.2%
AHe	05STP10	1,804	Chugach Ter.	20.5, 21.7, 22.1, 23.8, 25.7	22.8	±1.80 / 7.9%
AHe	05STP13	816	Kulthieth FM	0.59, 0.62, 0.67, 0.78, 0.82, 0.85	0.72	±0.10 / 13.9%
AHe	05STP18	1,250	Kulthieth FM	0.76, 0.81, 0.90, 0.94	0.85	±0.07 / 8.2%
AHe	05STP19	1,158	Prince William Ter.	0.78, 0.80, 0.82, 0.85	0.81	±0.03 / 3.7%
AHe	05STP23	1,432	Chugach Ter.	5.21, 5.42, 7.74, 7.86, 8.05	6.86	±1.26 / 18.4%
AHe	05STP36	2,171	Chugach Ter.	8.40, 8.65, 9.04, 9.17, 9.87, 14.7+	9.03	±0.50 / 5.5%
AHe	06STP21	1,678	Poul Creek FM	0.60, 0.64, 0.66, 0.82	0.68	±0.08 / 11.8%
AHe	06STP41	900	Chugach Ter.	15.6, 16.8, 18.4	16.9	±1.15 / 6.8%
AHe	06STP44	1,732	Chugach Ter.	19.5, 21.9	20.7	±1.20 / 5.8%
AHe	06STP46	2,428	Chugach Ter.	25.5, 26.1, 31.7	27.8	±2.79 / 10%
AHe	06STP72	0	Yakataga FM	2.13, 2.82, 3.99, 5.05+	2.98	±0.77 / 25.8%
AHe	06STP74	216	Yakataga FM	0.99, 1.02, 1.06, 1.07	1.04	±0.03 / 2.9%
AHe	06STP81	1,954	Poul Creek FM	0.99, 1.08, 1.33, 1.74, 3.75+	1.29	±0.29 / 22.5%
ZHe	05STP01	946	Kulthieth FM	12.09, 13.61	12.9	±1.1 / 8.5%
ZHe	05STP13	816	Kulthieth FM	8.61, 10.65	9.6	±1.4 / 14.6%
ZHe	05STP06	1,052	Prince William Ter.	4.38, 5.81	5.1	±1.0 / 19.6%
ZFT	05STP06	1,052	Prince William Ter.	42.7	42.7	±4.4 / 10.3%

Samples were analyzed at Virginia Tech *AHe), Lehigh University (ZHe), and Union College (ZFT); Ma = millions of years; Ter. = terrane; FM = formation; + = outlier not used in average age. The average AHe age reported for 01CH38 includes both old (Spotila et al., 2004) and new data. Additional sample data are presented in Tables 3.2 and 3.3.

APPENDIX A

Analytical methods

We obtained AHe ages on 25 bedrock samples of primarily sedimentary and metamorphic lithology at Virginia Tech (Table 3.2). AHe ages were measured on ~0.01-0.03 mg aliquots of 1-19 grains of apatite, which were typically $\geq 70 \mu\text{m}$ in diameter and were screened for micro-inclusions and crystal defects at 100x magnification. Although we analyzed the highest quality apatite grains available, poor apatite yields from some samples forced the use of lower-quality grains. To counter the potential effect of U- and Th-bearing micro-inclusions (i.e. zircon and monazite), fluid inclusions, or parent nuclide zonation on measured ages (Farley and Stockli, 2002), we analyzed multiple (~5) replicates per sample. Due to the young ages obtained in this study, the effect of radiation damage should not be a significant source of error (e.g. Herman et al., 2007; Flowers et al., 2007).

Samples were outgassed in Pt tubes in a resistance furnace at 940°C for 20 minutes and analyzed for ^4He by isotope dilution utilizing a ^3He spike and quadrupole mass spectrometry. Blank levels for ^4He detection using current procedures at Virginia Tech are ~0.2 femtomoles ^4He . Parent isotopes (^{238}U , ^{235}U , and ^{232}Th) were measured at Yale University and Caltech using isotope dilution (^{235}U and ^{230}Th spike) and ICP mass spectrometry. Although ^4He is also produced by ^{147}Sm decay, it is not routinely measured because it should produce <1% of radiogenic ^4He in typical apatite (Farley and Stockli, 2002). Cumulative analytical uncertainty, based on instrument precision and error in alpha particle ejection correction factor, is approximately $\pm 10\%$ (2σ). Age accuracy was

cross-checked by routine measurement of known standards including Durango fluorapatite (30.9 ± 1.53 Ma (1σ ; $n=40$)), with a known AHe age of 31.4 Ma (McDowell et al., 2005)). These measurements on Durango show that reproducibility on some natural samples is comparable to that expected from analytical errors. The error reported for each AHe age is the standard deviation of replicate samples (Table 3.2), which averaged about $\sim 10\%$ (1σ) and are thus comparable, but slightly higher than, analytical uncertainties.

New AHe data are generally consistent with previous work. For example, several new ages are almost identical to those determined from similar locations (02CH32, 01CH45, and 01CH39) by Spotila et al. (2004) (Figure 3.2). New analyses of five samples dated by Spotila et al. (2004) also closely match or provide improved constraints over earlier results. These samples were re-dated, because earlier work did not provide ample replicate analyses to establish reproducibility or was tainted by high uncertainties due to low ^4He content and poor sensitivity of earlier (now modified) analytical procedures. New analyses of 01CH38 yield the same result as obtained by Spotila et al. (2004) (Table 3.2). New ages for 02CH31 are slightly younger than previously reported (0.71 vs. 1.2 Ma; Table 3.1), but we use only the new data given improved analytical procedures and the low ^4He yield. Several other re-analyses modify earlier results. Spotila et al. (2004) interpreted anomalously old ages from 1-2 aliquots for 01CH34 and 01CH41 (Yakataga Formation) to be non-reset (i.e. AHe age > depositional age), but an additional 5-6 analyses indicates that these samples are partially reset. As with earlier data, new ages from these samples reproduce poorly, but the large number of replicates reveals a consistent age population younger than depositional age (Table 3.2). We speculate that

these samples were buried to just near closure depths, such that only apatite with lower temperature sensitivity (e.g. smaller grains) were reset, and accordingly use only the youngest ages (Figure 3.2). New data also indicate that the earlier single-aliquot age determination for 01CH29 of 3.9 Ma was erroneous (Spotila et al., 2004) (Table 3.2), presumably due to the presence of U or Th-bearing micro-inclusions.

Single grain ZHe ages were measured at Lehigh University on three samples. Euhedral grains ranging from 75-125 μm in diameter were screened at 100x magnification to avoid large inclusions or defects (Table 3.3). Samples were outgassed in a resistance furnace at 1350°C for 60 minutes and analyzed for ^4He by isotope dilution utilizing a ^3He spike and quadrupole mass spectrometry. Each sample was outgassed and analyzed a second time and the result was added to the initial measurement. Typically, less than 5% of residual ^4He was measured in these reheating steps. Parent isotopes were measured at Yale University using isotope dilution and ICP mass spectrometry. Analytical errors on individual isotope measurements are small ($\sim 1\text{-}2\%$), but intra-sample error is larger. The errors reported for each ZHe age is the standard deviation of replicate samples (Table 3.3).

ZFT ages were measured at Union College following procedures described by Garver and Kamp (2002) and Garver (2003). Polished zircon mounts were etched for 30 hours in a KOH:NaOH eutectic solution at 228 °C to reveal fossil tracks. Zircon mounts were then covered with a uranium-free muscovite external detector and irradiated with thermal neutrons (nominal flux 2×10^{15} n/cm²) utilizing the nuclear reactor at Oregon State University. The external detectors were etched in 48% HF at room temperature for

18 minutes to reveal induced tracks. Tracks were counted using an automated stage and Olympus BH2 microscope at 1250x magnification. Twelve standard mounts (Fish Canyon tuff, Buluk Member tuff, and Peach Spring Formation tuff) from two irradiations were analyzed to determine the ζ -calibration factor ($382.5 \pm 9.9 \text{ a cm}^2$). The ζ -factor and the track density of uranium glass (CN5) were used to calculate the ζ -age of the unknown samples using the ZETAAGE Program v. 4.8 of Mark T. Brandon (Brandon, 1992). The central fission track age was used, because the sample failed the X^2 -test (Table 3.3). This indicates the existence of a multiple age population, possibly because the sample is not depositional reset.

Acceleration in bedrock cooling rates

The acceleration in bedrock cooling on the windward flank of the St. Elias orogen may reflect accelerated erosion in the past 1-2 Ma due to climate change (Figure 3.6). Alternative explanations for the change in bedrock cooling rates are non-linear particle paths during exhumation or a change in tectonic influx. Cooling rates within the accreting Yakutat terrane could increase if rock trajectories steepen with respect to closure isotherms, as rock is horizontally translated through the fold and thrust belt. This is unlikely to play a major role in this circumstance, however, given that the same cooling trend is observed in the edge of the North America plate (Prince William Terrane) (Figure 3.6). Likewise, all samples in the fold and thrust belt increased in cooling rate between AFT and AHe closure (Figure 3.6), which cannot be explained by changes in trajectories predicted by numerical models of critical wedges. Models predict that the

transition from near-horizontal to steeply-inclined trajectories should occur near the deepest segment of the path, such that the corresponding change in cooling rate should vary from the foreland to the hinterland and occur between AFT and ZHe closure temperatures closest to the backstop (Konstantinovskaia and Malavieille, 2005; Naylor and Sinclair, 2007). More complex particle paths associated with thrust flats and ramps may have locally influenced individual samples, but seem unlikely to have increased cooling rates uniformly across the entire wedge. Furthermore, a comparable acceleration is observed elsewhere on the Alaska coastal margin (McAleer, 2006) and coincided with a ten-fold increase in terrigenous sediment flux into the Gulf of Alaska (Lagoe et al., 1993; Shackleton et al., 1995). Changes in tectonics, rather than independent changes in erosion, are more difficult to rule out as explanations for the increase in cooling rates. However, there is no independent evidence for a change in collision rate in the Pliocene (Plafker et al., 1994). Likewise, an increase in tectonic influx due to progressive recycling of orogenic detritus into the wedge would have produced a more gradual change in cooling rates than observed (Figure 3.6). We therefore interpret that the 11 fold acceleration in bedrock cooling rates was forced by an increase in erosivity due to climate change at 1-2 Ma.

Particle trajectories within the St. Elias orogen

Within the St. Elias orogen, due to the close spacing of the thrust faults, particle trajectories are not simply the result of ramp and flat geometries but are also influenced by motion on seaward forethrusts and underplating (Figures 3.1 and 3.10) (e.g. Naylor

and Sinclair, 2007; Konstantinovskaia and Malavieille, 2005). In a generalized model, as rock is horizontally translated through the orogenic wedge, initial particle trajectories with respect to the surface (exhumation) have a south-up vector which is largely controlled by the geometry of faults within the seaward deformation front. However, because these thrusts are not subaerial (only subject to erosion at glacial maxima), significant exhumation and therefore cooling is not taking place in this region. Progressing up the fold and thrust belt, as the forethrusts become subaerial particle trajectories with respect to the surface rotate to the north due to the steeper dip of the structurally higher forethrusts and because motion on seaward forethrust produces an additive north-up vector during exhumation. To the north, within the core of the fold and thrust belt, cumulative long-term particle trajectories become rotated past vertical (north up vector). In this region, duplexing at depth would also result in vertical particle trajectories during exhumation. Based on this model, and consistent with the distribution of reset AHe, AFT, and ZHe ages within the wedge (Figures 3.2. and 3.5), the deepest steepest trajectories are located near the Chugach St. Elias fault. In this region (Prince William terrane and the northern most Yakutat terrane), particle trajectories during exhumation are largely governed by the geometry of the Bagely backthrust at depth (Figure 3.10). In synthesis, time-averaged particle trajectories through the orogenic wedge become slightly inclined to the south at the seaward deformation front and subsequently rotated past vertical as particles are horizontally translated through the system, such that trajectories follow an arc-like path through time.

Additional references

- Brandon, M.T., 1992, Decomposition of fission-track grain-age distributions: *American Journal of Science*, v. 292, p. 535-564.
- Farley, K.A., and Stockli, D.F., 2002, (U-Th)/He dating of phosphates: apatite, monazite, and xenotime, in *Phosphates: Geochemical, Geobiological, and Materials Importance: Reviews in Mineralogy and Geochemistry*, v. 48, p.559-577.
- Garver, J.I., 2003, Etching zircon age standards for fission-track analysis, *Radiation Measurements*, v. 37, p. 47-53.
- Garver, J.I., and Kamp, P.J.J., 2002, Integration of zircon color and zircon fission-track zonation patterns in orogenic belts: application to the Southern Alps, New Zealand, *Tectonophysics*, v. 349, p. 203-219.
- McDowell, F.W., McIntosh, W.C., and Farley, K.A., 2005, A precise Ar/Ar reference age for the Durango apatite (U-Th)/He and fission-track dating standard: *Chemical Geology*, v. 214, p. 249-263.

Table 3.2: AHe data for the central St. Elias orogen

Sample	Elevation (m)	Latitude, longitude	Source and sample description	# grains	Mass (mg)	mwar (μm)	He (pmol)	U (ppm)	Th (ppm)	F_T	Corr. Age (Ma)	Closure temp. ($^{\circ}\text{C}$)	Average age (Ma) & standard dev.
01CH29-1	1,082	60.29255° -142.35583°	Kulthieth FM medium-grained arkosic quartzite	19	0.013	32.7	0.0014	36.6	74.3	0.62	0.56	76.2	0.7 $\pm 0.11 / 15.7\%$
				11	0.023	47.0	0.0019	26.5	33.8	0.75	0.61	81.3	
				10	0.027	57.4	0.0026	28.4	34.8	0.77	0.64	84.1	
				11	0.029	53.8	0.0048	43.3	28.4	0.75	0.84	80.9	
				4	0.025	67.7	0.0010	9.2	15.4	0.83	0.71	85.9	
				4	0.026	78.1	0.0012	9.6	12.1	0.83	0.83	87.0	
01CH32-1	442	60.34337° -142.4418°	Kulthieth FM coarse-grained arkose	13	0.0261	46.2	0.0035	42.3	45.1	0.72	0.66	80.4	0.58 $\pm 0.04 / 6.9\%$
				13	0.0233	49.2	0.0015	21.4	37.5	0.73	0.55	82.8	
				12	0.0189	40.6	0.0018	37.1	46.6	0.69	0.55	79.8	
				13	0.0247	46.1	0.0028	40.1	55.2	0.72	0.57	81.5	
				12	0.0214	45.7	0.0018	28.2	46.3	0.71	0.59	81.1	
01CH34-1	579	60.21338° -142.62697°	Poul Creek FM medium-grained poorly-sorted arkosic graywacke	5	0.028	68.4	0.0091	46.7	73.2	0.82	1.19	81.9	1.79 $\pm 0.59 / 33\%$
				15	0.033	50.3	0.0128	31.2	25.5	0.74	2.70	70.8	
				9	0.026	56.2	0.0097	53.6	54.3	0.77	1.37	77.7	
				1	0.016	96.6	0.0064	45.7	66.8	0.87	1.44	86.0	
				9	0.036	62.5	0.0121	30.3	26.2	0.79	2.27	75.4	
01CH36-1	884	60.33399° -142.60103°	Kulthieth FM medium-grained arkose	16	0.0375	52.3	0.0061	34.9	35.8	0.76	0.95	79.5	0.91 $\pm 0.04 / 4.4\%$
				14	0.0312	50.2	0.0040	27.9	32.1	0.75	0.93	79.0	
				11	0.0246	47.6	0.0021	16.6	30.5	0.74	0.90	78.4	
				10	0.0247	51.4	0.0019	16.3	29.6	0.76	0.82	80.4	
				11	0.0280	52.8	0.0047	37.2	35.9	0.75	0.93	79.8	
				10	0.0243	52.1	0.0049	43.5	38.6	0.77	0.95	79.4	
01CH37-1	221	60.3026° -142.781°	Kulthieth FM fine-grained arkose	19	0.0178	39.2	0.0023	29.1	29.5	0.71	0.98	74.7	1.02 $\pm 0.17 / 16.7\%$
				16	0.0157	37.9	0.0023	29.8	16.0	0.67	1.26	72.3	
				18	0.0204	39.7	0.0026	36.2	28.7	0.68	0.84	76.1	
				16	0.0185	39.1	0.0057	30.9	22.0	0.68	2.37++		
01CH38-1	640	60.31937° -143.11683°	Kulthieth FM fine-grained graywacke	15	0.0247	46.8	0.0086	36.9	29.5	0.73	2.06	71.7	1.47 $\pm 0.43 / 29.3\%$
				11	0.0255	50.2	0.0049	30.9	36.7	0.74	1.27	76.6	
				13	0.0267	50.5	0.0051	41.8	15.9	0.75	1.07	78.0	
01CH41-1	274	60.05915° -141.94°	~Yakataga FM fine-grained arkose	1	0.0032	55.2	0.0136	72.6	226.3	0.78	8.21++		1.96 $\pm 0.54 / 27.6\%$
				1	0.0032	59.8	0.0111	21.8	45.1	0.75	27.2++		
				1	0.0029	55.2	0.0011	61.4	61.9	0.77	1.28	78.0	
				15	0.0248	44.5	0.0077	23.9	34.4	0.72	2.59	69.3	
				16	0.0308	45.9	0.0122	42.5	39.0	0.73	2.00	71.7	
				14	0.0245	46.0	0.0193	35.1	46.7	0.73	4.44++		
01CH54-1	1,707	60.15477° -141.98813°	Yakataga FM coarse-grained poorly-sorted lithic arkose	10	0.0099	38.5	0.0067	65.4	22.6	0.66	2.79	66.5	2.86 $\pm 0.52 / 18.2\%$
				11	0.0099	36.2	0.0097	91.7	54.0	0.67	2.69	65.9	
				5	0.0137	59.0	0.0042	33.0	5.9	0.76	2.27	74.6	
				6	0.0176	53.8	0.0200	72.3	22.0	0.76	3.70	69.4	
				4	0.0172	61.0	0.0403	52.9	41.3	0.80	8.96++		
02CH31-1	1,387	60.28552° -141.45417°	Kulthieth FM medium-grained graywacke	11	0.0338	56.1	0.0037	30.5	32.1	0.76	0.71	82.9	0.71 $\pm 0.025 / 3.5\%$
				10	0.0285	55.3	0.0026	28.6	24.9	0.76	0.67	83.1	
				10	0.0280	51.9	0.0082	83.1	97.8	0.75	0.70	81.8	
				7	0.0255	55.4	0.0033	33.1	39.7	0.77	0.74	82.4	
02CH33-1	2,432	60.3095° -141.2241°	Kulthieth FM very coarse-grained lithic arkose	2	0.0261	91.2	0.0051	22.1	17.8	0.85	1.66	83.9	1.34 $\pm 0.18 / 13.4\%$
				15	0.0228	43.1	0.0031	25.2	26.1	0.69	1.19	74.7	
				14	0.0252	47.5	0.0044	30.4	34.5	0.73	1.19	76.2	
				15	0.0269	44.8	0.0046	25.3	35.3	0.69	1.40	74.0	
				15	0.0228	41.4	0.0032	24.3	26.6	0.69	1.27	73.6	
02CH34-1	1,798	60.41838° -141.76313°	Prince William Ter. fine-grained graywacke	14	0.0140	34.8	0.0209	16.7	22.5	0.66	1.96	67.7	1.96 NA
05STP6-1	1,052	60.4608° -143.05882°	Prince William Ter. medium-grained greenschist-grade meta graywacke	14	0.0327	53.7	0.0029	20.2	29.6	0.74	0.86	80.7	0.76 $\pm 0.07 / 9.2\%$
				14	0.0296	49.9	0.0028	25.9	36.3	0.73	0.73	80.8	
				14	0.0306	49.7	0.0041	37.3	51.7	0.73	0.70	81.1	
				12	0.0326	57.1	0.0044	13.8	18.8	0.76	1.82++		

Table 3.2: AHe data for the central St. Elias orogen continued.

Sample	Elevation (m)	Latitude, longitude	Source and sample description	# grains	Mass (mg)	mwar (μm)	He (pmol)	U (ppm)	Th (ppm)	F_T	Corr. Age (Ma)	Closure temp. ($^{\circ}\text{C}$)	Average age (Ma) & standard dev.
05STP10-1	1,804	60.8622°	Chugach Ter.	1	0.0107	92.0	0.0845	69.5	6.5	0.83	25.7	63.0	
-2		143.3235°	medium-grained	3	0.0378	94.8	0.0842	20.6	0.4	0.87	23.8	63.9	22.8
-3			amphibolite grade	5	0.0267	64.8	0.0661	28.3	0.4	0.81	20.5	59.6	$\pm 1.8 / 7.9\%$
-4			meta pelite / schist	4	0.0219	68.2	0.0434	21.2	1.4	0.81	21.7	59.9	
-5				8	0.0215	51.5	0.0595	31.8	1.5	0.75	22.1	55.8	
05STP13-1	816	60.4608°	Kulthieth FM	3	0.0258	73.9	0.0042	32.4	56.9	0.83	0.82	86.2	
-2		-143.05882°	medium-grained	1	0.0330	121.9	0.0039	24.5	21.7	0.90	0.85	94.2	
-3			arkose	13	0.0368	53.0	0.0072	44.2	82.2	0.75	0.78	81.2	0.72
-4				15	0.0339	47.9	0.0039	31.2	74.2	0.73	0.62	81.5	$\pm 0.10 / 13.9\%$
-5				14	0.0346	52.0	0.0047	31.6	83.9	0.75	0.67	82.2	
-6				5	0.0353	74.5	0.0031	15.3	81.2	0.83	0.59	89.0	
05STP18-1	1,250	60.40072°	Kulthieth FM	15	0.0360	51.4	0.0034	21.2	48.0	0.74	0.76	81.0	
-2		-142.51295°	coarse-grained	14	0.0354	55.8	0.0032	19.7	21.9	0.75	0.94	80.6	0.85
-3			finely laminated	15	0.0498	58.8	0.0042	20.6	25.1	0.76	0.81	82.6	$\pm 0.07 / 8.2\%$
-4			arkose	15	0.0520	58.4	0.0086	33.7	52.6	0.76	0.90	81.6	
05STP19-1	1,158	60.43331°	Prince William Ter.	13	0.0223	45.5	0.0022	25.0	34.1	0.71	0.80	78.6	
-2		-142.49036°	fine-grained	15	0.0205	45.2	0.0014	18.8	19.7	0.70	0.78	78.7	0.81
-3			greenschist grade	12	0.0142	40.5	0.0016	27.8	43.2	0.67	0.85	76.3	$\pm 0.03 / 3.7\%$
-4			meta graywacke	14	0.0249	51.7	0.0031	32.1	35.8	0.72	0.82	80.4	
05STP23-1	1,432	60.60122°	Chugach Ter.	12	0.0287	51.6	0.0269	26.1	17.2	0.76	7.86	63.2	
-2		-142.34093°	medium-grained	12	0.0162	42.7	0.0248	44.0	22.6	0.74	8.05	60.3	6.86
-3			muscovite schist	10	0.0255	53.4	0.0144	15.1	12.8	0.77	7.74	63.8	$\pm 1.26 / 18.4\%$
-4			with interbedded	11	0.0210	47.1	0.0070	13.6	7.4	0.77	5.42	64.6	
-5			meta sandstone	3	0.0273	88.3	0.0019	2.9	0.1	0.88	5.21	74.4	
05STP36-1	2,171	60.55415°	Chugach Ter.	16	0.0302	48.1	0.0306	29.3	2.2	0.72	9.04	61.6	
-2		-141.74559°	medium-grained	6	0.0300	65.6	0.0363	31.0	1.9	0.81	9.17	65.6	9.03
-3			amphibolite-grade	6	0.0437	75.5	0.0477	29.9	2.0	0.82	8.40	68.4	$\pm 0.50 / 5.5\%$
-4			biotite gneiss	9	0.0286	58.7	0.0191	18.9	1.3	0.77	8.65	64.4	
-5				6	0.0230	60.9	0.0393	41.3	2.8	0.79	9.87	64.0	
-6				11	0.0358	59.6	0.0499	22.6	1.9	0.79	14.68++		
06STP21-1	1,678	60.29503°	~Poul Creek FM	18	0.0334	44.7	0.0041	43.2	40.0	0.71	0.64	80.1	
-2		-141.96508°	medium-grained	19	0.0300	41.9	0.0052	49.2	35.6	0.70	0.82	77.1	0.68
-3			arkose	12	0.0275	48.4	0.0038	46.3	35.0	0.73	0.66	81.1	$\pm 0.08 / 11.8\%$
-4				5	0.0277	75.7	0.0061	72.9	55.3	0.82	0.60	89.2	
06STP41-1	900	60.74383°	Chugach Ter.	13	0.0139	43.0	0.0240	23.7	17.2	0.71	16.80	55.2	
-2		-141.96478°	very fine-grained	14	0.0145	40.1	0.0426	36.9	35.1	0.67	18.40	53.5	16.9
-3			mus. bio. Schist	9	0.0109	42.4	0.0176	23.9	20.0	0.69	15.60	55.5	$\pm 1.15 / 6.8\%$
06STP44-1	1,732	60.75363°	Chugach Ter.	7	0.0103	44.7	0.0242	20.6	36.5	0.70	21.90	53.8	
-2		-141.92648°	micaceous quartzite	8	0.0114	43.3	0.0331	31.1	40.3	0.70	19.50	54.2	20.7
													$\pm 1.2 / 5.8\%$
06STP46-1	2,428	60.7601°	Chugach Ter.	11	0.0116	39.0	0.0342	23.6	32.3	0.69	26.10	50.7	
-2		-141.88685°	very fine-grained	9	0.0101	39.5	0.0306	25.6	32.5	0.68	25.50	51.1	27.8
-3			mus. bio. schist	9	0.0089	38.3	0.0257	20.3	23.3	0.67	31.70	49.1	$\pm 2.79 / 10\%$
06STP72-1	0	60.06517°	Yakataga FM	1	0.0048	59.8	0.0022	45.9	27.7	0.80	2.13	75.2	
-2		-142.43135°	very poorly sorted	11	0.0236	48.0	0.0127	29.0	26.0	0.73	3.99	67.2	2.98
-3			diamictite / debris	10	0.0228	50.2	0.0252	90.5	38.1	0.75	2.82	70.4	$\pm 0.77 / 25.8\%$
-4			flow >5 cm clasts	1	0.0050	59.8	0.0038	25.1	45.3	0.80	5.05++		
06STP74-1	216	60.20113°	Yakataga FM	14	0.0293	48.3	0.0051	37.3	33.4	0.73	1.02	77.7	
-2		-142.82312°	medium-grained	14	0.0299	48.7	0.0060	40.1	40.3	0.72	1.07	77.4	1.04
-3			arkose	10	0.0200	48.1	0.0063	67.6	42.8	0.74	1.06	77.3	$\pm 0.03 / 2.9\%$
-4				8	0.0193	49.5	0.0045	50.2	41.7	0.74	0.99	78.3	
06STP81-1	1,954	60.214°	Poul Creek FM	17	0.0157	35.6	0.0062	99.5	46.6	0.64	1.08	72.5	
-2		-142.2416°	fine-grained	16	0.0151	36.0	0.0018	30.7	18.3	0.65	0.99	73.3	1.29
-3			graywacke	16	0.0150	37.2	0.0033	42.8	22.0	0.65	1.33	71.6	$\pm 0.29 / 22.5\%$
-4				11	0.0149	41.1	0.0114	49.9	29.3	0.69	3.75++		
-5				17	0.0144	35.9	0.0046	46.6	30.7	0.65	1.74	69.0	

Samples were analyzed at Virginia Tech; Ter. = terrane; bio. = biotite; mus. = muscovite; FM = formation; mwar = mass-weighted average radius; FT = alpha particle ejection correction factor; Corr. = corrected; temp. = temperature; dev = deviation; ++ = outlier not used in average age; Ma = millions of years. Errors for analyses are the average standard deviation of replicates. Latitude and longitude measured using North American Datum of 1927 Continental U.S. (NAD 27 CONUS). Accuracy of latitude and longitude

~10-100 m and elevation ~5-40 m. The average AHe age reported for 01CH38 includes both old (Spotila et al., 2004) and new data.

Table 3.3: ZHe and ZFT data for the central St. Elias orogen:

System	Sample	Elevation (m)	Latitude, longitude	# grains	235U				F _T	Age (Ma)	Average age (Ma) and standard dev.
					4He (mol)	238U (mol)	(mol)	232Th (mol)			
ZHe	05STP01-1	946	60.4208° -143.5028°	1	3.200E-13	2.039E-11	1.508E-13	7.357E-13	0.83	13.61	12.9
				1	2.112E-13	1.503E-11	1.112E-13	6.437E-12	0.82	12.09	±1.1 / 8.5%
ZHe	05STP06-1	1,052	60.4608° -143.05882°	1	7.268E-14	1.180E-11	8.729E-14	1.947E-12	0.79	5.81	5.1
				1	4.989E-14	1.178E-11	8.716E-14	2.263E-12	0.72	4.38	±1.0 / 19.6%
ZHe	05STP13-1	816	60.4608° -143.05882°	1	4.814E-13	4.343E-11	3.212E-13	5.261E-12	0.78	10.65	9.6
				1	1.539E-13	1.825E-11	1.350E-13	1.585E-12	0.74	8.61	±1.4 / 14.6%

System	Sample	# grains	ρ _s [cm ⁻²]	N _s	ρ _I (cm ⁻²)	N _I	ρ _D (cm ⁻²)	χ ²	U [ppm]	Age (Ma)	Error (1σ)
ZFT	06STP06	15	4.93E+6	520	3.08E+06	325	1.40E+05	1	266 ± 31	42.7	4.4

Samples were analyzed at Lehigh University (ZHe) and Union College (ZFT). Ma = millions of years. For ZHe data, FT = alpha particle ejection correction factor; dev. = deviation; Ages are FT corrected. Errors for analyses are the average standard deviation of replicates. For ZFT data, ρ_s = spontaneous track density; N_s = number of spontaneous tracks; ρ_I = induced track density; N_I = number of induced tracks; χ² = Chi-square probability; U = uranium concentration ± 2σ error; Zeta factor = 382.5±9.9 a cm²; CN5 standard glass. 06STP06 is from an arkose. The remaining rock types are in Table 3.2.

Chapter 4

Denudation and Deformation in a Glaciated Orogenic Wedge:

The St. Elias Orogen, Alaska

AARON L. BERGER and JAMES A. SPOTILA

Department of Geosciences, Virginia Tech, Blacksburg, Virginia 24061, USA

Submitted to *Geology*, 2008

ABSTRACT

Apatite (U-Th)/He dating from the St. Elias orogen illustrates a potential association between long-term denudation and glacier sliding. Cooling ages as young as 0.4 Ma (exhumation ~4-5 mm/yr) are concentrated in a narrow band near the glacier ELA (equilibrium line altitude) front, where mean Quaternary ELA intersects the windward flank of the orogen. This band of denudation is not correlated with individual faults, structural trends, or known concentrations of precipitation, and we propose that it is produced by focused glacier sliding at or near the ELA front. This implies that long-term glacial erosion is a maximum at ELA, which corroborates model predictions that glaciers and climate can control the pattern of crust removal from orogens. Denudation rates do not co-vary with fluctuations in glacier size along the ELA front, suggesting that small glaciers are capable of keeping pace with incision by larger ones and tectonic rock uplift. Ice discharge may thus play a critical, but complex, role in excavating glaciated orogens.

INTRODUCTION

Erosion has a fundamental influence on tectonics where mountain building is an integral consequence of relative plate motions. The distribution of strain and particle trajectories within orogenic belts can be strongly localized by focused erosion, to such a degree that erosion and deformation are coupled (*cf.* Willett, 2006). Since forms of erosion are climate-dependent, orogenic deformation is also partitioned by spatial climate gradients and modulated by temporal climate change (Willett, 1999; Whipple and Meade, 2004; Roe et al., 2006). Considerable attention has been devoted to the coupling of

erosion, tectonics, and climate in orogenic systems dominated by fluvial erosion (Willett, 1999; Thiede et al., 2004). Glacially-dominated mountain belts have been less studied in this context, despite the commonness of glaciers in orogenic belts and observations indicating that glacial erosion can be more effective than fluvial erosion (Hallet et al., 1996; Montgomery, 2002; Brocklehurst and Whipple, 2002). How glacial erosion influences orogeny has yet to be fully quantified.

Glacial erosion is known to affect both erosion rate and topography of mountain belts. The onset of late Cenozoic glaciation has been linked to increased denudation (Ehlers et al., 2006; Hebblen et al., 2007). Glacial erosion has also been shown to effectively modify preexisting fluvial landscapes (Harbor, 1992; Brocklehurst and Whipple, 2002; Montgomery, 2002; Oskin and Burbank, 2005). Yet how glacial erosion dictates patterns of crustal mass flux at the orogen scale is not known. Erosion by an individual glacier (i.e. a one-dimensional sense) is thought to scale with the basal velocity or unit flux per width of ice over rock (Hallet, 1979; Humphrey and Raymond, 1994), such that a glacier should focus denudation near its mean equilibrium line altitude (ELA), where cumulative ice discharge is a maximum (Andrews, 1972; Hallet, 1979; Anderson et al., 2006). Analytical models of orogenic wedges incorporating a glacier erosion rule predict that long-term rock uplift should peak at and just below ELA and that onset of glacial erosion should increase erosivity and shrink the wedge (Tomkin and Roe, 2007; Whipple and Meade, 2004). Yet a spatial relationship between maximum, long-term (10^6 yr) denudation and mean ELA has not been identified in the field (Hallet, 1979; Staiger et al., 2005; Oskin and Burbank, 2005).

To quantify the effect of glacial erosion in an active orogen, we have applied low temperature thermochronometry to the rugged St. Elias orogen in southern Alaska (Figure 4.1). This orogen has been constructed by collision of the Yakutat microplate at the syntaxial bend in the Pacific-North America plate boundary since the Middle Miocene (Plafker et al., 1994; Bruhn et al., 2004). At present, ~2-3 cm/yr shortening is accommodated in a fold and thrust belt along the leading edge of the Yakutat plate (Bruhn et al., 2004). For the past 5 Ma, this collision has been glaciated (Lagoe et al., 1993), owing to high latitude and intense coastal precipitation (Péwé, 1975). Glacier ELA rises steadily from the coast and intersects both flanks of the orogen, but fluctuates with climate cycles (Meigs and Sauber, 2000). Presently about half of the orogen is covered by temperate glaciers (Figure 4.1), and glacier coverage was nearly complete during previous glacial maxima (Péwé, 1975). Earlier work has shown that exhumation is more rapid on the windward flank of the orogen and that an intensification of glaciation in the Pliocene accelerated denudation (Spotila et al., 2004; Berger et al., in press), but has yet to establish a spatial relationship between denudation and ELA.

METHODS

We have combined 19 new (U-Th)/He apatite ages (AHe) from bedrock samples with 35 previously-obtained AHe ages from the St. Elias orogen (Spotila et al., 2004; Berger et al., in press). This thermochronometer is sensitive to rock cooling from ~40-90 °C, with a closure temperature of ~70 °C for typical sample grain size and cooling history

(Ehlers and Farley, 2003). Analytical techniques, explanation of uncertainties, and data are provided in Appendix B and Table 4.1.

Although other thermochronometers have been applied to this orogen (Berger et al., in press), we focus here on AHe data to discern spatial patterns in low-temperature cooling from a limited closure temperature range, rather than on the cooling history based on multiple mineral systems. AHe ages likely represent exhumation from ~1.5-2 km depth, given conditions in the orogenic wedge (Appendix B). Because we are concerned with first-order variations in cooling, we do not address in detail the complications of topography and advection on cooling ages or exhumation rates. Variations in geothermal conditions should be out-weighed by the differences in cooling ages that we observe. Samples were also generally collected from similar topographic positions on ridges of similar relief (~1-2 km), in an attempt to minimize the effects of variation in closure depth due to current topography (Appendix B).

RESULTS

New AHe ages define a general pattern that is consistent with previous observations (Figure 4.1; Table 4.1). AHe ages are older (~10-20 Ma, cooling rates ~3-10 °C/Ma) along the leeward (northern) flank of the range, but decrease by ~50-fold over ~60 km toward the coast. Older ages imply slower exhumation of the Chugach terrane on the leeward flank, which represents the deformational backstop of a doubly-vergent wedge (Berger et al., in press). Younger ages on the windward flank imply faster exhumation of the Prince William and Yakutat terranes, where precipitation and

deformation are concentrated. New AHe ages from this flank are locally even younger than previously measured (Spotila et al., 2004). AHe ages as young as 0.4 Ma define pockets of extremely rapid cooling (~ 200 °C/Ma) that were not previously sampled.

These young AHe ages suggest rapid exhumation rates. We estimate peak exhumation rates from the youngest ages of up to 4-5 mm/yr, based on calculated closure temperatures and an elevated geothermal gradient that takes into account heat advection using a 1-dimensional thermokinematic model (Appendix B). This predicted geothermal gradient is nearly double the regional background gradient (Appendix B). The resulting peak exhumation rate is consistent with a poorly defined age-elevation gradient from a short vertical transect (Figure 4.4). Although other variations in isotherm geometry associated with present and paleo-topography could result in local cooling age trends that do not correspond to exhumation, they are unlikely to explain the first-order AHe pattern. To produce the youngest ages without a local increase in exhumation rate, the geothermal gradient would locally need to be an improbable six times greater than the background gradient. Because of this unlikelihood, we interpret the pattern of AHe ages to reflect a localization of exhumation near the coast.

The AHe age pattern suggests a spatial relationship between exhumation and glacier ELA on the windward flank of the orogen. The youngest ages (< 1.0 Ma), and presumably focused exhumation, are concentrated in a narrow belt that is parallel to and ~ 35 km north of the coast (Figure 4.1). Ages just to the north and south of this belt are older (~ 2 Ma). This zone of rapid cooling roughly corresponds to what we term the “ELA front.” This is the position where mean Quaternary glacier ELA intersects the landscape

on the windward face of the orogen, and represents where time-averaged, unit ice discharge within individual glaciers should be a maximum. The upper limit of the ELA front is defined by modern ELA (Figures 4.1 4.5), whereas the lower extent is estimated to be ~300 m lower based on the position of glaciers on the continental shelf during last glacial maximum (Péwé, 1975; Mayo, 1986) (Appendix B). The ELA front and the band of young ages closely overlap in the western half of the orogen (Figure 4.1), as illustrated on a north-south plot (Figure 4.2a). To the east, the belt of young ages is offset ~20 km north of the ELA front, although it is poorly constrained due to limited number of well constrained ages. The age-ELA relationship is thus tenuous. However, there is an overall correlation ($R^2=0.70$) between AHe age and distance from the center of the ELA front (Figure 4.2b), even ignoring differences in sample elevation and geothermal gradient. This trend is best defined by ages from the leeward flank that increase northwards, whereas ages from the south are all <2 Ma and cluster at the base of the plot.

It is possible that the belt of young AHe ages is related to other variables or does not reflect rock uplift. The windward flank of the orogen receives heavy orographic precipitation, which could drive localized rapid erosion. Although precipitation is poorly constrained in this region and may have varied throughout the Quaternary (Appendix B), the band of young ages does not correlate with a known concentration in modern precipitation. High annual precipitation continues ~40 km inland of the young AHe ages (Figure 4.2a). Rapid exhumation could also be driven by a concentration of deformation in the orogenic wedge, independent of any climatic gradients. All ages younger than 2 Ma occur south of a proposed backthrust beneath the Bagley ice field (Berger et al., in

press). However, the belt of the youngest (<1 Ma) ages does not correlate with a specific thrust fault and is at an oblique angle to the structural trend defined by an echelon hinterland thrusts (Figure 4.1). Another alternative explanation is that young ages represent exhumation without rock uplift. For example, a hypothetical topographic high could have been situated over what is now the ELA front and removed by erosion since ~1 Ma. Given the lack of supporting evidence for these alternatives, however, we focus interpretations on the tenuous relationship of exhumation and presumably rock uplift with the ELA front.

DISCUSSION

We propose that the belt of young AHe ages reflects long-term denudation that is concentrated at the loci of maximum glacier sliding on the windward flank of the orogen. This hypothesis is consistent with a simplistic view based on theoretical predictions, 1-d numerical simulations, and short-term observations, that erosion along individual glaciers should scale with the flux of ice over rock (Hallet, 1979; Humphrey and Raymond, 1994; Anderson et al., 2006). That such a phenomenon may actually be observed at the orogen scale, however, is surprising.

If it is true that glacial erosion scales simply with ice discharge, then the most rapid denudation should not be uniformly focused along the zone of mean ELA defined by multiple glaciers. The fastest erosion along an individual glacier should occur near ELA (Andrews, 1972; Hallet, 1979), but the fastest regional denudation should occur along large glaciers with high ice discharge. Because ice discharge is distributed along

the length of a glacier as a broad curve, rather than a sharp peak centered at ELA (Anderson et al., 2006), ice discharge and erosion nearly anywhere along large outlet glaciers (e.g. Bering glacier) should exceed that at ELA on smaller glaciers that are not fed from the orogen interior (e.g. Hayden glacier) (Figures 4.1 and 4.5). Yet exhumation rates at modern ELAs are consistently rapid and do not correlate with current glacier drainage areas, which vary by two orders of magnitude (Figure 4.3). Drainage area should be a loose proxy for relative differences in modern ice discharge, given that precipitation does not vary by more than a factor of two over these basins (Appendix B). Quaternary ice discharge may have been comparably heterogeneous, given the improbability of lateral glacier migration (Harbor, 1992) and a prominent east-west divide (Waxell-St. Elias ridge) that should have kept discharge concentrated at outlet glaciers (Figure 4.1; Appendix B). Yet the pattern of denudation does not reflect these probable along-strike variations in ice discharge.

The AHe age-ELA association is also surprising considering the numerous factors that could obscure it. AHe ages represent exhumation averaged over longer time scales than potential shifts in mean ELA. Local surface uplift could shift mean ELA southwards by 10s of km in less than 100 Ka, given high rates of uplift and the orogen's seaward taper (Figure 4.2a). For example, uplift along the Icy Bay fault could have built the plateau beneath the Guyot glacier, thereby pushing the ELA front away from the belt of young ages (Figure 4.1). Local uplift associated with specific faults and local concentrations of precipitation could also perturb a general relationship between denudation and glacier sliding. Given that ELA is itself linked to precipitation and that

concentrations of erosion likely require fault motion to replace denuded crust, we would expect precipitation and structure to relate to long-term denudation to at least some degree.

To reconcile these complications, we propose a more complex conceptual model of orogen-scale glacial erosion. The lack of correlation between denudation and glacier drainage area suggests that the erosional power of all glaciers along the ELA front is sufficient to keep pace with tectonic rock uplift. Ubiquitous high annual precipitation may enable even small glaciers to erode quickly. Erosion by small glaciers and mass wasting may also be coupled to incision by large glaciers, analogous to how fluvial tributaries respond to base level. Alternatively, large glaciers may have reached a process threshold (e.g. over-deepening) and are thus “graded” (Alley et al., 2003). Given the broad distribution of ice discharge along a glacier (Anderson et al., 2006), we also suggest that the most rapid erosion occurs where high ice flux intersects an orogen’s structural-topographic front. For example, the ELA front near the Malaspina glacier occurs along the coastal plain south of the active thrust front, where there is likely no rock uplift. Hence, the zone of rapid denudation occurs north of the ELA front, where the ice flux is presumably still very high. Finally, local variations in precipitation, uplift, topographic and ELA history, and other factors may modify the denudation pattern or obscure the relationship between time-averaged exhumation and ELA. Altogether, this conceptual model predicts that denudation relates to glacier sliding, but acknowledges innate complexity in glacial and orogenic systems.

These interpretations build on a model of glacial erosion, in which glaciers act as “buzz saws” that limit mean orogenic topography below mean Quaternary ELA (Brozovic et al., 1997; Mitchell and Montgomery, 2006). Our observations illustrate a denudational buzz saw, or glacial excavator, that focuses exhumation near the narrow ELA front. Topography may locally rise above ELA (e.g. Waxell-St. Elias ridge), but glaciers play the more significant geodynamic role of controlling the removal of crust from the orogen. This fits with theoretical models of orogenic wedges, in which glaciers focus denudation and partition deformation (Tomkin and Roe, 2007). It is also distinct from fluviially-dominated orogens, where denudation is more generally influenced by the patterns of precipitation and stream power (Willett, 1999; Thiede et al., 2004; Whipple and Meade, 2004; Roe et al, 2006). In glacially-dominated orogens, precipitation does not necessarily produce rapid erosion where it falls, but instead causes erosion down-gradient at the ELA front, as dictated by complex interactions between precipitation, temperature, ice flux, topography, and tectonics.

CONCLUSIONS

These data quantify an important aspect of how glaciers affect denudation in active orogenic belts. Long-term denudation appears to be concentrated near the loci of maximum individual glacier sliding along mean Quaternary ELA on the windward flank of the orogen. This pattern may be locally perturbed by active structures, topography, or precipitation, but does not seem to be influenced by the relative sizes or discharges of glaciers along the ELA front. This suggests complexity in the behavior of long-term

glacial denudation. The localization of denudation near ELA matches model predictions for how exhumation and deformation should be focused and implies an important climatic control on orogenic behavior. These findings may be tested by measuring patterns of erosion rate over shorter timescales (e.g. cosmogenic radionuclide dating) or similar investigations of other glaciated orogens, in which late Cenozoic climate change could have resulted in belts of focused denudation near the position of mean ELA.


ACKNOWLEDGEMENTS

We thank collaborators for helpful discussions, including B. Hallet, J. Buscher, R. McAleer, T. Pavlis, J. Chapman, E. Enkelmann, A. Meigs, R. Bruhn, S. Gulick, P. Koons, J. Elliott, J. Freymueller, and all other STEEP participants. We thank D. Bubank, P. Reiners, J. Tomkin, S. Willett, and editor A. Barth for helpful reviews that strengthened this paper. Support was provided by National Science Foundation grant EAR0409224.

REFERENCES

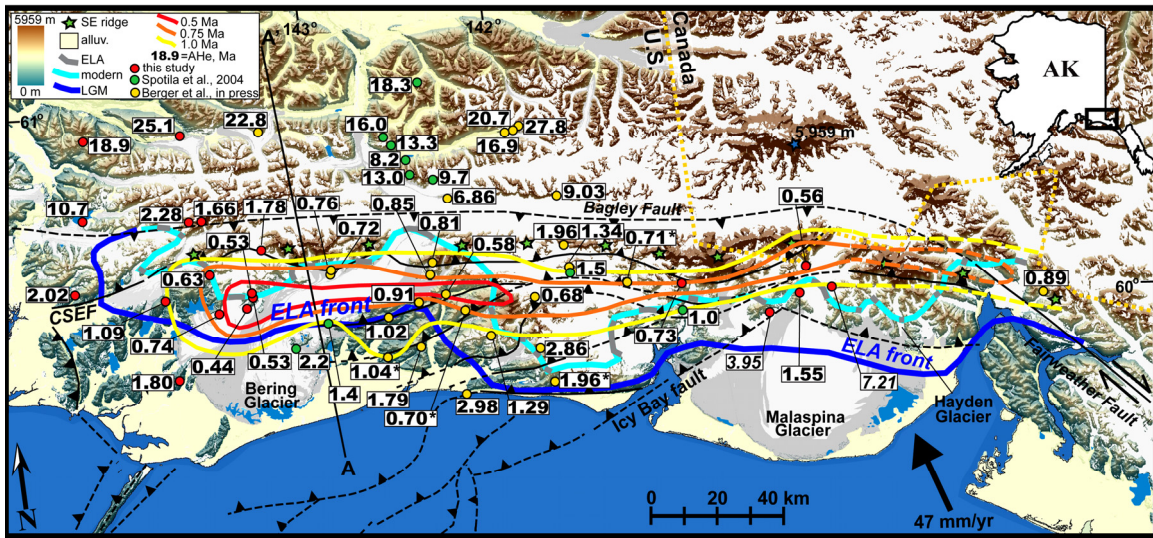
- Alley, R.B., Lawson, D.E., Larson, G.J., Evenson, E.B., and Baker, G.S., 2003, Stabilizing feedbacks in glacier-bed erosion, *Nature*, 424, 758-760.
- Anderson, R.S., Molnar, P., and Kessler, M.A., 2006, Features of glacial valley profiles simply explained, *J. Geophys. Res.*, 111, F01004, 14 p.
- Andrews, J.T., 1972, Glacier power, mass balances, velocities, and erosion potential, *Z. Geomorphol. N.F. Suppl. Bd.*, 13, 1-17.
- Berger, A.L., Spotila, J.A., Chapman, J., Pavlis, T., Enkelmann, E., Ruppert, N., and Buscher, J., in press, Architecture, kinematics, and exhumation, across the central St. Elias Orogen; A thermochronologic approach, *Earth. and Planet. Sci. Lett.*
- Brocklehurst, S.H., and Whipple, K.X., 2002, Glacial erosion and relief production in the eastern Sierra Nevada, California, *Geomorphology*, 42, 1-24.
- Brozovic, N., Burbank, D.W., and Meigs, A.J., 1997, Climatic limits on landscape development in the Northwestern Himalaya, *Science*, 276, 571-574.
- Bruhn, R.L., Pavlis, T.L., Plafker, G., and Serpa, L., 2004, Deformation during terrane accretion in the Saint Elias Orogen, Alaska, *Geol. Soc. Amer. Bull.*, 116, 771-787.
- Ehlers, T.A., Farley, K.A., Rusmore, M.E., and Woodsworth, G.J., 2006, Apatite (U-Th)/He signal of large magnitude accelerated glacial erosion, southwest British Columbia, *Geology*, 34, 765-768.

- Ehlers, T., and Farley, K., 2003, Apatite (U-Th)/He thermochronometry: methods and applications to problems in tectonics and surface processes, *Earth and Planetary Science Letters*, 206, 1-14.
- Hallet, B., 1979, A theoretical model of glacial abrasion, *J. Glaciology*, 23, 39-50.
- Hallet, B., Hunter, L., and Bogen, J., 1996, Rates of erosion and sediment evacuation by glaciers: A review of field data and their implications, *Global and Planetary Change*, 12, 213-235.
- Harbor, J.M., 1992, Numerical modeling of the development of U-shaped valleys by glacial erosion, *Geol. Soc. Amer. Bull.*, 104, 1364-1375.
- Hebbeln, D., Lamy, F., Mohtadi, M., and Echtler, H., 2007, Tracing the impact of glacial-interglacial climate variability on erosion of the southern Andes, *Geology*, 35, 131-134.
- Humphrey, N.F., and Raymond, C.F., 1994, Hydrology, erosion, and sediment production in a surging glacier: Variegated Glacier, Alaska, 1982-83, *J. Glaciology*, 40, 539-552.
- Lagoe, M.B., Eyles, C.H., Eyles, N., and Hale, C., 1993, Timing of late Cenozoic tidewater glaciation in the far North Pacific, *Geology. Soc. Amer. Bull.*, 105, 1542-1560.
- Mayo, L.R., 1986, Annual runoff rate from glaciers in Alaska: A model using the altitude of glacier mass balance equilibrium, in D.L. Kane (ed.), *Cold Regions Hydrology Symposium*, Amer. Water Res. Assoc., Bethesda, Maryland, 509-517.

- Meigs, A., and Sauber, J., 2000, Southern Alaska as an example of the long-term consequences of mountain building under the influence of glaciers, *Quat. Sci. Reviews*, 19, 1543-1562.
- Mitchell, S.G., Montgomery, D.R., 2006, Influence of a glacial buzzsaw on the height and morphology of the Cascade Range in central Washington State, USA, *Quat. Research*, 65, 96-107.
- Montgomery, D.R., 2002, Valley formation by fluvial and glacial erosion, 30, 1047-1050.
- Oskin, M., and Burbank, D.W., 2005, Alpine landscape evolution dominated by cirque retreat, *Geology*, 33, 933-936.
- Péwé, T.L., 1975, Quaternary geology of Alaska, U.S. Geol. Surv. Professional Paper, 835, 139 p.
- Plafker, G., Moore, J.C., and Winkler, G.R., 1994, Geology of the Southern Alaska margin, *The Geology of North America*, Geol. Soc. Amer., Vol. G-1, 389-447.
- Roe, G.H., Stolar, D.B., and Willett, S.D., 2006, Response of a steady-state critical wedge orogen to changes in climate and tectonic forcing, in Willett, S.D., Hovius, N., Brandon, M.T., and Fisher, D.M., eds., *Tectonics, Climate, and Landscape Evolution: Geol. Soc. Amer. Special Paper 398, Penrose Conference Series*, 227-239.
- Spatial Climate Analysis Center, 2002, PRISM 1961-1990 Mean Annual Precipitation: Alaska, Oregon Climate Service, Oregon State University, via  The Climate Source, http://www.cimatesouce.com/ak/fact_sheets/akppt_xl.jpg.

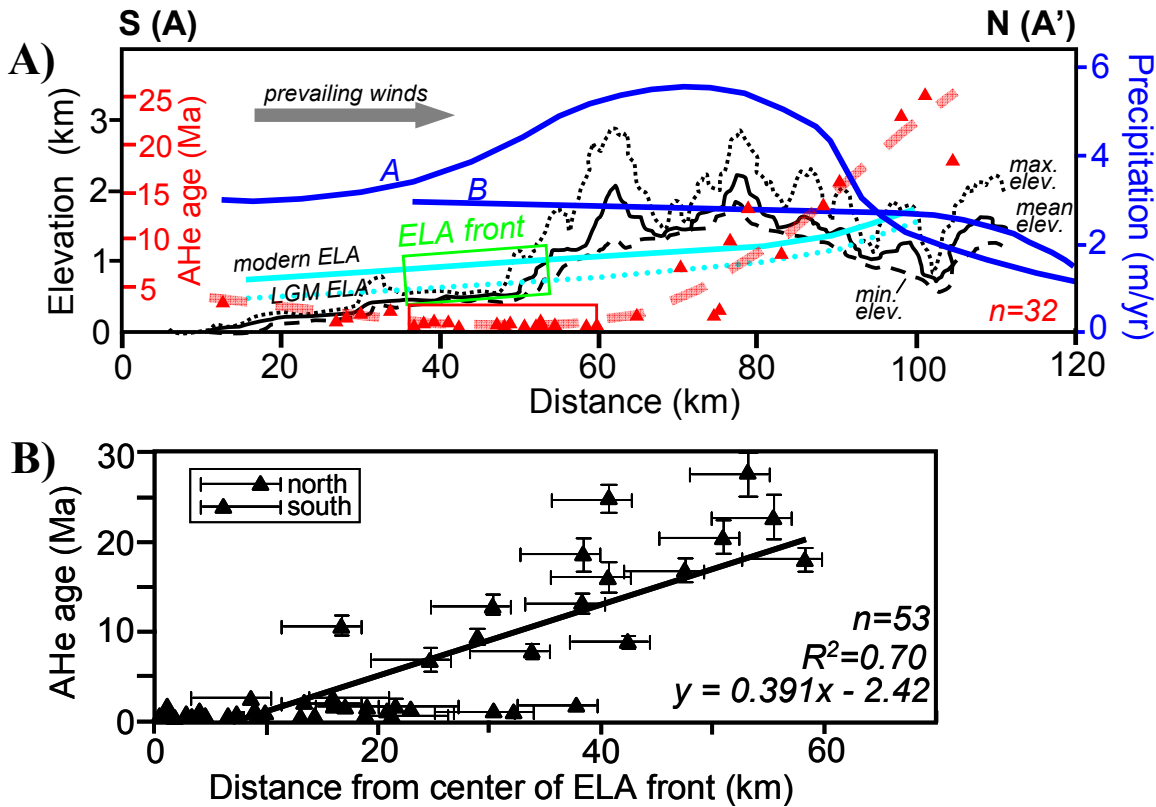
- Spotila, J.A., Buscher, J., Meigs, A., and Reiners, P., 2004, Long-term glacial erosion of active mountain belts: Example of the Chugach-St. Elias Range, Alaska, *Geology*, 32, 501-504.
- Staiger, J.K.W., Gosse, J.C., Johnson, J.V., Fastook, J., Gray, J.T., Stockli, D.F., Stockli, L., and Finkel, R., 2005, Quaternary relief generation by polythermal glacier ice, *Earth Surface Processes and Landforms*, 30, 1145-1159.
- Thiede, R.C., Bookhagen, B., Arrowsmith, J.R., Sobel, E.R., Strecker, M.R., 2004, Climatic control on rapid exhumation along the southern Himalayan front, *Earth and Planetary Sci. Lett.*, 222, 791-806.
- Tomkin, J.H., and Roe, G.H., 2007, Climate and tectonic controls on glaciated critical-taper orogens, *Earth and Planet. Sci. Lett.*, 262, 385-397.
- Whipple, K.X., and Meade, B.J., 2004, Controls on the strength of coupling among climatic, erosion, and deformation in two-sided, frictional orogenic wedges at steady state, *J. Geophys. Res.*, 109, F01011, 24 p.
- Willett, S.D., 2006, Introduction, in S.D. Willett, N. Hovius, M.T. Brandon, and D.M. Fisher, *Tectonics, Climate, and Landscape Evolution*, *Geol. Soc. Amer. Special Paper* 398, vii-xi.
- Willett, S.D., 1999, Orogeny and orography: The effects of erosion on the structure of mountain belts, *J. Geophys. Res.*, 104, 28,957-28,981.

Figure 4.1: Distribution of AHe ages in the St. Elias orogen.



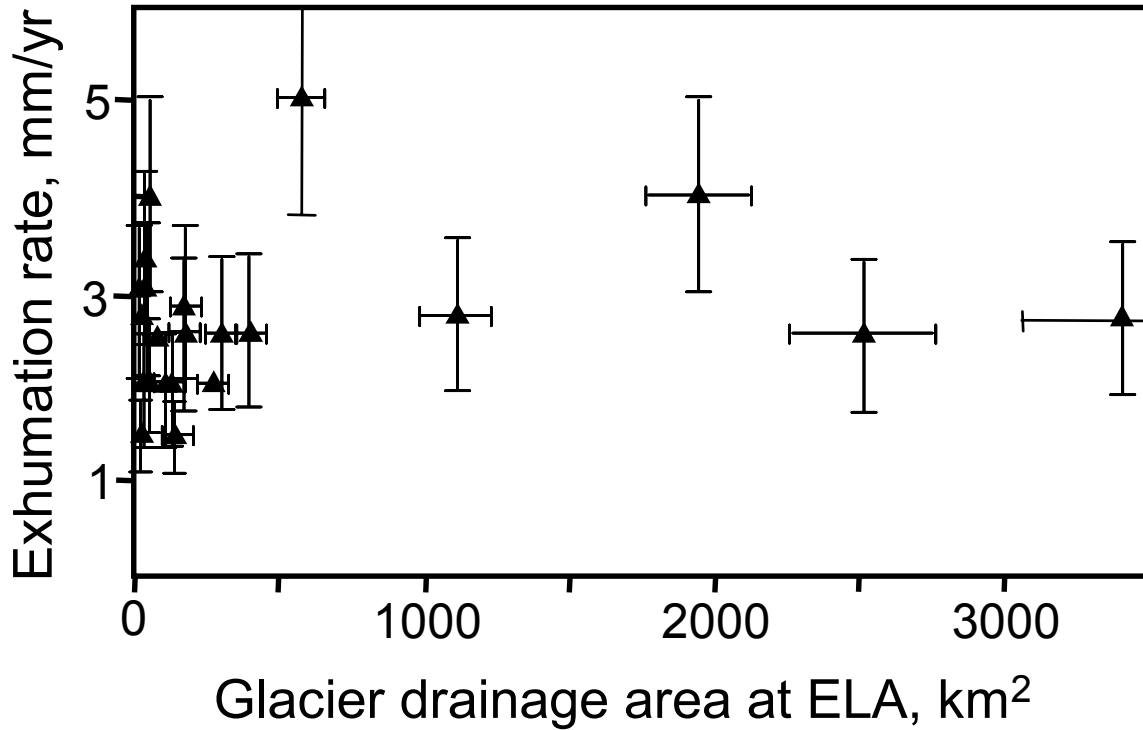
Shaded relief map of the St. Elias orogen, showing structures and apatite (U-Th)/He ages (Table 4.1). The youngest AHe ages are contoured and occur near glacier ELA on the windward flank. Contours of 0.5, 0.75, and 1.0 Ma should approximate exhumation rates of 4.0, 2.7, and 2.0 mm/yr (Appendix B). Distribution of glaciers is based on combination of USGS 1:250,000 maps and high-altitude, non-alluvial surfaces with slopes $<10^\circ$. Modern ELAs for southward-flowing glaciers are shown as thick blue lines (Appendix B). ELA during the last glacial maximum (LGM) is assumed to be ~ 300 m lower (P  w  , 1975) and approximated as the dark blue line. The “ELA front” is the zone between modern and glacial maxima ELA on the windward flank. Green stars mark the location of Waxell-St. Elias (SE) ridge (Figure 4.6). Relative motion of the Yakutat terrane with respect to North America is shown at bottom right (Plafker et al., 1994).

Figure 4.2: Precipitation, topography, ELA, and AHe age distribution



A) Relationship between topography, ELA, precipitation, and AHe age along a north-south profile (AA', Figure 4.1). Topography (max., min., and mean elevation) is from a 10-km-wide swath and 60-m-resolution DEMs. Modern ELA is based on Mayo (1986). ELA during the last glacial maximum (LGM) is ~300 m lower near the coast and ~200 m lower farther inland after Péwé (1975). The green box shows the “ELA front”, where mean Quaternary ELA (i.e. zone between modern and LGM ELA) intersects mean topography of the windward flank. The two curves of mean annual precipitation are from (A) a model that integrates regional data with an orographic function (Spatial Climate Analysis Center, 2002) and (B) synthesis of regional data (Péwé, 1975) (Appendix B). AHe ages (red triangles) for samples within 50 km of AA' were projected orthogonally. The dashed pink line approximates the trend of AHe ages, and the red box highlights the youngest ages. B) AHe age versus minimum sample distance from the center line of the ELA front for all reset samples (excludes those in italics on Figure 4.1; Appendix B). Error bars for AHe age are 1σ . Error bars for distance are ± 5 km for southern ELA (glacial maxima) and ± 2 km for modern ELA (Appendix B), the skewness of which defines whether the AHe ages are from north or south of the ELA front.

Figure 4.3: Exhumation rate versus glacier-basin



Long-term exhumation rate versus drainage-basin area at modern ELA of southward-flowing glaciers (Figure 4.5; Table 4.2). If drainage area is a proxy for ice discharge, then long-term denudation is unaffected by along-strike variation in ice flux. Error bars are estimated to be $\pm 10\%$ for drainage area and $\pm 25\%$ for exhumation rate.

APPENDIX B

Thermochronologic methods

Low-temperature thermochronometry was used to constrain the exhumation pattern across the St. Elias orogen. New (U-Th)/He ages of apatite (AHe) were obtained from bedrock samples collected by helicopter along the east-west ELA front along the windward flank of the orogen. Samples used consisted mainly of sedimentary (arkose, graywacke) and metamorphic (gneiss) lithologies. New ages were combined with previous AHe ages from Spotila et al. (2004) and Berger et al (in press). (U-Th)/He is based on the radiogenic production and thermally-controlled diffusion of ^4He within host minerals. Apparent AHe cooling ages typically correspond to closure temperatures of ~ 70 °C, but closure temperature is cooling-rate and grain-size dependent (Wolf et al., 1996; Farley, 2000; Ehlers and Farley, 2003).

AHe ages were measured at Virginia Tech on 1-25 grain, ~ 0.01 - 0.03 mg aliquots (Table 4.1). Apatite grains dated were ≥ 70 μm in diameter and were screened for microinclusions and other crystal defects at 100x magnification. Although the highest quality apatite grains available were used, apatite yields from some samples were poor, forcing the use of lower-quality grains. To counter the potential effect of U- and Th-bearing microinclusions (i.e. zircon and monazite (House et al., 1997)), fluid inclusions, or parent nuclide zonation on measured ages (Fitzgerald et al., 2006), we analyzed multiple (~ 5) replicates per sample (a total of 97 analyses for 19 samples). This enabled evaluation of sample reproducibility and identification of anomalously old outliers that likely have ^4He contamination. Samples were outgassed in Pt tubes in a resistance

furnace at 940 °C for 20 minutes (followed by a 20-minute reextraction test) and analyzed for ^4He by isotope dilution utilizing a ^3He spike and quadrupole mass spectrometry. Blank levels for ^4He detection using current procedures at Virginia Tech are ~ 0.2 femtomoles. Radiogenic parent isotopes (^{238}U , ^{235}U , and ^{232}Th) were measured at Yale University and Caltech using isotope dilution (^{235}U and ^{230}Th spike) and ICP mass spectrometry. Although ^4He is also produced by ^{147}Sm decay, it was not routinely measured because it should produce $<1\%$ of radiogenic ^4He in typical apatite and should only be a factor in AHe ages when U concentrations are <5 ppm (which applies to none of our samples; Table 4.1) (Farley and Stockli, 2002; Reiners and Nicolescu, in press).

Routine 1σ uncertainties due to instrument precision are $\pm 1\text{-}2\%$ for U and Th content, $\pm 2\text{-}3\%$ for He content, and $\pm 4\text{-}5\%$ for alpha ejection correction factor based on grain dimension and shape. Cumulative analytical uncertainty is thus approximately $\pm 10\%$ (2σ). Age accuracy was cross-checked by measurements of known standards, such as Durango fluorapatite (30.9 ± 1.53 Ma (1σ ; $n=40$)), with a known age of 31.4 Ma (McDowell et al., 2005)). These measurements on Durango show that reproducibility on some natural samples is comparable to that expected from analytical errors.

Uncertainties for samples are reported as the observed standard deviation from the mean of individual age determinations (Table 4.1). The average AHe reproducibility on well-reproduced average ages is $\sim 11\%$ (1σ ; 16 samples, 74 age determinations), which is worse than that obtained from Durango apatite. Some samples with very young average AHe ages reproduced well, such as 05STP2 (0.44 Ma $\pm 6.9\%$ 1σ , $n=5$) and 05STP4 (0.74 Ma $\pm 9.7\%$ 1σ , $n=6$). Other samples reproduced more poorly. The 11% average

reproducibility excludes three samples (05STP11, 06STP1, 06STP71) that reproduced poorly ($1\sigma > 20\%$). Two of these samples are from thin Cenozoic stratigraphy on the eastern end of the orogen and may be only partially reset (see below). The 11% average reproducibility also ignores ten individual age determinations that were considered outliers and culled prior to calculation of average age, because they were significantly older than concordant replicates and were likely contaminated by excess ^4He due to inclusions (Table 4.1).

The pattern of new ages measured here are consistent with previous AHe dating in the orogen (Spotila et al., 2004; Berger et al., in rev.) (Figure 4.1). One sample dated here was also dated previously by Spotila et al. (2004), but with a discrepant result. Sample 02CH28 was reported as average AHe of 4.8 Ma by Spotila et al. (2004), but was redated here as 0.73 Ma (Table 4.1). One of four new age determinations was anomalously old (Table 4.1), suggesting this sample is prone to ^4He contamination by micro-inclusions. Although there is no independent indication that the earlier analyses were inaccurate due to poor apatite quality, we choose to use the younger age population (i.e. the new data) for our interpretations here (Figure 4.1).

AHe ages constrain the pattern of low-temperature cooling throughout most of the orogen (Figure 4.1). However, many of the samples that reproduced poorly are from the eastern part of the orogen, near the bend in the plate boundary at the Fairweather fault and the Seward and Hubbard outlet glaciers. One sample from near the Hubbard glacier is very young (06STP4, 0.56 Ma), but other samples from this region do not yield reproducible ages. This may be because these Cenozoic sedimentary samples were not

buried deeply enough to be completely reset. The stratigraphic cover of the Yakutat terrane is thinner on the east than on the west, and if these sample were exhumed from very shallow depths, some detrital grains may retain pre-depositional ^4He . As a result, two of the resulting average ages (06STP71 and 06STP3) were not used for the contours on Figure 4.1 and were excluded from the regression plot in Figure 4.2b.

For the purposes of this study, we primarily focus on differences in apparent cooling ages, rather than estimates of exhumation rate. Assuming geothermal and topographic conditions are more or less uniform across the orogen, the 50-fold difference in cooling ages across the orogen should represent major differences in exhumation rate. However, it is still useful to consider what exhumation rates these young AHe ages may correspond to. Given the rapid cooling, a closure temperature approach is a suitable approximation for estimating exhumation rate. Closure temperatures for these rapidly-cooled samples should vary from $\sim 70\text{-}90$ °C, based on sample grain sizes and standard apatite diffusion parameters (Farley, 2000). Based on regional estimates of geothermal gradient in the absence of rapid denudation of 25 °C/km (Magoon, 1986; Johnsson et al., 1992; Johnsson and Howell, 1996), this range in closure temperature should correspond to closure depths of 2.8-3.6 km. However, it is likely that heat is advected due to rapid exhumation, such that the geothermal gradient is steeper. Using the 1-dimensional, steady-state thermokinematic solution to the crust's thermal profile from Reiners and Brandon (2006), the geothermal gradient could be elevated to ~ 46 °C/km if denudation rates are as high as 5 mm/yr, assuming reasonable boundary conditions for the orogenic wedge (layer thickness (L) of 10 km (the maximum stratigraphic thickness above

subducting Eocene oceanic crust of the accreting Yakutat terrane (Plafker et al., 1994)), and thermal parameters from Reiners and Brandon (2006) of thermal diffusivity $\kappa = 27.4 \text{ km}^2/\text{Ma}$, surface temperature $T_S = 0 \text{ }^\circ\text{C}$, basal temperature $T_L = 250 \text{ }^\circ\text{C}$ (for regional geothermal gradient of $25 \text{ }^\circ\text{C}/\text{km}$), and internal heat production $H_T = 4.5 \text{ }^\circ\text{C}/\text{Ma}$). Using this elevated geothermal gradient, AHe closure depths for the area of rapid cooling are 1.5-2 km, such that AHe contours of 0.5, 0.75, and 1.0 Ma on Figure 4.1 correspond to maximum time-averaged exhumation rates of 4.0, 2.7, and 2.0 mm/yr. This elevated geothermal gradient was also used for the exhumation rates in Figure 4.3.

Such rapid rates of exhumation are consistent with a poorly-defined age-elevation gradient from a near-vertical sample transect from just west of the Bering glacier. Three samples from Khitrov ridge define a very rough age-elevation gradient of $0.144 \text{ Ma}/\text{km}$ ($6.9 \text{ mm}/\text{yr}$) between 0.44 and 0.53 Ma (Figure 4.4). The zero-age intercept of this gradient occurs at 2.5 km below sea level, which given the $\sim 0.5 \text{ km}$ mean elevation of the area corresponds to $\sim 3.0 \text{ km}$ below the surface. The rate of exhumation required to bring the bottom sample to the surface from this depth is $6.8 \text{ mm}/\text{yr}$, such that the gradient and the intercept are mutually consistent. Using a closure temperature for these samples of $\sim 88 \text{ }^\circ\text{C}$, calculated iteratively based on grain size, diffusion characteristics (Farley, 2000), and the resulting cooling rate, the inferred geothermal gradient is $29 \text{ }^\circ\text{C}/\text{km}$. This implies even faster exhumation than estimated using the 1-dimensional model and $46 \text{ }^\circ\text{C}/\text{km}$ geothermal gradient. Age-elevation gradients can be affected by variations in isotherm shape associated with topography. Calculations by Mancktelow and Grasemann (1997) for a case of similar relief (1.5 km), topographic wavelength ($\sim 5 \text{ km}$), geothermal

gradient ($\sim 35^\circ \text{C/km}$), closure temperature (100°C), and exhumation rate (5 mm/yr), suggest that the age-elevation gradient could overestimate the exhumation rate by $\sim 20\%$. Given that the age-elevation gradient is poorly defined and likely overestimates exhumation rate, we use the result from the 1-dimensional model for our interpretations. However, this relief transect at least corroborates that exhumation rates in the area are very rapid.

Other effects of sample elevation and topography are not likely to alter the first order patterns of exhumation we infer for this area. Our estimates of exhumation rates at glacier ELAs (Figure 4.3) are based on calculations for individual samples using the 1-d closure temperature approach and basing the vertical distance traveled from closure depth on the local mean elevation in a 10-km-diameter circle (typical wavelength of the rugged glacial topography). Samples were also generally collected from ridge tops of comparable relief ($\sim 1\text{-}2 \text{ km}$) by helicopter. This should help minimize the effect of variable isotherm shape and deviations between local sample elevation and mean topography on inferred exhumation rates. Furthermore, given the typical 10-km-wavelength relief of $\sim 1\text{-}2 \text{ km}$ for most of the area (higher-relief parts of the orogen have not been sampled; Figure 4.1), the maximum difference in closure depths between locations should be less than a factor of two, which cannot account for the ~ 50 -fold difference in ages from north to south or the ~ 5 -fold difference within the rapidly-cooled windward flank. Based on this, we interpret the pattern of AHe ages to reflect spatial variations in exhumation rate.

Glaciological parameters and precipitation data

The source areas for the major southward-flowing glaciers in the St. Elias orogen were defined based on ice distributions on 1:250,000 USGS topographic maps (Figure 4.5). Divides were drawn based on the principle that ice flows down ice gradient, such that ice divides are the highest point on a continuous ice sheet that flows into multiple glacier systems. The glacier drainage areas upstream of equilibrium line altitudes (ELA) were calculated graphically and are listed in Table 4.2. These drainage areas include hillslopes above the glaciers and are thus larger than the surface area of ice above ELA, but are obviously only a subset of the total drainage basin of each glacier (i.e. extended to the glacier termini). Given that the maps used were in some cases decades old, and the fact that glaciers have receded in much of this region over the past century (Porter, 1989), the ice distributions and ELA shown should be considered approximate 20th century conditions.

Modern glacier ELAs were determined for large and small windward-flowing glaciers on the basis of topographic contours of the glacier surfaces from 1:250,000 scale USGS maps. ELAs for the glaciers shown in Figures 4.1 and 4.5 are listed in Table 4.2. This method is based on defining the boundary between accumulation and ablation areas on the glacier, where accumulating regions have concave contours and ablation areas have convex contours in the direction of glacier flow (Meierding, 1982; Mayo, 1986; Benn and Lehmkuhl, 2000). This technique is simple and can be performed using only topographic maps over a wide area, but provides only an approximation of true ELA. It is less accurate than other approaches, such as using field or airphoto observations of snowcover during the melt season, smaller glaciers, or other meteorological data. The

accumulation area ratio (AAR) technique could not be used, given that many glaciers flow directly into the ocean and experience ice removal by calving. However, the results obtained are consistent with regional syntheses of modern ELA (Péwé, 1975; Mayo, 1986).

More precise determination of modern ELAs would not enhance the comparison to AHe ages, given that uncertainties in paleo-ELAs are much larger (see below) and because ELAs should fluctuate significantly even at decadal timescales. Glaciers exhibit a prolonged response, called physical memory, to cyclic variations in precipitation in the absence of climate change (e.g. Pacific Decadal Oscillation), such that ELAs may routinely shift horizontally by up to several kilometers (Roe and O'Neal, in prep.). More recent airphotos and satellite imagery would also be affected by the rapid glacial retreat that has occurred in Alaska over the past few decades, and may thus not represent typical interglacial conditions. The use of coarse topographic maps ignore these short term fluctuations and may thus better approximate mean 20th century conditions. Nonetheless, uncertainties in the horizontal position of modern ELA are assumed to be at least ± 2 km.

Uncertainties in the position of paleo-ELA during glacial maxima periods outweigh errors in the position of modern ELA. Paleo-ELA is not well constrained along the windward flank of the orogen, given post-glacial-maximum erosion and deposition on the continental margin. We assumed ELA was ~ 300 m lower along the coast during glacial maxima, based on regional estimates (Péwé, 1975). ELAs during glacial maxima are not well constrained, however, and may have fluctuated throughout the Quaternary (e.g. the Illinoian glacial maximum ELA was lower than the last glacial maximum ELA;

Péwé, 1975). This assumption of paleo-ELA provides a weak lower bound of what we define as the “ELA front”, or the zone lying between modern and glacial-maxima ELA on the windward flank of the orogen. Based on errors in the elevation of paleo-ELA of at least ± 100 m and because of the gentle slope of the coastal plain, we assign ± 5 km horizontal uncertainty to the lower bound of the ELA front.

We compare these glaciological parameters to bedrock cooling and exhumation in several ways. The comparison between AHe age distribution and the position of the ELA front (Figures 4.1 and 4.2) should test how time-averaged, long-term denudation is associated with the zone of theoretically-greatest ice flux and erosion on individual glaciers (Andrews, 1972; Hallet, 1979; Anderson et al., 2006). This comparison is only approximate, however, given that the position of ELAs during glacial maxima are poorly constrained and that mean ELA may fluctuate due to changes in climate or topography over shorter (10^5 yr) timescales than the AHe cooling ages (10^6 yr). The comparison of long-term exhumation rates with variations in ice flux along strike is more poorly constrained (Figure 4.3). Modern glacier drainage areas at ELA should only approximate relative differences in modern ice discharge between glaciers, given that precipitation varies across the area by up to a factor of two (Figure 4.5) and due to other complicating variables which are not considered (e.g. aspect, albedo, etc.). Modern glacier drainage areas should be an even poorer representation of mean Quaternary ice discharge, given that precipitation patterns and glacier drainage divides could have varied between glacial cycles. Better constraints on the position of ELA during glacial maxima or climate-glacier flow models that predict the distribution of glaciers throughout the Quaternary

would improve this comparison. Given the likelihood that outlet glaciers have been fixed during at least the last few glacial cycles by Waxell-St. Elias ridge (see below), however, it is likely that the heterogeneity in modern drainage areas at least approximates how ice discharge has varied throughout multiple glacial intervals.

Existing precipitation data for the St. Elias orogen are sparse. Estimated isohyets of mean annual precipitation based on a regional climate summary of existing precipitation data and patterns of snow lines throughout the state of Alaska are shown in Figure 4.5 (Péwé, 1975). These isohyets have poor resolution and likely miss major spatial variations in precipitation associated with local topography. A second estimate of mean annual precipitation is from the Spatial Climate Analysis Center (2002) (Figure 4.5). This uses the statistical method *PRISM* (Parameter-elevation Regression on Independent Slopes Model), which combines historical point data for annual precipitation (from 1961-1990) with 2-km-resolution topography from a digital elevation model to estimate the effects of terrain on climate in mountainous regions (Daly et al., 1994). Although the *PRISM* precipitation data are based on similarly limited observations as Péwé (1975), we consider it more accurate because it accounts for the local effects of orography. The variation in precipitation for both sources are shown along the north-south transect (AA') in Figure 4.2. Neither appears to correlate with the location of the youngest AHe ages. However, the poor constraints on precipitation in this area severely limits this comparison with AHe age distribution.

Waxell-St. Elias Ridge

The zone of rapid denudation and the ELA front both occur south of a prominent east-west ridge, which forms an impressive barrier to ice flow in the St. Elias orogen. The Waxell-St. Elias ridge runs east-west, parallel to the coast, and consists of several discrete, elliptical segments that span a total of >300 km (Figures 4.1 and 4.6). Glaciers currently flow north to south through this barrier at only five locations, where major outlet glaciers with massive ice discharge occur (e.g. Bering and Malaspina glaciers; Figures 4.1, 4.5, and 4.6). During glacial maxima periods, it is likely that ice flow over this ridge occurred at only several other points, given its height relative to the probable elevation of the Bagley ice field behind it (Figure 4.6). This means that most of the ELA front would have been isolated from direct north to south ice flow across this barrier, thereby keeping ice discharge heterogenous along the range front during glacial maxima.

The prominent Waxell-St. Elias ridge may have also had an important influence on the pattern of glaciation and denudation in the orogen. The ridge exists partly due to motion of a backthrust under the Bagley ice field (Berger et al., in press), but is also due to the presence of very resistant bedrock (greenschist-amphibolite grade metasediment and metavolcanics; Plafker et al., 1994). As a result of this ridge, glaciers are unable to flow directly south across the orogen, resulting in just a few local outlet glaciers and considerable east-west ice flow north of the ridge (Figures 4.1 and 4.5). The zone of rapid denudation occurs just south of this ridge, within easily-eroded Cenozoic stratigraphy of the deforming Yakutat terrane. In contrast, the accumulation area of southward flowing outlet glaciers is floored by more resistant bedrock of the Prince William and Chugach terranes (Plafker et al., 1994). This may help facilitate denudation at the ELA front, by

resisting erosion in the north, trapping ice in the Bagley ice field, forcing ice flow through narrow outlets, and perhaps even by focusing orographic precipitation and ice-avalanching on the ELA front to the south. Without the Waxell-St. Elias ridge, the glacio-erosional evolution of the orogen may have been different, thus implying that physiogeologic setting has been an important part of this orogen's history.

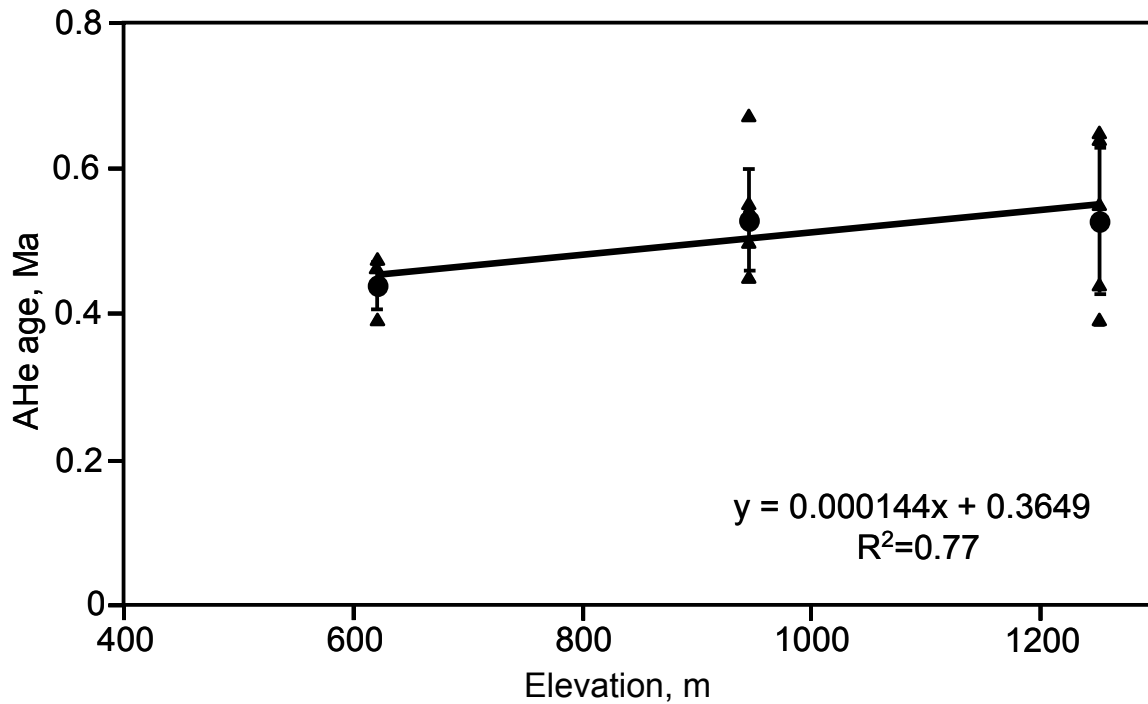
Additional references

- Benn, D.I., and Lehmkuhl, F., 2000, Mass balance and equilibrium line altitudes of glaciers in high-mountain environments, *Quat. Int.*, 65/66, 15-29.
- Berger, A.L., Spotila, J.A., Chapman, J., Pavlis, T., Enkelmann, E., Ruppert, N.A., and Buscher, J.T., in press, Architecture, Kinematics, and Exhumation of a Convergent Orogenic Wedge: A Thermochronological Investigation of Tectonic-Climatic Interactions within the Central St. Elias Orogen, Alaska: *Earth and Planetary Science Letters*.
- Daly, C., Neilson, R.P., and Phillips, D.L., 1994, A statistical-topographic model for mapping climatological precipitation over mountainous terrain, *Journal of Applied Meteorology*, 33, 140-158.
- Ehlers, T., and Farley, K., 2003, Apatite (U-Th)/He thermochronometry: methods and applications to problems in tectonics and surface processes, *Earth and Planetary Science Letters*, 206, 1-14.
- Farley, K.A., 2000, Helium diffusion from apatite: General behavior as illustrated by Durango fluorapatite: *Journal of Geophysical Research*, 105, 2903-2914.
- Farly, K.A., and Stockli, D.F., 2002, (U-Th)/He dating of phosphates: apatite, monazite, and xenotime, in *Phosphates: Geochemical, Geobiological, and Materials Importance*, *Rev. Mineral. Geochem.*, vol. 48, 559-577.
- Fitzgerald, P.G., Baldwin, S.L., Webb, L.E., and O'Sullivan, P.B., 2006, Interpretation of (U-Th)/He single grain ages from slowly cooled crustal terranes: A case study

- from the Transantarctic Mountains of southern Victoria Land: *Chemical Geology*, 225, 91-120.
- House, M.A., Wernicke, B.P., Farley, K.A., and Dumitru, T.A., 1997, Cenozoic thermal evolution of the central Sierra Nevada from (U-Th)/He thermochronometry. *Earth Planet. Sci. Lett.*, 151, 167-179.
- Mancktelow, N.S., and Grasemann, B., 1997, Time-dependent effects of heat advection and topography on cooling histories during erosion, *Tectonophysics*, 270, 167-195.
- Mayo, L.R., 1986, Annual runoff rate from glaciers in Alaska: A model using the altitude of glacier mass balance equilibrium, in D.L. Kane (ed.), *Cold Regions Hydrology Symposium*, Amer. Water Res. Assoc., Bethesda, Maryland, 509-517.
- McDowell, F.W., McIntosh, W.C., and Farley, K.A., 2005, A precise $^{40}\text{Ar}/^{39}\text{Ar}$ reference age for the Durango apatite (U-Th)/He and fission-track dating standard: *Chemical Geology*, 214, 249-263.
- Meierding, T.C., 1982, Late Pleistocene glacial equilibrium-line altitudes in the Colorado front range: A comparison of methods: *Quat. Res.*, 18, 289-310.
- Meigs, A., and Sauber, J., 2000, Southern Alaska as an example of the long-term consequences of mountain building under the influence of glaciers, *Quat. Sci. Reviews*, 19, 1543-1562.
- Péwé, T.L., 1975, Quaternary geology of Alaska, U.S. Geol. Surv. Professional Paper, 835, 139 p.

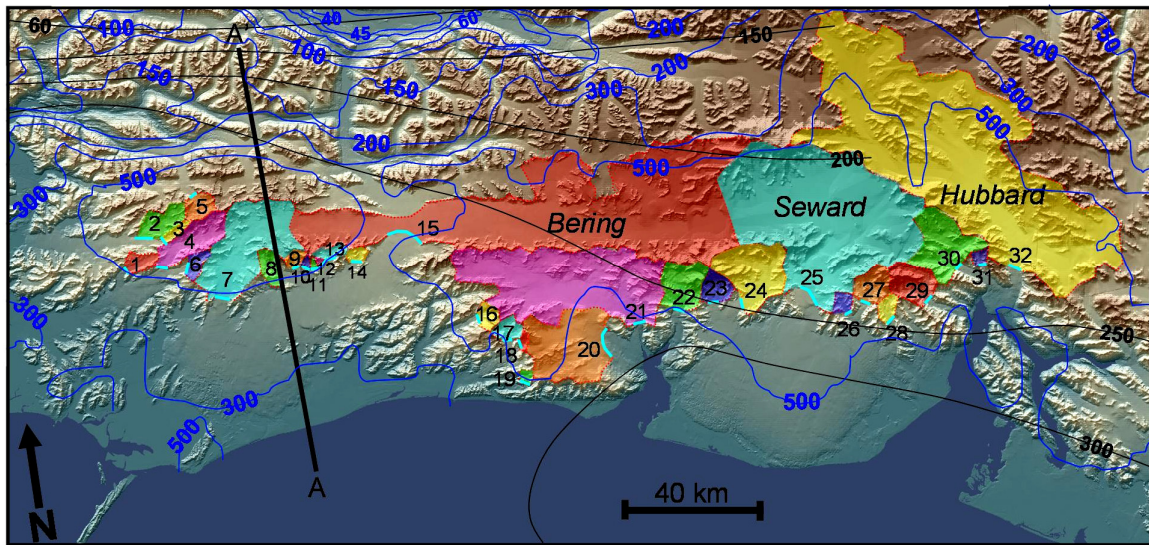
- Porter, S.C., 1989, Late Holocene fluctuations of the fjord glacier system in Icy Bay Alaska, *Arctic and Alpine Research*, 21, 364-379.
- Reiners, P.W., and Brandon, M.T., 2006, Using thermochronology to understand orogenic erosion, *Ann. Rev. Earth and Planet. Sci.*, 34, 419-466.
- Reiners, P.W., and Nicolescu, S., in press, Measurement of parent nuclides for (U-Th)/He chronometry by solution sector ICP-MS, *Geochim. Cosmochim. Acta*.
- Roe, G. and O'Neal, M.A., in prep., The response of glaciers to intrinsic climate variability: observations and models of late Holocene variations in the Pacific Northwest, *J. Glaciology*.
- Spatial Climate Analysis Center, 2002, PRISM 1961-1990 Mean Annual Precipitation: Alaska, Oregon Climate Service, Oregon State University, via The Climate Source, http://www.cimatesouce.com/ak/fact_sheets/akppt_xl.jpg.
- Spotila, J.A., Buscher, J., Meigs, A., and Reiners, P., 2004, Long-term glacial erosion of active mountain belts: Example of the Chugach-St. Elias Range, Alaska, *Geology*, 32, 501-504.
- Wolf, R.A., Farley, K.A., and Silver, L.T., 1996, Helium diffusion and low-temperature thermochronometry of apatite, *Geochim. Cosmochim. Acta*, 60, 4231-4240.

Figure 4.4: AHe age versus elevation.



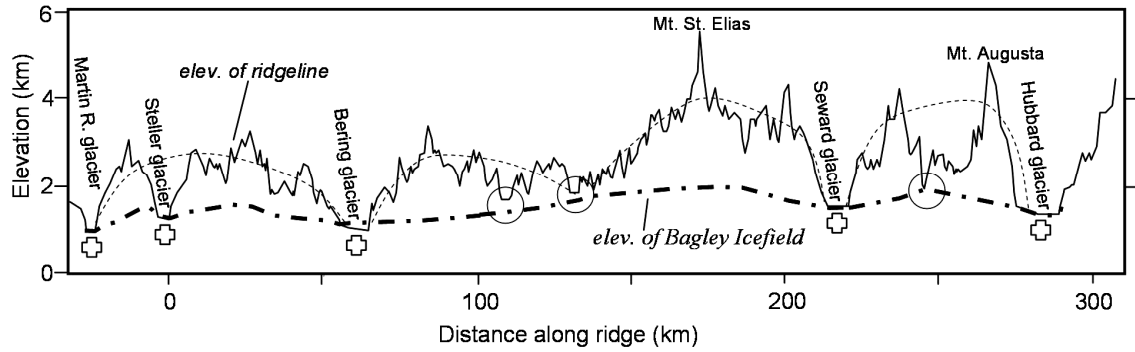
Vertical AHe transect at Khitrov ridge, just west of the Bering glacier. The samples represented are (from highest to lowest) 05STP3, 05STP1, and 05STP2 (Figure 4.1). Individual age determinations are shown as triangles, whereas the average age for each sample is shown as a large circle. Error bars for the average ages are given for the standard deviation of individual analyses (1σ). The regression is based on the three average ages, rather than on all individual age determinations, with age as the dependent variable. Regression equation shown at bottom right.

Figure 4.5: Map of glacier drainage basins and precipitation.



Glacier drainage basins of the St. Elias orogen, overlain on shaded relief map from USGS 60-m DEMs. Glacier basins were mapped using 1:250,000 scale topographic maps, based on the elevation of the glacier surface and direction of the ice-surface gradient (*cf.* Mayo, 1986). Only glaciers that drain southwards or eastwards are shown; smaller glaciers on the leeward flank of the range are not plotted. ELAs of each glacier are shown as the bright blue lines and were determined based on the boundary between concave (above ELA) and convex (below ELA) ice contours (*cf.* Péwé, 1975). The names, drainage areas, and ELAs of each numbered glacier are listed in Table 4.2. Two sets of isohyets of mean annual precipitation (cm/yr) are shown. Those in black are from the regional climate summary of Péwé (1975). Those in blue are from PRISM model of recent precipitation data (Spatial Climate Analysis Center, 2002). Line AA' indicates profile used to construct Figure 4.2.

Figure 4.6: Topographic profile of hanging wall of the Bagley fault.



West to east profile of Waxell-St. Elias ridge (BB', Figure 4.1). Maximum elevation along the circuitous ridge line is from 1:250,000 scale maps. The ridge is comprised of four elliptical sections (dashed lines) separated by outlet glaciers. Height of the modern surface of the Bagley ice field to the north is shown as heavier dashed line. Ice currently cuts through the ridge at only five locations (denoted by stars), and may have flowed over the ridge during glacial maxima at three additional spots (denoted by circles).

Table 4.1: AHe data

Sample	Elev. (m)	Latitude	Longitude	Lithology	# Grains	Mass (mg)	Ft	U ppm	Th ppm	MWAR	He pmol	Age (Ma)	Avg. (Ma)	% SD	
05STP1-1	946	60.4208°	-143.5028°	arkose (K ulthieth)	7	0.0311	0.796	23.5	36.9	63.0	0.0019	0.45	0.53±0.07	±14.2%	
					-2	8	0.0526	0.820	25.3	26.4	77.8	0.0048			0.67
					-3	8	0.0323	0.767	22.6	31.3	61.1	0.0021			0.55
					-4	8	0.0603	0.826	24.1	7.85	81.8	0.0036			0.54
					-5	4	0.0419	0.838	6.28	6.82	82.4	0.0007			0.50
					-6	4	0.0320	0.837	15.4	31.0	85.6	0.0014			0.45
05STP2-1	620	60.3931°	-143.5422°	arkose (K ulthieth)	16	0.0377	0.743	25.0	36.6	51.9	0.0019	0.39	0.44±0.03	±6.9%	
					-2	15	0.0342	0.736	41.1	42.3	50.6	0.0029			0.43
					-3	16	0.0455	0.759	37.6	60.0	55.3	0.0043			0.46
					-4	11	0.0403	0.771	34.6	21.1	61.7	0.0030			0.47
					-5	13	0.0487	0.777	33.5	23.9	60.6	0.0036			0.47
					05STP3-1	1252	60.4332°	-143.5044°	arkose (K ulthieth)	14	0.0446	0.755			29.0
-2	7	0.0569	0.823	37.1	29.1	84.9	0.0070	0.65							
-3	12	0.0458	0.866	17.7	17.7	59.2	0.0018	0.39							
-4	9	0.0435	0.798	39.5	46.2	71.0	0.0040	0.44							
-6	3	0.0211	0.836	15.2	22.4	79.2	0.0010	0.55							
05STP4-1	394	60.3896°	-143.6997°	arkose (K ulthieth)	6	0.0411	0.830	10.1	16.2	74.4	0.0021	0.86	0.74±0.07	±9.7%	
					-2	6	0.0341	0.803	22.5	30.4	65.8	0.0031			0.73
					-3	5	0.0416	0.819	58.2	64.4	76.0	0.0093			0.72
					-4	5	0.0391	0.825	28.5	25.9	74.2	0.0046			0.78
					-5	6	0.0556	0.837	11.6	15.1	82.3	0.0023			0.62
					-6	6	0.0559	0.827	46.1	38.1	77.4	0.0100			0.75
05STP7-1	1140	60.8838°	-143.7637°	gneiss (Chugach)	6	0.0380	0.810	95.2	2.3	72.7	0.3984	25.9	25.1±0.87	±3.5%	
					-2	4	0.0270	0.832	100.5	0.6	78.1	0.2982			25.3
					-3	5	0.0201	0.777	109.3	0.6	57.9	0.2269			25.4
					-4	10	0.0142	0.728	75.3	1.0	42.2	0.0962			23.6
05STP11-1	1448	60.5428°	-143.4165°	sandstone (Orca Group)	5	0.0157	0.765	36.0	28.6	56.0	0.0463	17.3	1.78±0.83	±46.7%	
					-2	13	0.0146	0.678	61.0	36.0	38.0	0.0103			2.86
					-3	15	0.0164	0.675	43.8	36.2	39.9	0.0050			1.64
					-4	15	0.0164	0.658	22.6	26.2	40.8	0.0014			0.84
05STP15-1	488	60.2306°	-143.9758°	sandstone (Poul Creek)	15	0.0278	0.715	23.6	26.6	46.7	0.0055	1.76	1.80±0.11	±6.1%	
					-2	1	0.0212	0.895	1.97	6.52	101.2	0.0080			22.8
					-3	16	0.0287	0.726	28.0	35.9	49.3	0.0069			1.72
					-4	16	0.0307	0.728	29.1	29.2	46.9	0.0105			2.47
					-5	10	0.0222	0.723	13.5	13.1	47.2	0.0028			1.99
					-6	10	0.0204	0.728	46.0	26.8	48.2	0.0071			1.74
					-7	1	0.0265	0.884	2.17	7.24	105.8	0.0130			2.71
05STP26-1	2208	60.6469°	-143.7903°	granite (Chugach)	16	0.0218	0.706	111	0.7	42.5	0.0190	2.14	2.28±0.16	±6.9%	
					-2	14	0.0184	0.690	104	0.4	42.0	0.0142			2.06
					-3	11	0.0205	0.728	98.3	1.0	50.1	0.0179			2.35
					-4	5	0.0192	0.794	135	0.9	61.5	0.0239			2.23
					-5	2	0.0173	0.828	112	1.6	71.2	0.0212			2.54
					-6	4	0.0285	0.831	114	1.1	76.5	0.0331			2.36
05STP27-1	1704	60.4996°	-143.7248°	arkose (K ulthieth)	15	0.0166	0.665	34.2	53.8	39.4	0.0017	0.63	0.63±0.11	±17.5%	
					-2	12	0.0176	0.700	36.5	41.4	41.5	0.0022			0.74
					-3	19	0.0186	0.670	39.1	43.4	36.6	0.0024			0.76
					-4	7	0.0191	0.787	19.3	33.1	56.0	0.0010			0.46
					-5	10	0.0217	0.727	31.8	55.3	47.4	0.0021			0.57
05STP33-1	2758	60.6441°	-143.7239°	granite (Chugach)	7	0.0584	0.850	66.4	23.9	78.4	0.0334	1.79	1.66±0.09	±5.6%	
					-2	6	0.0623	0.845	73.2	27.6	84.8	0.0334			1.53
					-3	10	0.0743	0.831	67.6	25.2	75.7	0.0379			1.60
					-4	9	0.0454	0.816	71.1	27.5	64.9	0.0238			1.58
					-5	3	0.0363	0.859	69.2	20.2	92.5	0.0206			1.70
					-6	4	0.0296	0.826	76.0	26.7	76.2	0.0183			1.74
06STP1-1	1189	60.1686°	-140.5297°	sandstone (Poul Creek/ Yakataga)	16	0.0255	0.717	44.5	61.5	44.3	0.0094	1.65	1.55	>20%	
					-2	8	0.0290	0.771	32.2	37.4	58.2	0.0267			5.54
					-3	8	0.0226	0.753	34.4	44.0	52.3	0.0058			1.45
					-4	16	0.0216	0.714	29.4	33.2	43.5	0.0145			4.82
					-5	16	0.0235	0.721	39.2	39.2	43.8	0.0402			8.78
06STP3-1	1713	60.1643°	-140.3476°	sandstone (Poul Creek)	17	0.0254	0.730	44.0	40.7	47.4	0.0386	7.41	7.21±1.16	±16.1%	
					-2	12	0.0201	0.724	26.5	35.9	47.7	0.0225			8.41
					-3	4	0.0146	0.759	40.0	41.3	55.5	0.4309			148
					-4	4	0.0110	0.743	15.0	12.2	50.1	0.0041			5.30
					-5	7	0.0238	0.753	59.6	17.8	56.2	0.0734			122
					-6	15	0.0123	0.645	45.7	52.5	35.9	0.0187			7.72
					-7	10	0.0138	0.733	33.6	20.7	47.6	0.0275			13.5
06STP4-1	1676	60.2369°	-140.4611°	quartzite (Orca Group)	14	0.0204	0.713	13.5	16.2	45.0	0.00038	1.44	0.56±0.08	±15.3%	
					-2	18	0.0207	0.680	28.3	38.1	39.1	0.00031			0.59
					-3	10	0.0154	0.703	6.3	18.0	44.5	0.00007			0.44
					-4	11	0.0130	0.699	47.4	55.3	41.4	0.00161			1.80
					-5	11	0.0130	0.684	26.0	30.9	39.4	0.00031			0.64
06STP50-1	875	60.4488°	-143.9837°	sandstone (K ulthieth)	19	0.0244	0.678	55.0	54.1	40.3	0.0060	1.02	1.09±0.09	±8.3%	
					-2	18	0.0221	0.684	48.6	63.6	39.6	0.0062			1.23
					-3	19	0.0254	0.689	46.0	56.9	40.6	0.0054			1.00
					-4	19	0.0247	0.691	45.4	53.5	39.7	0.0056			1.09

Table 4.1: AHe data Continued.

Sample	Elev. (m)	Latitude	Longitude	Lithology	# Grains	Mass (mg)	Ft	U ppm	Th ppm	MWAR	He pmol	Age (Ma)	Avg. (Ma)	% SD
06STP71-1	853	60.1333°	-140.7119°	sandstone (Yakataga)	10	0.0230	0.752	38.2	26.4	53.5	0.0215	<i>5.35</i>	3.95±1.06	±26.8%
-2					8	0.0169	0.738	52.3	30.8	49.6	0.0145	3.73		
-3					7	0.0151	0.744	91.1	104	48.6	0.0577	8.47		
-4					13	0.0292	0.733	45.6	36.5	50.8	0.0169	2.78		
-5					6	0.0173	0.769	29.9	18.5	55.3	0.0193	8.08		
01CH22-1	1532	60.9104°	-144.3150°	schist (Chugach)	11	0.0077	0.637	33.3	17.8	33.1	0.0194	<i>20.1</i>	18.9±1.20	±6.3%
-2					12	0.0035	0.521	38.6	17.3	25.7	0.0072	17.7		
01CH25-1	320	60.6940°	-144.3774°	phyllite (Chugach)	20	0.0171	0.662	116.8	16.7	36.4	0.0708	<i>9.92</i>	10.7±1.31	±12.3%
-2					2	0.0068	0.750	50.3	6.9	56.7	0.0134	9.71		
-3					20	0.0174	0.658	108.1	10.6	36.5	0.0695	10.5		
-4					13	0.0204	0.710	65.8	4.0	46.4	0.0515	10.2		
-5					8	0.0130	0.715	67.6	30.6	42.4	0.0716	19.7		
-6					12	0.0222	0.738	92.8	12.9	51.9	0.1092	13.3		
01CH26-1	884	60.4990°	-144.4772°	granitoid (Chugach)	4	0.0103	0.797	24.0	15.0	55.5	0.0021	<i>1.79</i>	2.02±0.14	±7.2%
-2					5	0.0095	0.751	32.0	18.8	50.3	0.0028	2.04		
-3					6	0.0170	0.752	30.3	16.8	54.3	0.0050	2.19		
-4					7	0.0176	0.748	30.3	18.5	51.2	0.0049	2.06		
02CH28-1	1625	60.2573°	-141.1584°	graywacke (Kulthieth)	12	0.0217	0.704	14.9	19.3	49.5	0.0034	<i>2.19</i>	0.74±0.14	±18.7%
-2					15	0.0234	0.691	18.3	30.1	46.2	0.0012	0.55		
-3					11	0.0242	0.721	19.2	16.6	54.2	0.0018	0.87		
-4					14	0.0243	0.718	17.5	19.0	47.9	0.0016	0.81		

Ages in italics were considered outliers and not used for average age calculation. Elev. = sample elevation in meters; Ft = alpha particle ejection correction factor after Farley et al. (1996); MWAR = mass weighted average radius of sample (μm); Avg. = average AHe age (Ma); % SD = standard deviation of average age as a percentage of the average age; Chugach = Chugach terrane. Yakataga, Poul Creek, and Kulthieth are formations in the Yakutat terrane. Orca Group is a formation in the Prince William terrane.

Table 4.2: Glacier data.

#	Glacier	ELA (m)	Drainage Area (km ²)	Exhumation Rate (mm/yr)
1	"Martin River West"	732		43 2.0
2	Miles	1006		135 1.5
3	"Mt. Tom White"	1341		20 1.5
4	Martin River	853		176 2.5
5	Fan	1372		65 2.5
6	"Martin River East"	1036		42 3.0
7	Stellar	671		575 5.0
8	"Khitrov"	853		51 4.0
9	"Mt. Stellar A"	1036		20 3.0
10	"Mt. Stellar B"	975		8 3.0
11	"Mt. Stellar C"	914		8 3.0
12	"Mt. Stellar D"	914		9 2.7
13	"Mt. Stellar E"	1036		36 2.7
14	"Mt. Stellar F"	975		24 2.7
15	Bering	1128		2516 3.0
16	Leeper	732		30 3.3
17	Yakataga	914		49 2.0
18	Yaga	914		24 1.5
19	White River	762		22 1.5
20	Guyot	671		397 2.5
21	Yhatse	610		1109 2.7
22	Tyndall	701		166 2.8
23	Libby	792		75 2.5
24	Agassi	853		308 2.5
25	Seward	914		1949 4.0
26	"Marvine West"	823		27 2.0
27	Marvine	823		115 2.0
28	Hayden	732		55 2.0
29	Turner	792		124 2.0
30	Valerie	853		272 2.0
31	"Mt. Foresta"	1097		23 2.0
32	Hubbard	732		3406 2.7

Numbers refer to glaciers numbered in Figure 2, from west to east. Glacier names are from 1:250,000 USGS topographic maps; those in parentheses have no official name. ELA (equilibrium line altitude) was measured based on contour shape on 1:250,000 USGS topographic maps in feet, converted to meters. Drainage area was measured graphically based on ice divides following ice surface gradients from 1:250,000 USGS topographic maps. Exhumation rates are based on contours on Figure 4.1.

Chapter 5

Quaternary Tectonic Response to Intensified Glacial Erosion in an Orogenic Wedge

AARON L. BERGER¹, SEAN P. S. GULICK², JAMES A. SPOTILA¹, JOHN M.
JAEGER³, JAMES B. CHAPMAN⁴, LINDSAY A. LOWE², TERRY L. PAVLIS⁴,
KENNETH D. RIDGWAY⁵, BRYCE WILLEMS⁶, and RYAN J. MCALEER¹

¹Department of Geosciences, Virginia Tech, Blacksburg, VA 24061, USA

*²Institute for Geophysics, Jackson School of Geosciences, University of Texas at Austin,
Austin, TX 78758, USA*

³Department of Geological Sciences, University of Florida, Gainesville, FL 32611, USA

*⁴Department of Geological Sciences, University of Texas El Paso, El Paso, TX 79968,
USA*

*⁵Department of Earth and Atmospheric Sciences, Purdue University, West Lafayette, IN
47907, USA*

*⁶Department of Geology and Environmental Geosciences, Northern Illinois University,
DeKalb, IL 60115, USA*

Submitted to *Nature Geoscience*, 2008

ABSTRACT

Spatial and temporal variations in climate have been shown to have a profound influence on denudation, topography, and deformation in orogenic systems (Molnar and England, 1990; Willett, 1990; Beaumont et al., 1992). Nonetheless, the impact of the most severe transition in climate during Cenozoic time, the Late Neogene and Pleistocene onset and advance of glaciers, has hitherto not been empirically defined via comprehensive analysis of orogen kinematics. Here we analyze spatial patterns and temporal variations in denudation and deformation in a heavily glaciated collision belt, the St. Elias orogen in southern Alaska, using low-temperature thermochronometry (Berger et al., in press; Berger and Spotila, in review) and offshore seismic reflection and borehole data (Zellers, 1995; Gulick et al., 2007; Lowe et al., in press). The synthesis of these independent datasets suggest that global-scale glacial intensification in mid-Pleistocene time enhanced glacier coverage and caused ice-streams to advance to the edge of the continental shelf, thereby augmenting and concentrating denudation across the subaerial reaches of the orogen and burying the submarine deformation front. We propose that this climatically driven mass redistribution forced the structural reorganization of the orogen to maintain critical Coulomb taper, including out-of-sequence thrusting in the hinterland, firm establishment of double vergence via accelerated backthrust motion, and narrowing of the actively-deforming wedge. Numerical modeling has traditionally been the primary basis for the paradigm that orogenic evolution reflects a marriage between atmospheric and tectonic processes (Whipple and Meade, 2004; Stolar et al., 2006; Tomkin and Roe, 2007); strikingly, our

observations from a natural system confirm and elucidate the impact of climate change on tectonics.

INTRODUCTION

The kinematic evolution of real-world orogenic systems during concomitant Late Cenozoic cooling is an ideal but underutilized phenomenological venue for quantifying the interplay between plate tectonics and global climate (Molnar and England, 1990; Lamb and Davis, 2003; Huntington et al., 2006). Linkages between these interacting systems are commonly explored using numerical models of critical Coulomb wedges (Beaumont et al., 1992; Willett, 1999). Within critical wedges, linked deformation and erosion maintain mean orogen surface gradients (Davis et al., 1983; Dahlen et al., 1984), such that orogen form is coupled to climatically influenced denudation pattern and intensity (Beaumont et al., 1992; Willett, 1999). Within an orogen dominated by processes of fluvial erosion, an increase in erosional intensity is predicted to accelerate rock uplift while decreasing orogen width and relief (Whipple and Meade, 2004; Stolar et al., 2006). As glacial erosion can be more effective than fluvial erosion (Brocklehurst and Whipple, 2002; Montgomery, 2002), a climate shift towards glacially-dominated denudation should have an observable impact on orogenesis. Numerical simulations of glaciated critical wedges predict that Late Cenozoic alpine glaciation should have intensified and redistributed erosion to follow patterns of ice flux, thereby reducing mean topography, contracting orogen width, and forcing widespread structural reorganization (Tomkin and Roe, 2007; Tomkin, 2007). Empirical studies have lagged behind models,

however, and examples of these responses have not previously been linked to global cooling in a real-world orogen.

BACKGROUND

The St. Elias orogen is a product of the ongoing oblique collision of the Yakutat terrane into the North American plate since Middle Miocene time (Plafker et al., 1994; Bruhn et al., 2004). Deformation is currently focused on the windward flank of the orogen within a thin-skinned fold and thrust belt that accommodates ~ 3 cm/yr of shortening (Figure 5.1) (Plafker et al., 1994; Bruhn et al., 2004). This thrust belt may be approximated as a critical Coulomb wedge, as it lies above a subducting slab and is composed of poorly-indurated, offscraped Cenozoic stratigraphic units with a tapered mean topographic profile (Plafker et al., 1994). The orogen has rugged coastal topography that receives heavy orographic precipitation of ~ 3 -6 m/yr, which decreases to < 0.6 m/yr on the leeward flank (P  w  , 1975; Berger and Spotila, in review). Half of the orogen is currently covered by erosive, wet-based glaciers that extend to sea-level and can move 100s of meters per year (Figure 5.1). During late Pleistocene glacial maxima, regional ice coverage was nearly complete and reached the shelf edge via now-submerged sea valleys (Figure 5.1) (P  w  , 1975). The history of glacial expansion is constrained by oxygen isotopes and syn-orogenic strata within the Gulf of Alaska (Figure 5.2) (Logoe and Zellers, 1996; Zachos et al., 2001; Lisiecki and Raymo, 2005). Synchronous with global cooling, the concentration of ice rafted sediments indicate that moderate glaciation initiated at ~ 5.5 Ma (glacial interval A), but waned during the Mid-Pliocene Warm Interval (~ 4.2 -3.0 Ma). Glaciation returned as part of northern

hemisphere cooling from ~3-2.5 Ma (glacial interval B), and, based partly on our new data, significantly intensified in mid-Pleistocene time (deemed glacial interval C, which continues to the present). We suggest this intensification was due to a regional glacial response to a global change from 40 to 100 Kyr glacial-interglacial climate cycles, which occurred at ~0.7-1 Ma (Berger and Jansen, 1994; Clark et al., 2006). Glacial intervals B and C corresponded to increases in detrital flux into the Gulf of Alaska, including a doubling of terrigenous sediment flux to the distal Surveyor Fan since ~1 Ma (Figure 5.2) (Rea and Snoeckx, 1995; Lagoe and Zellers, 1996). Because regional modifications of Pacific-North America plate motion are not known to have occurred in Plio-Pleistocene time (Plafker et al., 1994; Bruhn et al., 2004), these sediment pulses suggest that glaciation increased erosion. In particular, we contend that the onset of glacial interval C played a critical role in the evolution of the orogen.

ANALYTICAL METHODS

Thermochronometry data and methods used for this work are presented in detail in supporting publications (Berger et al., in press; Berger and Spotila, in review), although the pattern and history of exhumation are shown here (Figures 5.1, 5.2, and 5.3). AHe, AFT, and ZHe thermochronometers have typical closure temperatures of ~70°, 110°, and 180° C, respectively. Closure temperatures vary in detail, depending on grain size and sample cooling rate, and were estimated using standard procedures and mineral parameters. For the background conditions in the St. Elias orogen (geothermal gradient of 25-30 °C/km), typical closure temperatures of these mineral systems reflect the history of

exhumation from depths ~2-7 km (Berger et al., in press; Berger and Spotila, in review). Rates of exhumation on the windward flank of the orogen are sufficiently high that advection of heat towards the Earth's surface should result in a steeper geothermal gradient. Based on calculations, near surface geothermal gradients in the zone of youngest AHe ages may be as high as 45 °C/km (Berger and Spotila, in review). To account for advection, the geothermal gradients used to estimate exhumation rates for individual samples were adjusted between 30-45 °C/km within the wedge and assumed to be 25 °C/km on the leeward flank.

The marine seismic data presented here were collected in 2004 aboard the R/V Maurice Ewing. We acquired ~1800 km of high-resolution seismic-reflection profiles along the Gulf of Alaska continental margin using dual 45/45 cu. in. GI airguns with a better than 5-m vertical resolution (Gulick et al., 2007). Processing included trace regularization, normal moveout correction, bandpass filtering, muting, frequency-wavenumber filtering, stacking, water-bottom muting, and finite-difference migration. Glacial erosion surfaces were identified in the data based on stratal truncations and associated chaotic reflectivity indicative of diamicton formed in ice proximal/marginal settings (Powell and Cooper, 2002). Approximate chronology (Figure 5.4) was established by correlating sequences beneath the angular unconformity near the shelf edge on the 2004 data with the strata drilled by industry and dated biostratigraphically (Zellers, 1995). In particular, the last observation of the Pliocene planktonic foraminifera *Neogloboquadrina asanoi* at ~2250 mbsf in Exxon well #50 places the seismically

imaged strata pursuant to the paper in the Pleistocene and the angular unconformity as mid-Pleistocene (Figure 5.4).

BEDROCK THERMOCHRONOMETRY

Low-temperature apatite (U-Th)/He thermochronometry (AHe) constrains the exhumation pattern in the St. Elias orogen (Spotila et al., 2004; Berger et al., in press, Berger and Spotila, in review). Time-averaged cooling rates indicate that the most rapid exhumation occurs within a narrow east-west band on the windward flank of the orogen that correlates with the “ELA front”, or the intersection of mean Quaternary glacier equilibrium altitude (ELA) and mean topography (Berger and Spotila, in review) (Figures 5.1 and 5.3). This zone of rapid exhumation cuts across structural trend and is more concentrated than orographic precipitation, suggesting that denudation is focused by maximum Quaternary ice flux, which should occur at mean ELA (Andrews, 1972; Tomkin, 2007; Tomkin and Roe, 2007) (Figure 5.3). Exhumation is an order of magnitude slower on the leeward flank, which has been interpreted to be a deformational backstop that is isolated from the deforming wedge by an active backthrust that makes the orogen doubly-vergent (Berger et al., in press) (Figures 5.1 and 5.3). However, higher temperature apatite fission-track (AFT) and zircon (U-Th)/He (ZHe) thermochronometry (Berger et al., in press; Johnston, 2005) indicate that this pattern has only been in place during the Quaternary. Cooling rates across the windward flank increased dramatically at ~1 Ma, but have remained slow and steady on the leeward flank (Figures 5.2 and 5.3). The acceleration of cooling in the wedge corresponded to an increase in average

denudation rate from ~ 0.3 to 3 mm/yr ($\pm 25\%$) and required motion along the backthrust to increase. The timing of these changes is roughly coeval with intensification of glaciation at the onset of glacial interval C (Figure 5.2).

OFFSHORE SEISMIC

The offshore record indicates that the Pleistocene increase in denudation across the subaerial deforming wedge corresponded to increased deposition and structural reorganization offshore. High-resolution seismic images acquired along the Bering Trough and across the seaward deformation front (the Pamplona Zone) constrain sedimentation, ice coverage, and deformation on the continental shelf (Figures 5.1 and 5.4). An irregular angular unconformity that truncates underlying stratigraphy occurs near the shelf-edge (Figure 5.4a). Based on correlation with biostratigraphic studies on industry wells (Zellers, 1995), this unconformity formed in mid-Pleistocene time and marks the onset of what we refer to as glacial interval C. We interpret this unconformity to represent the first ice advance that extended beyond the present inner continental shelf (<25 km from the modern coast) and subsequently crossed the entire submarine extent of the deforming wedge to the edge of the continental shelf (Figure 5.4a). Two additional seismic profiles show that this unconformity occurs outside of the modern sea valley and was thus produced by a regional erosional event (Figure 5.4b). These profiles also show that the morphological sea valley did not form until after this regional erosional event, implying that the glacial advances to the shelf-edge corresponded with a transition in glacial morphology from broad zones of ice (perhaps analogous to piedmont glaciers) to focused ice streams that carried greater ice discharge.

The mid-Pleistocene unconformity also represents a transition in deformation across the submarine extent of the orogenic wedge. Prior to the advance of ice streams to the edge of the continental shelf, the Pamplona Zone experienced long-wavelength folding and related faulting (Figure 5.4a). Growth strata between 1.5 and ~0.5 Ma indicate that these structures were buried during their latest growth, but ultimately shut-down in mid-Pleistocene time as erosion beveled the tops of the folds. Since this shelf-wide erosional resurfacing, ~200 and ~400 m of undeformed sediment has accumulated in and adjacent to the Bering Trough, respectively. Although minor shortening still occurs on the most seaward structure of the Pamplona Zone outside of the Bering Trough (Lowe et al., in press), it is likely too small to significantly affect wedge taper. The lack of significant active shortening across the toe of the wedge is unusual, given the expectation that the frontal thrusts of a critical wedge should accommodate the greatest fraction of convergence (Davis et al., 1983; Dahlen et al., 1984). These results imply that the cessation of shortening across the offshore extent of the wedge was coeval with, and causally related to, both augmented onshore denudation and lowering of the submarine critical taper by subsequent sedimentary burial. We suggest both are a product of increased glacier coverage at the onset of glacial interval C and represent an example of climate forced tectonic changes.

ARCHITECTURAL MODEL

Based on the above synthesis of onshore and offshore observations, we propose a new kinematic model for the Quaternary evolution of the St. Elias orogen and examine it

in the context of change to a cooler glacial climate. Prior to the increase in glacier coverage in mid-Pleistocene time (glacial interval C), denudation rates across the upper, subaerial portion of the orogenic wedge were relatively slow ($\sim 35 \text{ km}^2/\text{Myr}$ unit flux) and deformation extended from the backthrust to the offshore, forearc limit of the Pamplona Zone (Figure 5.5a). Since the onset of glacial interval C, denudation rates across the subaerial wedge have increased ($\sim 190 \text{ km}^2/\text{Myr}$ unit flux) and become focused at the ELA front. This change required accelerated motion along both the backthrust and a vertically stacked array of hinterland forethrusts (Figure 5.5b). At the same time, the offshore wedge was buried by sediment and became inactive. Based on mass balance, $\sim 20\%$ of the sediment supplied by increased glacial erosion currently covers the inactive offshore wedge; the remainder was likely transported farther offshore to the Surveyor Fan (Rea and Snoeckx, 1995). Periodic glacial advances may erode a fraction of this cover and redeposit it on the slope and fan, but the eroded material is replaced by renewed deposition during interglacial periods. This kinematic evolution fits with the classic model of critical Coulomb wedges, in which perturbations in denudation lead to structural reorganization and out-of-sequence thrusting to maintain critical taper (Davis et al., 1983; Dahlen et al., 1984; Whipple and Meade, 2004; Stolar et al., 2006). In this case, Quaternary climate change appears to have focused glacial denudation across the subaerial wedge resulting in increased rock uplift via accelerated thrust motion, while coeval glaciogenic deposition lowered the submarine critical taper and stabilized offshore structures via load-induced normal stress (Figure 5.5c).

A consequence of the shutting-off of the offshore Pamplona Zone is that the inactive wedge has been progressively consumed by the active onshore wedge at ~ 3 cm/yr, such that the wedge has narrowed by $\sim 20\%$ since mid-Pleistocene time (Figure 5.5). As long as aggressive erosion continues unabated, the St. Elias orogen should continue to contract due to the accumulation of shortening, until the inactive deformation front merges with the active deformation front and establishes a new equilibrium form. At the onset of glacial interval C, the zone of active deformation within the wedge narrowed to a much greater extent ($\sim 50\%$) (Figure 5.5), suggesting that effective deformation within orogens may be confined to narrow zones within a larger wedge complex and may fluctuate depending on climatic conditions. This redistribution of deformation is consistent with model results that indicate active wedges should contract in response to an increase in fluvial erosion (Whipple and Meade, 2004; Stolar et al., 2006) or a transition to or intensification of glacial climate (Tomkin, 2007; Tomkin and Roe, 2007).

DISCUSSION AND CONCLUSION

The unique perspective offered by combining these distinct data sets provides an empirical view of how an orogen evolves kinematically in response to a climate shift towards Intense glacial conditions. The observations imply that Quaternary deformation within the St. Elias orogenic wedge has been directly influenced by glacial erosion. The trigger for the reorganization of the orogenic wedge was not the onset of northern hemisphere glacial conditions at ~ 3 -2.5 Ma, but rather the intensification of glacier

coverage in mid-Pleistocene time and, perhaps, a shift in glacier morpho-dynamics towards more erosionally-effective ice-streams. The response of a critical wedge to climatic perturbations may therefore function on the basis of thresholds such that enhanced glacial erosion and glaciogenic deposition may have pushed the orogen to a tipping point, beyond which a structural reorganization and narrowing of the entire wedge were required. An implication of these results is that the onset and acceleration of alpine glaciation in Late Cenozoic time should have modified denudation and deformation within numerous mountain belts worldwide, although likely on a more subtle level than the St. Elias orogen. This hypothesis is consistent with climate as the driver of observed changes in exhumation rates, sedimentation rates, and relief within many orogenic systems over the last few million years (Molnar and England, 1990; Lamb and Davis, 2003). Where present, glaciation may thus play a significant role in the internal processes of mountain building, empirically supporting the paradigm that orogenic architecture, kinematics, and evolution may be directly influenced by atmospheric processes.

ACKNOWLEDGEMENTS

We thank collaborators in studying the St. Elias orogen and other colleagues for many helpful discussions and ideas, including Jamie Buscher, Richard Law, Elizabeth Berger, and particularly all STEEP (St. Elias Erosion-Tectonics Project) participants. Support was provided by National Science Foundation (NSF-EAR 0409224, NSF-EAR 0408584, NSF-EAR 0735402, NSF-ODP 0351620).

REFERENCES

- Andrews, J.T., 1972, Glacier power, mass balances, velocities, and erosion potential: *Z. Geomorphol. N.F. Suppl. Bd.*, 13, 1-17.
- Beaumont, C., Fullsack, P., and Hamilton, J., 1992, Erosional control of active compressional orogens: in McClay, K., ed., *Thrust Tectonics*, Chapman and Hall, London, 1-18.
- Berger, A.L., and Spotila, J.A., in review, Denudation and deformation in a glaciated orogenic wedge: The St. Elias Orogen, Alaska: *Geology*.
- Berger, A.L., Spotila, J.A., Chapman, J.B., Pavlis, T.L., Enkelmann, E., and Buscher, J.T., in press, Architecture, kinematics, and exhumation of a convergent orogenic wedge: A thermochronological investigation of tectonic-climatic interactions within the central St. Elias Orogen, Alaska: *Earth and Planetary Science Letters*.
- Berger, W.H., Jansen, E., 1994, Mid-Pleistocene climate shift - the Nansen connection: In: Johannessen, O.M., Muench, R.D., Overland, J.E. (Eds.), *The Polar Oceans and Their Role in Shaping the Global Environment*, AGU Geophysical Monograph 84, 295-311.
- Brocklehurst S.H. and Whipple, K.X., 2002, Glacial erosion and relief production in the Eastern Sierra Nevada, California: *Geomorphology*, 42, 1-24.
- Bruhn, R.L., Pavlis, T., Plafker, G., and Serpa, L., 2004, Deformation during terrane accretion in the Saint Elias orogen, Alaska: *Geological Society of America Bulletin*, 116, 771-787.

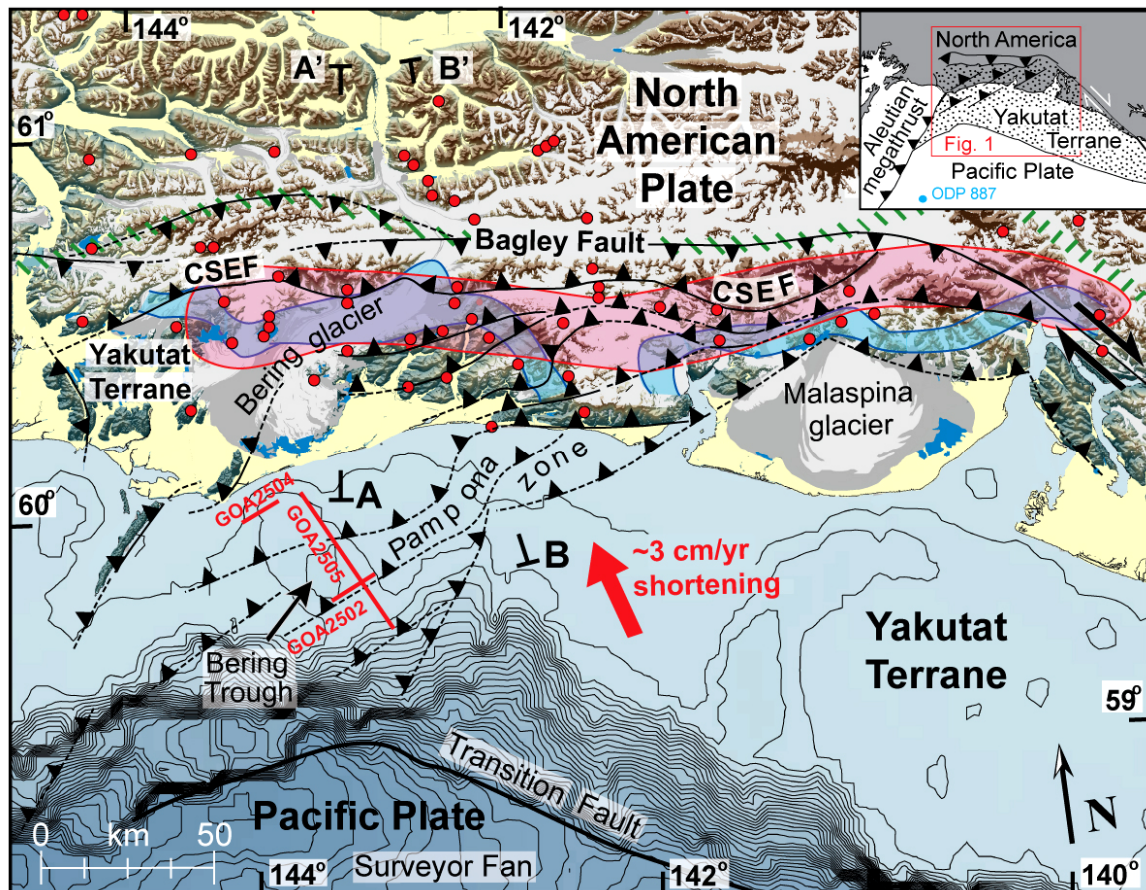
- Clark, P.U., Archer, D., Pollard, D., Blum, J.D., Rial, J.A., Brovkin, V., Mix, A.C., Pisias, N.G., Roy, M., 2006, The middle Pleistocene transition: characteristics, mechanisms, and implications for long-term changes in atmospheric CO₂. *Quaternary Science Reviews* 25, 3150-3184.
- Dahlen, F.A., Suppe, J., and Davis, D., 1984, Mechanics of fold-and-thrust belts and accretionary wedges; cohesive Coulomb theory: *Journal of Geophysical Research*, 89, 10,087-10,101.
- Davis, D., Suppe, J., and Dahlen, F.A., 1983, Mechanics of fold-and-thrust belts and accretionary wedges: *Journal of Geophysics Res.*, 88, 1153-1172.
- Gulick, S., Lowe, L., Pavlis, T., Mayer, L. Gardner, J., 2007, Geophysical insights into the Transition fault debate: Propagating strike-slip in response to stalling Yakutat block subduction in the Gulf of Alaska: *Geology*, 35, 763-766.
- Huntington, K.W., Blythe, A.E., and Hodges, K.V., 2006, Climate change and Late Pliocene acceleration of erosion in the Himalaya: *Earth and Planetary Science Letters*, 252, 107-118.
- Johnston S.A., 2005, Geologic structure and exhumation accompanying Yakutat terrane collision, southern Alaska: Oregon State University, M.S. thesis, 49 p.
- Lagoë, M. B., and Zellers, S. D., 1996, Depositional and microfaunal response to Pliocene climate change and tectonics in the eastern Gulf of Alaska: *Marine Micropaleontology*, 27, 121-140.
- Lamb, S., and Davis, P., 2003, Cenozoic climate change as a possible cause for rise of the Andes: *Nature*, 425, 792-797.

- Lisiecki, L. E., and Raymo, M. E., 2005, A Pliocene-Pleistocene stack of 57 globally distributed benthic $\delta^{18}\text{O}$ records, *Paleoceanography*, 20, PA1003.
- Lowe, L., Gulick, S., Pavlis, T., in press, Identifying active structures in the Kayak and Pamplona Zones: Implications for offshore tectonics of the Yakutat microplate, Gulf of Alaska: AGU Monograph.
- Molnar, P., and England, P., 1990, Late Cenozoic uplift of mountain ranges and global climate change: Chicken or egg?: *Nature*, 346, 29-34.
- Montgomery, D.R., 2002, Valley formation by fluvial and glacial erosion: *Geology*, 30, 1047-1050.
- Péwé, T.L., 1975, Quaternary geology of Alaska: U.S. Geological Survey Professional Paper 835, 145 p.
- Plafker, G., Moore, J.C., and Winkler, G.R., 1994, Geology of the southern Alaska margin: in Plafker, G., and Berg, H.C., eds., *The Geology of Alaska*: Boulder, Colorado, Geological Society of America, *Geology of North America*, G-1, 389-449.
- Powell, R.D., and Cooper, J.M., 2002, A glacial sequence stratigraphic model for temperate, glaciated continental shelves, in *Glacier-influenced Sedimentation on High-Latitude Continental Margins*, Geological Society of London Special Publication, 203, 215-244.
- Rea, D. K., and Snoeckx, H., 1995, Sediment fluxes in the Gulf of Alaska; paleoceanographic record from Site 887 on the Patton-Murray Seamount Platform, in Rea, D. K., Basov, I. A., Scholl, D. W., and Allan, J. F., eds.,

- Proceedings of the Ocean Drilling Program, Scientific Results: College Station, TX., Ocean Drilling Program, 247-256.
- Spotila, J.A., Buscher, J.T., Meigs, A.J., and Reiners, P.W., 2004, Long-term glacial erosion of active mountain belts: Example of the Chugach-St. Elias Range, Alaska: *Geology*, 32, 501–504.
- Stolar, D.B., Willett, S.D., and Roe, G.H., 2006, Climatic and tectonic forcing of a critical orogen, in Willett, S.D., Hovius, N., Brandon, M.T., and Fisher, D.M., eds., *Tectonics, Climate, and Landscape Evolution: Geological Society of America Special Paper 398*, Boulder, CO, 241-250.
- Tomkin, J.H., and Roe, G.H., 2007, Climate and tectonic controls on glaciated critical-taper orogens: *Earth and Planetary Sciences*, 262, 385-397.
- Tomkin, J.H., 2007, Coupling glacial erosion and tectonics at active orogens: A numerical modeling study: *Journal of Geophysical Research-Earth Surface*, 112, F02015.
- Whipple, K.X., and Meade, B.J., 2004, Controls on the strength of coupling among climate, erosion, and deformation in two-sided, frictional orogenic wedges at steady state: *Journal of Geophysical Research*, 109, F01011.
- Willett, S.D., 1999, Orogeny and orography; the effects of erosion on the structure of mountain belts: *J. Geophys. Res.*, 104, 28,957-28,982.
- Zachos, J., Pagani, M., Sloan, L., Thomas, E., and Billups, K., 2001, Trends, rhythms, and aberrations in global climate 65 Ma to present: *Science*, 292, 686-693.

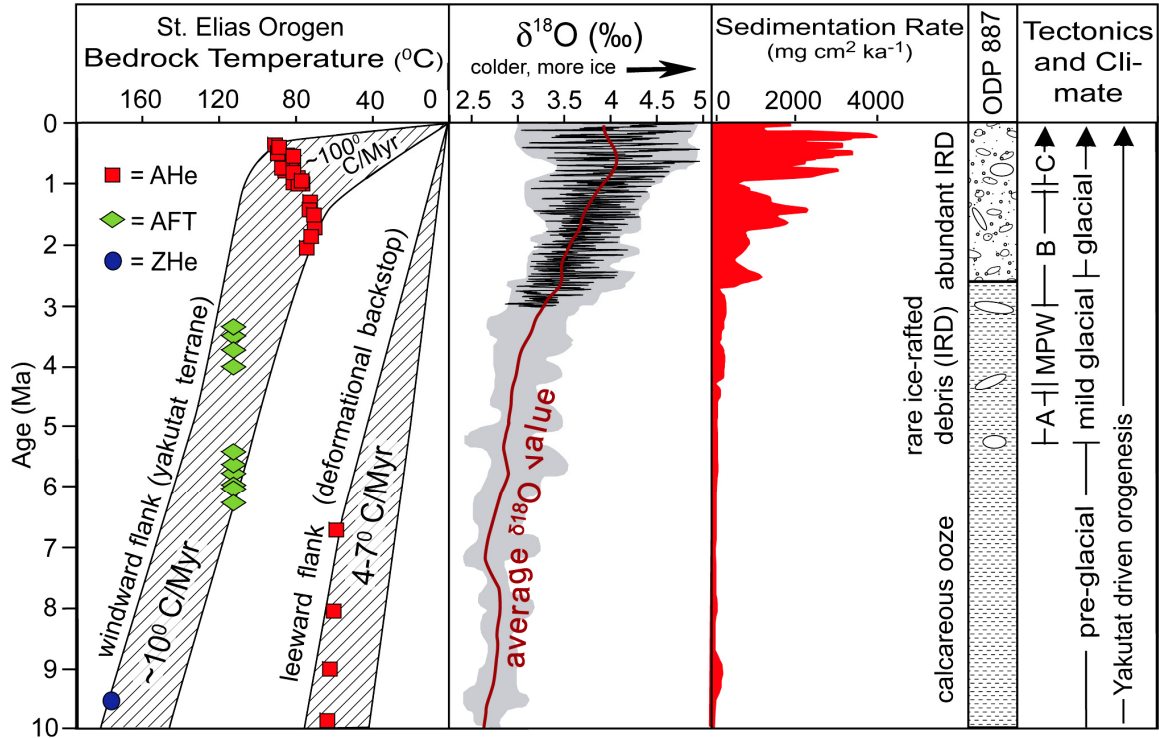
Zellers, S. ,1995, Foraminiferal sequence biostratigraphy and seismic stratigraphy of a tectonically active margin; the Yakataga formation, northeastern Gulf of Alaska, *Marine Micropaleontology*, 26, 255-271.

Figure 5.1: Thermochronometry and tectonics of the St. Elias orogen.



Red dots show locations of 59 AHe ages (Spotila et al., 2004; Berger et al., in press; Berger and Spotila, in review), which delineate the pattern of recent exhumation. Ages are 0.44-1 Ma within the area shown in red on the windward flank, corresponding to exhumation rates of $\sim 2\text{-}5$ mm/yr ($\pm 25\%$). Ages north of the green hatched line are older (6-30 Ma) and correspond to slow ($\sim 0.2\text{-}0.4$ mm/yr ($\pm 25\%$)) exhumation on the leeward flank. The belt of rapid exhumation shown in red correlates roughly with the location where mean Quaternary ELA (i.e. between modern and glacial maxima limits) intersects the mean topography of the windward flank (Berger and Spotila, in review; Péwé, 1975) (shown in blue), implying that long-term erosion is related to glacial ice flux. The shaded relief map includes bathymetry of the Gulf of Alaska (100 m contour interval), major post mid-Miocene structures (Plafker et al., 1994; Bruhn et al., 2004; Berger et al., in press), the modern distribution of glaciers (white), and deglaciated and ice-proximal areas covered by alluvium (yellow). The Chugach St. Elias fault (CSEF) is the suture between the colliding Yakutat Terrane and North America. Locations of seismic profiles from Figure 5.4 are shown in red and ODP 887 from Figure 5.2 is shown in blue on the regional location map.

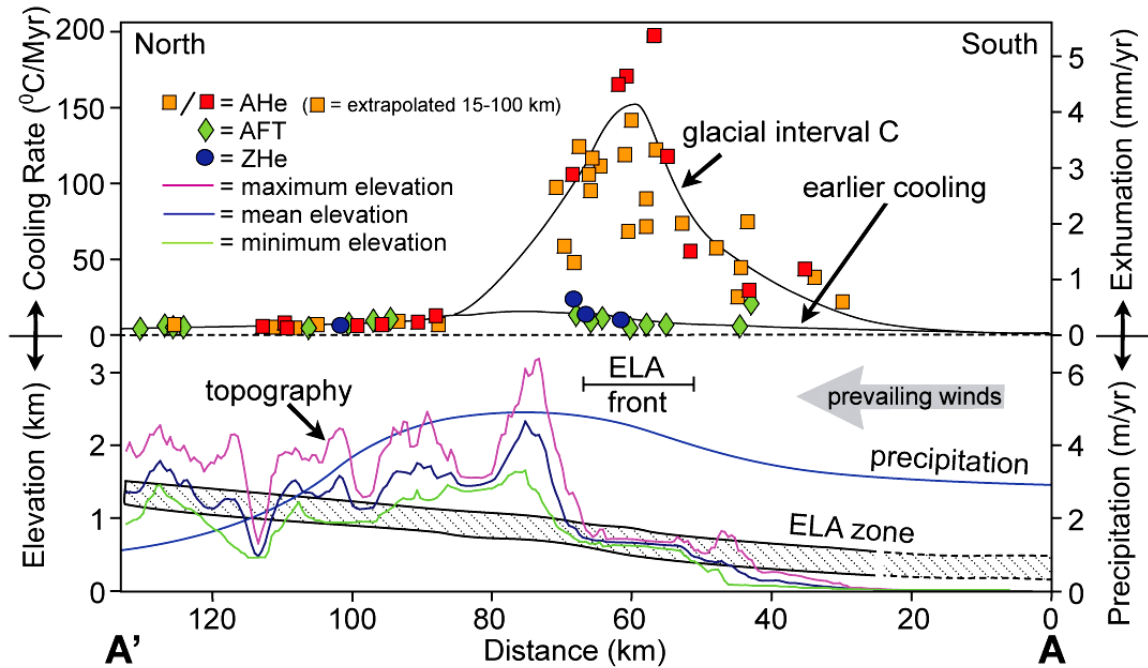
Figure 5.2: History of glaciation, bedrock cooling, and sedimentation during Yakutat driven orogenesis.



Bedrock time-temperature paths for the St. Elias orogen are shown at the left, with ages from the windward (orogenic wedge) and leeward flanks shown separately. Lines encompass possible cooling paths and are constrained by older AFT and ZHe ages that do not fall on the plot. AHe ages from the windward flank require significant acceleration in cooling in the past ~1 Ma. Globally distributed marine records of benthic oxygen isotopes (a proxy of global ice volume and temperature) are shown with specific values in black (Lisiecki and Raymo, 2005), while the global range and average correlate to the shaded area and red line, respectively (Zachos et al., 2001). The increased $\delta^{18}\text{O}$ variability after the Pliocene reflects increased continental ice sheet volume and a corresponding local intensification in glaciation. History of syn-orogenic sediment accumulation in the Gulf of Alaska (mean sedimentation rate (cm/ka) times mean sediment dry bulk density (g/cm³)) for ODP (Ocean Drilling Program) site 887 are shown (Rea and Snoecke, 1995), indicating an increase in sedimentation occurred coincident with the intensification of glaciation and acceleration of bedrock cooling on the windward flank of the orogen. The age control for ODP site 887 is based on paleomagnetism, biostratigraphy, and subsidiary oxygen isotopes data (± 5 ka). Final columns on the right depict the sedimentary facies observed in ODP site 887 and a synthesis of climate events in the orogen. The orogen was dominated by fluvial conditions prior to ~5.5 Ma, when initial mild glaciation began (glacial interval A). This was interrupted by the Mid-

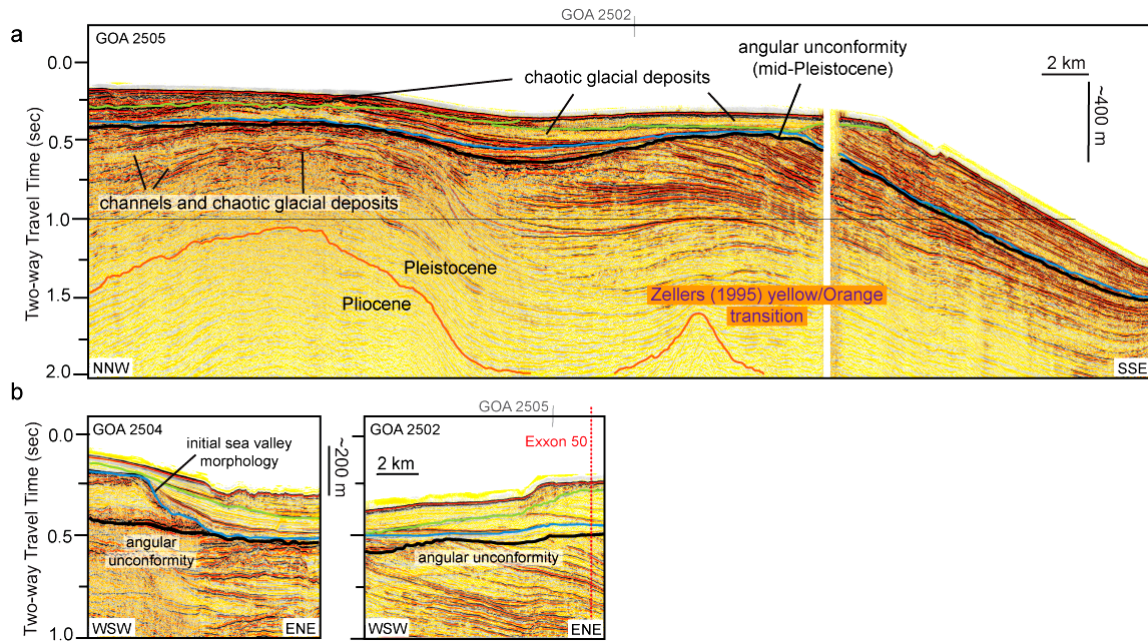
Pliocene Warm Interval (MPW). Renewed glaciation occurred with the onset of glacial interval B starting at ~2.5 Ma and further intensified at ~1 Ma with the onset of glacial interval C.

Figure 5.3: Variation in bedrock cooling rate, topography, and climate across the St. Elias orogen.



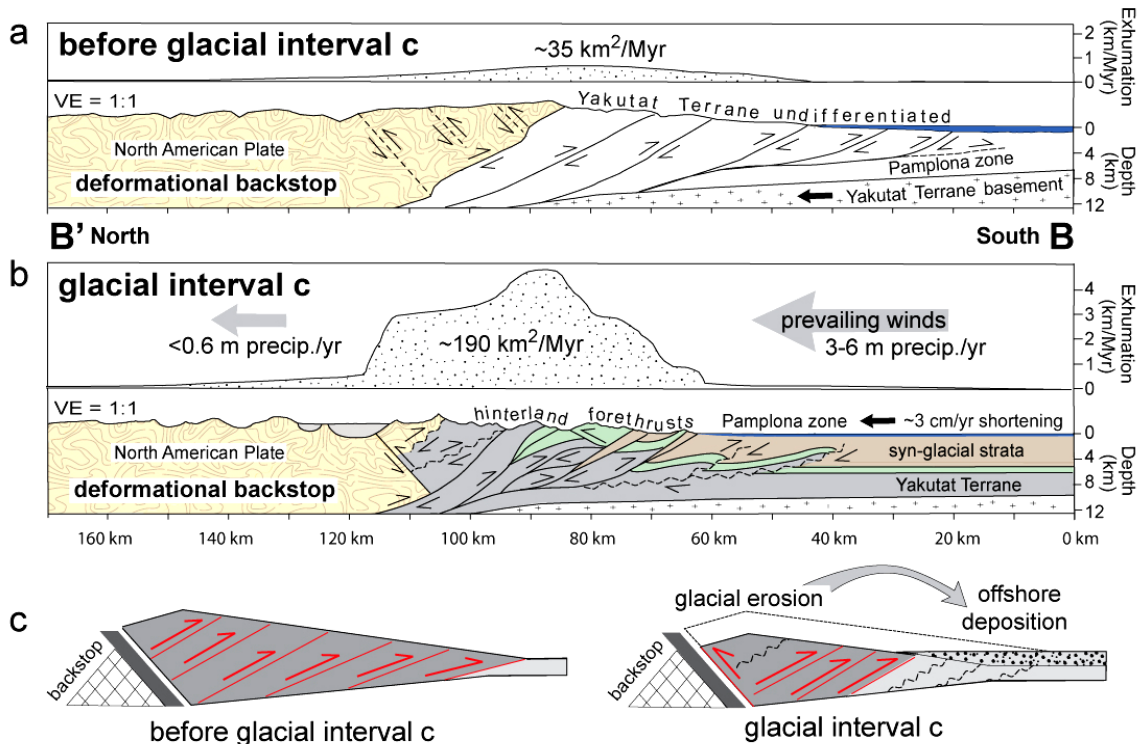
Cooling rates are calculated for all AHe, AFT, and ZHe data in the orogen assuming linear cooling between respective thermochronometers. Rates from AHe ages within 15 km of line AA' (red) and beyond (orange) are rapid only along the windward flank of the orogen near the ELA front, where mean Quaternary ELA intersects the landscape. This indicates rapid cooling in this zone over the past 1 Ma (i.e. during glacial interval C), whereas cooling on the leeward flank throughout Yakutat driven orogenesis and on the windward flank prior to 3.5 Ma (indicated by AFT and ZHE, earlier cooling) was considerably slower. Topography (10-km-wide swath), mean precipitation (Berger and Spotila, in review), and the range of ELA positions (Péwé, 1975) (modern vs. glacial maxima) are shown below. Data follow transect AA', shown in Figure 5.1.

Figure 5.4: Seismic reflection profiles from the continental shelf in the Gulf of Alaska.



Seismic profiles are from the R/V Maurice Ewing cruise 0408, locations shown in Figure 5.1. A) Upper profile follows the length of the Bering Trough (GOA2505). The orange line is interpreted to be the Plio-Pleistocene boundary based on correlation with Exxon Well 50 (crossed by GOA2502) and the biostratigraphic work of Zellers (1995). Dark colored lines on the continental shelf represent glacial erosion surfaces and their correlative conformity. The oldest of these (black) occurred in mid-Pleistocene time and is thought to coincide with the 0.7-1 Ma Middle Pleistocene Transition (Clark et al., 2006). Sediment below this horizon is deformed by the Pamplona Zone structures, whereas younger sediment is undeformed. Evidence of glacial erosion and subsequent deposits are limited to <25 km from the current coast below this horizon and are present out to the shelf-edge above this horizon. B) Crossline profiles are GOA2504, acquired closer to land, and GOA2502, acquired closer to the shelf edge (Figure 5.1). These profiles show the creation of a morphologic sea valley was also subsequent to the mid-Pleistocene angular unconformity. We suggest the cessation of Pamplona zone shortening coincided with, and is causally related to this initial glacial advance to the shelf edge deemed glacial interval C.

Figure 5.5: Proposed model of climate-related influences on orogen kinematics.



A) Architecture of the orogen prior to onset of glacial interval C, drawn along line BB' based on thermochronometry (Berger et al., in press; Berger and Spotila, in review) and geologic data (Plafker et al., 1994; Bruhn et al., 2004) (Figure 5.1). Exhumational flux (shown above) at this time was slow and deformation extended broadly from the backthrust to the most seaward thrust of the Pamplona Zone. Given the limited difference in rock uplift between the deformational backstop and the deforming wedge, activity on the backthrust is believed to have not been significant at this time. B) Architecture of the orogen after intensification of glaciation associated with the onset of glacial interval C. Exhumational flux has increased significantly within the wedge, but not in the deformational backstop, indicating that motion across the backthrust must have accelerated. Denudation and deformation are also concentrated in a narrow zone along the windward flank, suggesting the active, effective part of the wedge narrowed. The Pamplona Zone has been largely shut down due to sediment burial and hinterland exhumation, and should be consumed at $\sim 3 \text{ cm/yr}$ by continued shortening in the hinterland. As the wedge contracts due to backthrust motion, forethrusts appear to be progressively truncated and incorporated into its hanging wall, likely explaining the Plio-Pleistocene shift in deformation away from the Chugach St. Elias fault (Berger et al., in press). C) Interpretative model of the effect of glacial erosion and deposition on the St. Elias critical wedge. Before glacial interval C (left), the critical Coulomb wedge is wider and has greater relief. After the intensification of glaciation, concentrated glacial erosion of the upper portion of the wedge reduced relief, concentrated deformation, required

enhanced back thrusting, and, along with offshore deposition, forced the termination of foreland structures thereby narrowing the wedge. For A, B, and C, straight dashed lines depict structures with only minor amounts of slip and wavy dashed lines depict inactive structures.